

Unstable Metal Hydrides for Possible On-Board Hydrogen Storage

Zhijie Cao ¹, Franziska Habermann ², Konrad Burkmann ², Michael Felderhoff ^{3,*} and Florian Mertens ^{2,*}

¹ Advanced Energy Storage Materials and Devices Laboratory, School of Physics and Electronic-Electrical Engineering, Ningxia University, Yinchuan 750021, China; caozhijie@nxu.edu.cn

² Institut für Physikalische Chemie, Technische Universität Bergakademie Freiberg, Leipziger Straße 29, 09599 Freiberg, Germany; franziska.habermann@doktorand.tu-freiberg.de (F.H.); konrad-joerg.burkmann@doktorand.tu-freiberg.de (K.B.)

³ Max-Planck-Institut für Kohlenforschung, Kaiser-Wilhelm-Platz 1, 45470 Mülheim an der Ruhr, Germany

* Correspondence: felderhoff@mpi-muelheim.mpg.de (M.F.); florian.mertens@chemie.tu-freiberg.de (F.M.); Tel.: +49-(0)208-3062450 (M.F.); +49-(0)3731393737 (F.M.)

Abstract: Hydrogen storage in general is an indispensable prerequisite for the introduction of a hydrogen energy-based infrastructure. In this respect, high-pressure metal hydride (MH) tank systems appear to be one of the most promising hydrogen storage techniques for automotive applications using proton exchange membrane (PEM) fuel cells. These systems bear the potential of achieving a beneficial compromise concerning the comparably large volumetric storage density, wide working temperature range, comparably low liberation of heat, and increased safety. The debatable term “unstable metal hydride” is used in the literature in reference to metal hydrides with high dissociation pressure at a comparably low temperature. Such compounds may help to improve the merits of high-pressure MH tank systems. Consequently, in the last few years, some materials for possible on-board applications in such tank systems have been developed. This review summarizes the state-of-the-art developments of these metal hydrides, mainly including intermetallic compounds and complex hydrides, and offers some guidelines for future developments. Since typical laboratory hydrogen uptake measurements are limited to 200 bar, a possible threshold for defining unstable hydrides could be a value of their equilibrium pressure of $p_{\text{eq}} > 200$ bar for $T < 100$ °C. However, these values would mark a technological future target and most current materials, and those reported in this review, do not fulfill these requirements and need to be seen as current stages of development toward the intended target. For each of the aforementioned categories in this review, special care is taken to not only cover the pioneering and classic research but also to portray the current status and latest advances. For intermetallic compounds, key aspects focus on the influence of partial substitution on the absorption/desorption plateau pressure, hydrogen storage capacity and hysteresis properties. For complex hydrides, the preparation procedures, thermodynamics and theoretical calculation are presented. In addition, challenges, perspectives, and development tendencies in this field are also discussed.

Keywords: hydrogen storage; metal hydrides; intermetallic compounds; complex hydrides



Citation: Cao, Z.; Habermann, F.; Burkmann, K.; Felderhoff, M.; Mertens, F. Unstable Metal Hydrides for Possible On-Board Hydrogen Storage. *Hydrogen* **2024**, *5*, 241–279. <https://doi.org/10.3390/hydrogen5020015>

Academic Editor: Jin-Yoo Suh

Received: 11 April 2024

Revised: 2 May 2024

Accepted: 3 May 2024

Published: 10 May 2024



Copyright: © 2024 by the authors. Licensee MDPI, Basel, Switzerland. This article is an open access article distributed under the terms and conditions of the Creative Commons Attribution (CC BY) license (<https://creativecommons.org/licenses/by/4.0/>).

1. Introduction

Minimizing greenhouse gas emissions to limit global warming has become a global consensus during the past few decades. As an energy carrier, hydrogen is a perfect choice to realistically solve this critical issue due to its high energy density (142 MJ/kg), abundant reserves and zero carbon emissions if renewably produced [1]. In this scenario, the so-called “hydrogen economy”, a long-term guideline toward a cleaner energy system, was proposed, in which hydrogen was introduced into the current energy network to improve the overall cleanliness [2–4]. In this system, hydrogen is mainly combined with proton exchange membrane (PEM) fuel cells, in which protons generated from the anode transfer through the internal electrolyte to react with oxygen at the cathode, and electricity is

produced via electron transfer in the external circuit to drive the vehicles [5]. For on-board PEM fuel cell systems, an efficient and safe hydrogen storage technology guaranteeing a reasonable cruising range (>500 km) should be developed, which poses a challenge because of the inherent properties of hydrogen gas, such as the low volumetric energy density, high volatility and strong inflammability [6–8]. Current approaches for on-board hydrogen storage mainly include compressed gaseous, cryogenic liquid, liquid organic carriers and solid-state materials [9]. However, comprehensive evaluations of the key performances of these techniques lead to the conclusion that no available methods can meet the Department of Energy (DOE) targets [10]. Nowadays, high-pressure gas storage (up to 70 MPa) is the solution for vehicles, mainly because of the achieved relative technological maturity, flexible operation, high energy efficiency, and low maintenance costs. Because of the intrinsic physical limitations, further increasing the gas pressure is insufficient for fulfilling the practical requirements of automotive storage. For on-board applications, this high-pressure gas system is only a compromise of the necessities (cruising distance, dead load, etc.) of fuel cell vehicles with the volumetric and/or gravimetric densities. Although the high-pressure tank systems are widely tested and already used in fuel cell vehicles (e.g., Mirai from Toyota) [11], they still prompt many concerns in regard to the volumetric density, safety, cost, etc. By comparison, solid-state hydrogen storage materials show much higher volumetric efficiency and greater safety, while they suffer from serious thermodynamic and/or kinetic barriers.

A possible solution for the existing dilemma is to combine lightweight high-pressure tank and metal hydrides tank technologies to form a novel hybrid hydrogen storage system, the “high-pressure metal hydride (MH) tank” [12–14]. As shown in Figure 1, the packing densities of metal hydride powders are limited due to the nature of the powder forms; hence, more than 50% of the inner volume of tank system remains empty even when filled with the maximum amount of hydrogen storage material [13]. At this time, filling the free space with high-pressure hydrogen gas will greatly increase the volumetric density and the amount of stored hydrogen. Therefore, this hybrid tank system can realize higher gravimetric and/or volumetric hydrogen density than single solid-state materials or high-pressure gas as long as the volumetric density in the metal hydride stays higher than in the surrounding gas. For instance, under an operating pressure of 35 MPa at 298 K, the amount of stored hydrogen in the hybrid tank (100 L) increases from 2.3 kg to 3.7 kg after filling 100 kg of Ti–Cr–Mn alloy [15].

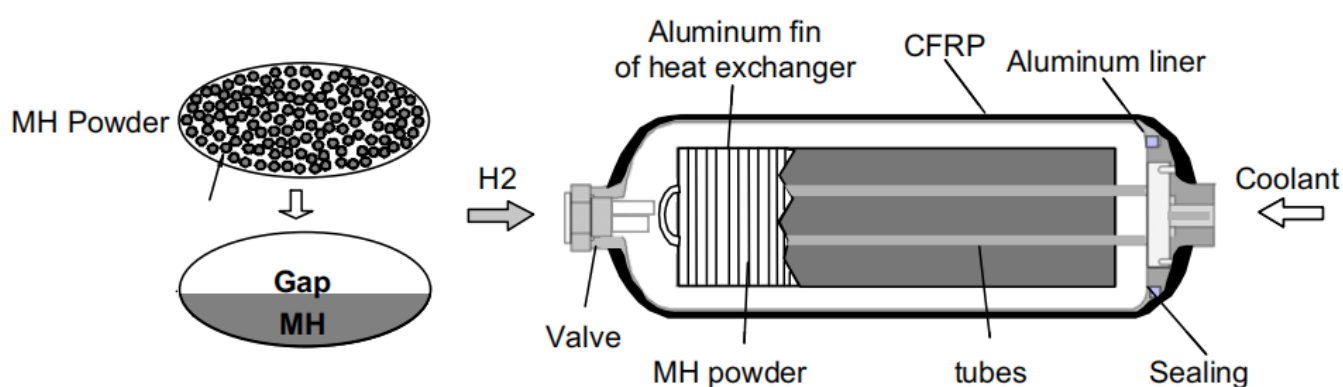


Figure 1. Schematic view of a high-pressure MH tank, reproduced with permission from Elsevier [13].

Suitable metal hydrides are vital to the overall performances of hybrid tanks. During the hydrogen charging process, the hydrogen storage alloys absorb hydrogen to form metal hydrides and release heat, while during the discharging process, the metal hydrides start to desorb hydrogen and absorb heat as the internal pressure decreases to a value lower than the dissociation pressures. To improve the merits of hybrid tanks, it is essential to employ metal hydrides with high dissociation pressures [16]. On the one hand, high dissociation pressure means low desorption temperature, which is beneficial for the hybrid tank system

to supply hydrogen at low temperatures. On the other hand, increasing the dissociation pressure will decrease the heat of the reaction ($\Delta_R H$), which will reduce the thermal effect and improve the heat exchange efficiency of the hydrogen filling/refilling process. In addition, the large hydrogen capacity, excellent kinetics, long-term cycle life and favorable heat management are also essential for the envisioned high-pressure MH tank systems. For a 35 MPa hybrid tank system, Mori et al. [17] proposed some target performances for metal hydrides. As shown in Table 1, the hydrogen storage density and stability are prior target performances for on-board applications.

Table 1. Target performances for metal hydrides [17].

Priority	Specification	Note
1. Hydrogen storage density	Weight > 3–4 wt%	V = stored hydrogen gas volume (273 K, 0.1 MPa)
2. Enthalpy	Volume (V/V_0) > 1800–2400	V_0 = volume of MH
3. Equilibrium pressure	$ \Delta_R H < 20$ kJ/mol H_2	
	>1.0 MPa at 243 K (desorbing)	
	<35 MPa at 393 K (absorbing)	
4. Cyclic durability	Decrease of storage capacity	H_2 purity > 99.99%
	<10% at 1000 cycles	
	<5% at 100 cycles	

To meet the requirements of high-pressure MH tanks, some possible candidates have been developed and tested, mainly including intermetallic compounds and complex metal hydrides. These metal hydrides will decompose under ambient conditions (room temperature, 0.1 MPa pressure). They can only exist at low temperatures and/or under high pressures. The key term “unstable metal hydride” in this review needs some clarification. The term “unstable” in this context does not mean that the hydride is unstable in the thermodynamic or kinetic meaning, being that there is no energetic barrier toward preventing the decomposition. The word “unstable” in the context of this review is understood as the property of the compound to possess a high plateau pressure at moderate temperatures, resulting in the decomposition of the compound even at technologically high pressures. To comprehensively understand and judge the material basis for the developments of suitable metal hydride systems, a review of recent investigations of unstable metal hydrides is essential. Here, we first introduce the developments and applications of intermetallic compounds. Specific examples of partial substitutions and the related mechanisms are provided for AB_2 -type Laves phase alloys and solid solution alloys. The kinetics of these alloys are usually excellent, and the amount of hydrogen absorption or desorption increases quickly and reaches the saturation value within a few minutes or even in seconds, while the equilibrium pressures are either too high or too low for the purpose of high-pressure MH tanks. Therefore, thermodynamic properties are mainly discussed in this part. Then, the concepts, synthesis, and theoretical predictions of complex hydrides, including transition metal alanates and transition metal borohydrides, are mainly emphasized due to their extremely unstable nature. Finally, prospects for addressing the existing challenges and future developments are proposed.

2. Intermetallic Compounds

2.1. AB_2 -Type Laves Phase Alloys

AB_2 -type Laves phase alloys represent one of the most promising material categories for high-pressure MH tank application, primarily because their high dissociation pressures [18–21]. The high variety of interstitial sites endows them with abundant accommodation positions for hydrogen atoms; therefore, they display prominent hydrogen storage properties like a comparably high hydrogen capacity, excellent kinetics and favorable activation properties [22–24]. As shown in Figure 2, AB_2 -type Laves phase alloys possess one the following three structures types: hexagonal C14 ($MgZn_2$ -type), cubic C15 ($MgCu_2$ -type), and hexagonal C36 ($MgNi_2$ -type) [25]. There are three types of tetrahedral sites in these structures: A_2B_2 , AB_3 and B_4 . Regarding hydrogen absorption, these interstitial sites show

distinct preferences in respect of the accommodation of hydrogen atoms [26]. Hydrogen atoms favor the A_2B_2 interstitial positions, followed by the AB_3 sites, whereas the B_4 sites are unable to provide accommodation for hydrogen atoms. Theoretically, the maximum capacity of C14-type and C15-type Laves phases can reach up to 6.3 and 6 hydrogen atoms per formula unit, respectively [27].

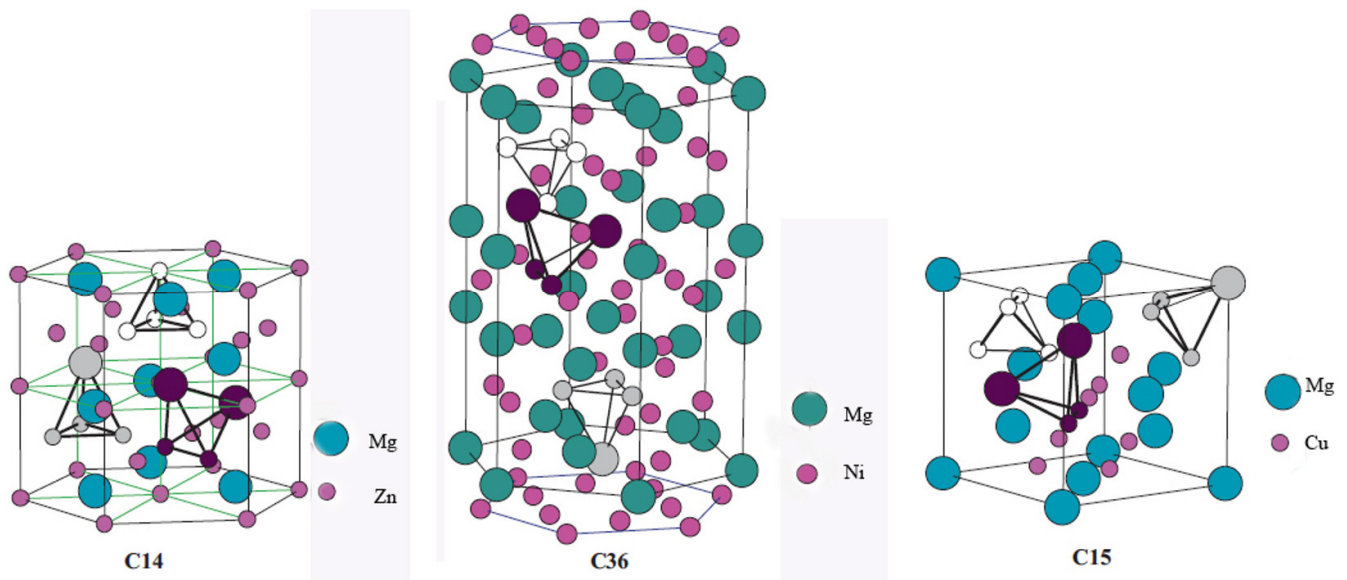


Figure 2. Different types of tetrahedral interstitial sites in C14, C36 and C15 Laves phases. Small and large circles correspond to Cr and Zr atoms, respectively. A_2B_2 interstitial holes are represented by purple atoms; A_1B_3 holes by light gray atoms; and B_4 interstitial holes by white atoms. Reproduced with permission from Elsevier [25].

2.1.1. $TiCr_2$ -Based Alloys

The Ti–Cr system often shows significant deviation from the stoichiometric nominal $TiCr_2$ alloy with the non-stoichiometric composition of $TiCr_x$ ($1.6 \leq x \leq 2.2$). The hexagonal C14 phase is a high-temperature structure, the cubic C15 phase is a low-temperature one, and the structural C36 polytype is an intermediate one with existing temperatures between those of the C15 and C14 structures. Pioneering work was carried out by Johnson and Reilly in 1978 when they found that the C15 phase $TiCr_{1.8}$ can reversibly absorb hydrogen to form two nonstoichiometric phases, $TiCr_{1.8}H_{2.6}$ and $TiCr_{1.8}H_{3.6}$, at 195 K [28]. Both hydrides are extremely unstable, possessing high dissociation pressures of 0.2 MPa and 5 MPa at 195 K, respectively. Subsequently, they investigated the reaction of C14 phase $TiCr_{1.9}$ with hydrogen under the same conditions [29]. This phase can directly uptake hydrogen to produce two unstable nonstoichiometric hydrides of $TiCr_{1.9}H_{2.5}$ and $TiCr_{1.9}H_{3.5}$ at 195 K, having dissociation pressures of ~ 0.02 MPa and 3 MPa, respectively. Hydrogen absorption of C14 phase $TiCr_{1.8}$ at the extremely high pressure of 200 MPa results in the formation of the hydrogen-rich phase $TiCr_{1.8}H_{4.5}$ (3.1 wt%) [30]. In comparison with C14 and C15, hydrides of the C36 phase are much more stable, but the hydrogen capacities ($TiCr_2H_x$, $x \leq 0.5$) are too low to be considered for hydrogen storage purposes [31–33].

For possible applications in high-pressure MH tanks, the plateau pressures of the C14 and C15 phases should be lowered; meanwhile, the hydrogen capacity under moderate pressures needs to be improved to meet the requirements. Partial element substitution at the A sites and/or the B sites has been proven to be an effective method to optimize hydrogen storage performances, like the plateau pressure, capacity, activation and the absorption/desorption hysteresis [34]. From first-principles calculations of C14-type Laves phase Ti–Mn hydrides, Nagasako et al. [35] concluded that the heat of formation (ΔH) of transition metal hydrides can be predicted qualitatively by a single parameter, the B to

V ratio, with B being the bulk modulus and V the equilibrium volume of the host alloy. This computationally motivated yet empirical rule can be used to obtain an estimate of the dissociation pressure (P) given by $\ln P \propto B/V$ to describe the metal hydride decomposition by hydrogen desorption [15]. The relationship found indicates that elements with small bulk modulus and/or large atomic radius can effectively lower the dissociation pressures of hydrogen storage alloys. The increase in the lattice volume will presumably lead to the expansion of the interstitial sites, thus resulting in easier hydrogen uptake and higher hydrogen capacity, which may be an element of the underlying mechanism captured by the empirical rule [36]. In the wake of the publication of the empirical rule, many computational studies were conducted on TiCr₂-based alloys, including the C15 structure [37], C14 Laves phase compounds TiX₂ (X = Cr, Mn, Fe) [38] and TiCrMn [39], which provided useful guidelines to improve the efficiency when designing new TiCr₂-based alloys.

According to the computational and empirical rule, alloying elements, such as Zr, Sc at the A site and Mn, V, Fe, etc., at the B site, were chosen to optimize the performance of TiCr₂-based alloys. Wu et al. [40–42] studied the influence of Zr and Sc on the hydrogen storage properties of TiMnCr. With the increase in the Zr content in Ti_{1-x}Zr_xMnCr ($x = 0 \sim 1.0$), the average value of the hydrogen capacity increases linearly, the plateau pressure decreases monotonously, and the hysteresis between the absorption and desorption curves decreases as the x value increases from 0.2 to 0.32, but increases again as the x value is further raised [40]. When x lies at values between 0.2 and 0.32 in the alloys, the corresponding hydride displays a dissociation pressure higher than 0.1 MPa at 293 K (Figure 3). The introduction of Zr into Ti_{1-x}Zr_x(Mn_{0.5}Cr_{0.5})₂ ($x = 0, 0.1, 0.2, 0.32, 0.5$) alloys induces a decrease in the equilibrium pressure and an increase in the hydrogen capacity [41]. These two effects result in a maximum reversible capacity at $x = 0.32$; meanwhile, the dissociation pressure exceeds 0.1 MPa at 293 K if x is less than 0.32 in the alloys. Similar to the effect of Zr, the increase in the Sc content in Ti_{1-x}Sc_xMnCr ($x = 0.05, 0.10, 0.15, 0.22, 0.27$ and 0.32) alloys also increases the hydrogen storage capacity and decreases the pressure of the absorption/desorption plateau [42]. The difference is that the Sc-doped alloys suffer from much steeper plateaus than the Zr-containing alloys. The partial substitution of the Cr by Mn alters the properties of both the parent alloys and their corresponding hydrides [43–45] in the following ways. The lattice contraction induced by Mn addition in TiCrMn makes the accommodation of a single H atom more difficult, and consequently, this alloy exhibits a high desorption plateau pressure exceeding 10 MPa at 313 K [46]. The PCT curves of TiCr_{2-x}Mn_x-H₂ ($0 \leq x \leq 1$) over a wide range of temperatures from 212 K to 433 K and pressures up to 100 MPa H₂ indicate that both the low-composition hydride phases, i.e., x being small, TiB₂H_{~3} (where B = Cr + Mn) and the high-composition hydride phase (TiB₂H_{~4}), i.e., x being large, are unstable with equilibrium pressures over 1 MPa under ambient conditions [47]. The substitution of V for Cr leads to great changes in the structural and thermodynamic properties of TiCr_{2-x}V_x ($0 \leq x \leq 1.2$) compounds [48]. The TiCr_{2-x}V_x alloy crystallizes in a C14-type Laves phase structure for $0 \leq x \leq 0.3$. For compositions $0.3 \leq x \leq 0.6$, it coexists with a cubic compound, and for $0.6 \leq x \leq 1.2$, the alloy forms a single BCC structure. In respect of thermodynamic stability, the plateau pressure displays a linear decrease with the increase in the V content, and only the TiCr_{2-x}V_x-H₂ ($x < 0.6$) system possesses a plateau pressure higher than 0.1 MPa at 298 K. Substitution of the expensive elements V and/or Ti by ferrovanadium (FeV) and/or Ti sponge (TiS) in Ti_{0.98}Zr_{0.02}V_{0.43}Fe_{0.09}Cr_{0.05}Mn_{1.5} leads to a decrease in the absorption capacity from 2.0 wt% to 1.7 wt%, while the desorption plateau pressure stays at the high level of 1.5 MPa at 298 K [49].

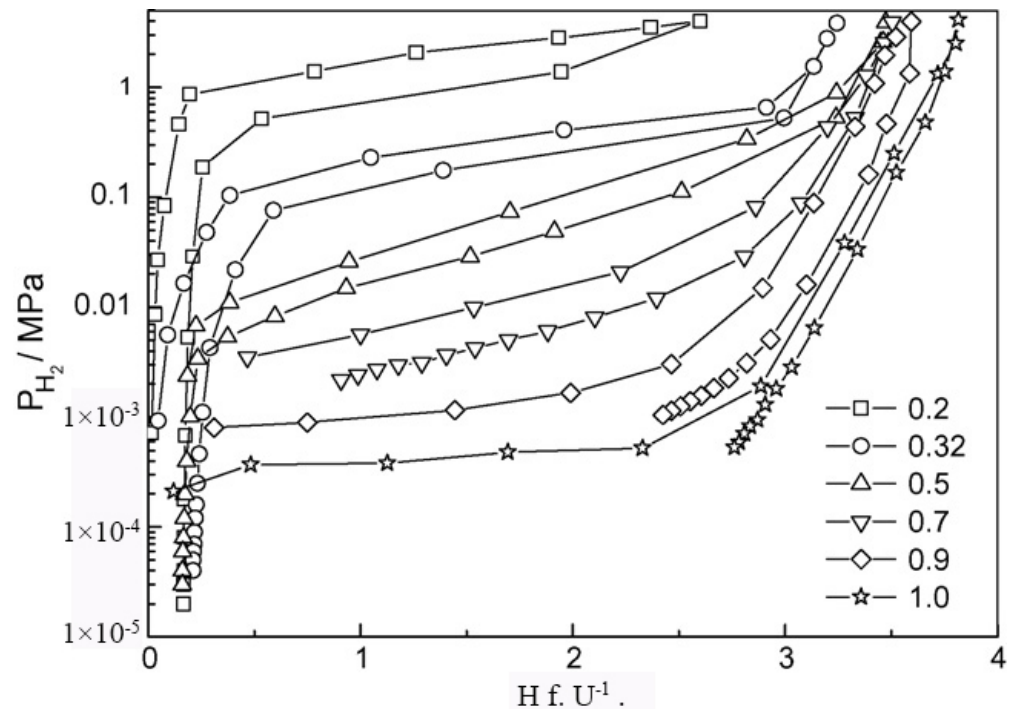


Figure 3. PCT curves of hydrogen absorption–desorption at 293 K of $Ti_{1-x}Zr_xMnCr$ alloys. Reproduced with permission from Elsevier [40].

Compared with the stoichiometric AB_2 alloys, those that are mainly rich in A-atom (hypo or sub) have the same structure but display better hydrogen storage properties due to the high degree of disorder in the structures introduced by the presence of excess elements [50,51]. Hypo-stoichiometric AB_2 alloys with increased Ti or Zr contents were investigated mainly because of their increased hydrogen uptake capacities [52–54], decreased plateau pressures [55,56], improved cycling performances [52], and improved low- and/or high-temperature properties [36]. For potentially unstable metal hydrides, Lee et al. [56] explored Ti–Zr–Cr–Mn Laves phase alloys by partial substitution of Zr for Ti and Cr, V, Cu for Mn to develop suitable materials with a plateau pressure less than 1 MPa at ambient temperature. Among them, $(Ti_{0.75}Zr_{0.25})_{1.05}Mn_{0.8}Cr_{1.05}V_{0.05}Cu_{0.1}$ was the best-performing composition, with a hydrogen capacity of 1.9 wt% and a desorption plateau pressure of 0.3 MPa at 303 K. In 2006, Kojima et al. [15] proposed the development of a $Ti_{1.1}CrMn$ alloy for the 33 MPa high-pressure MH tank for the first time. This non-stoichiometric alloy, having a dissociation pressure of 11 MPa at 296 K (Figure 4), can reversibly store 1.8 wt% H_2 within 5 min in the pressure range of 33 and 0.1 MPa; meanwhile, 94% of the initial capacity can be retained even after 1000 cycles. Combining the hydrogen storage concepts of metal hydrides and high-pressure tanks, by depositing 100 kg of $Ti_{1.1}CrMn$ alloy in a 35 MPa tank of 100 L, the created high-pressure hybrid tank provides 60% more volumetric hydrogen density than the corresponding compressed hydrogen gas under the same conditions. For a hybrid system filled with 100 g of $Ti_{1.1}CrMn$ metal hydride, simulated results demonstrated that the filling process can be finished within less than 12 min at a pressure of 33 MPa [57]. Afterwards, a large variety of alloying elements were investigated to identify suitable non-stoichiometric compositions to fulfill the targets of high-pressure metal hydride MH tank applications. Substituting with Zr at the Ti sites in $Ti_{1.1}CrMn$ contributes to the improvement of the hydrogen storage properties because of the larger radius and higher hydrogen affinity of Zr than of Ti [36]. The optimized $(Ti_{0.9}Zr_{0.1})_{1.1}CrMn$ alloy enjoys an improved hydrogen capacity of 2.2 wt%, and the reversible absorption and desorption process can be accomplished within 4.2 min at even 16 MPa and a low temperature of 268 K. Based on the thermodynamic calculations, this optimized Zr-substituted alloy desorbs hydrogen at 0.32 MPa at 303 K and 13.5 MPa at

353 K, which shows a significant reduction in the sorption pressure plateau compared to the $\text{Ti}_{1.1}\text{CrMn}$ alloy. Ouyang et al. [58] further optimized the hydrogen storage properties of $\text{Ti}_{1.1}\text{CrMn}$ through the partial substitution of Ti by Zr and of Cr by Mo and W. The optimized alloy $(\text{Ti}_{0.85}\text{Zr}_{0.15})_{1.1}\text{Cr}_{0.9}\text{Mo}_{0.1}\text{Mn}$ has a dissociation pressure of ~ 1 MPa and a capacity of 1.78 wt% at 273 K, and it completes the dehydrogenation within 6 min at an initial pressure of 1 atm. According to their calculations, if a hybrid tank is filled with 28% of this alloy, the volumetric hydrogen density of the tank system will reach 40 kg/m^3 ; meanwhile, the gravimetric density remains at the relatively high value of 2.72 wt%. Afterwards, they tried to employ Fe at the B site to lower the cost, and the corresponding $(\text{Ti}_{0.85}\text{Zr}_{0.15})_{1.1}\text{Cr}_{0.925}\text{MnFe}_{0.075}$ alloy displays a similar desorption plateau pressure of 1.06 MPa but a reduced hydrogen capacity of 1.54 wt% at 273 K [59]. Moreover, this alloy can finish the dehydrogenation process within 2 min at 298 K at an initial pressure of 0.1 MPa, and there is almost no capacity loss after 50 absorption/desorption cycles. Chen et al. [60] adjusted the ratio of Cr, Mn, and Fe elements in Ti–Cr–Mn–Fe-based alloys to find an appropriate alloy for hybrid hydrogen storage tank. The results indicate the increase in the plateau pressures with the decrease in the Fe and Mn content, respectively, as was shown for the two series of alloys $\text{TiCr}_{1.9-x}\text{Mn}_{0.1}\text{Fe}_x$ ($0.4 \leq x \leq 0.6$) and $\text{TiCr}_{1.4-y}\text{Mn}_y\text{Fe}_{0.6}$ ($0.1 \leq y \leq 0.3$) alloys. Among these, the Ti super-stoichiometric $\text{Ti}_{1.02}\text{Cr}_{1.1}\text{Mn}_{0.3}\text{Fe}_{0.6}$ alloy showed the best overall hydrogen storage properties, delivering a hydrogen capacity of 1.78 wt% and a hydrogen desorption pressure plateau of 41.28 MPa at 318 K. The authors also found that the Ti super-stoichiometry can lead to the expansion of the unit cell, thus contributing to the improvement of the hydrogen capacity as well as the decrease in the plateau pressure in the $\text{Ti}_{1+x}\text{Cr}_{1.2}\text{Mn}_{0.2}\text{Fe}_{0.6}$ ($x = 0 \leq x \leq 0.1$) alloys [61]. Moreover, the kinetic behaviors of $\text{Ti}_{1.02}\text{Cr}_{1.2}\text{Mn}_{0.2}\text{Fe}_{0.6}$ indicated that this alloy can accomplish hydrogen absorption at 263 K under 21.8 MPa H_2 pressure. Annealing helps to increase the hydrogen absorption and desorption plateau pressure, and to flatten the hydrogen desorption plateau of the $\text{Ti}_{1.02}\text{Cr}_{1.1}\text{Mn}_{0.3}\text{Fe}_{0.6}$ alloy [62]. The annealed alloy displays a dissociation pressure of 45.12 MPa at 318 K and a hydrogen capacity of 1.72 wt%. Chen et al. also adopted rare earth elements (RE = La, Ce, Ho) to modify the original $\text{Ti}_{1.02}\text{Cr}_{1.1}\text{Mn}_{0.3}\text{Fe}_{0.6}$ alloy for improved hydrogen storage behavior. The applied rare earth metal substitutions helped to increase the hydrogen capacity, to lower the absorption/desorption plateau pressure, and to ameliorate the activation properties [63]. Among the studied alloys, the $\text{Ti}_{1.02}\text{Cr}_{1.1}\text{Mn}_{0.3}\text{Fe}_{0.6}\text{La}_{0.03}$ alloy displays the best overall properties, with a hydrogen absorption plateau pressure of 39.31 MPa and 51.27 MPa at 298 K and 318 K, respectively, and a hydrogen capacity up to 1.715 wt% within 20 min. Li et al. [64–66] balanced the elemental contents of Ti, Cr, Fe and Mn to search for proper Ti–Cr–Fe–Mn-based alloys for high-pressure hydrogen storage. Based on their discoveries, the $\text{Ti}_{1.05}\text{Cr}_{0.75}\text{Fe}_{0.25}\text{Mn}_{1.0}$ alloy with a reversible hydrogen capacity of 1.55 wt% within 5 min at 271 K and a desorption plateau pressure of 45 MPa at 333 K was applicable. The authors estimated that a high-pressure hybrid tank based on this material would provide a volumetric density higher than 40 kg/m^3 while being able to supply hydrogen even at temperatures as low as 243 K [66]. Puzskiel et al. [67] designed a non-stoichiometric AB_2 C14 Laves alloy $(\text{Ti}_{0.9}\text{Zr}_{0.1})_{1.25}\text{Cr}_{0.85}\text{Mn}_{1.1}\text{Mo}_{0.05}$ for application in a hybrid reservoir. This alloy has proper thermodynamic stability (nearly 20 kJ/mol H_2), with a desorption equilibrium pressure of 1.4 MPa at 273 K, a hydrogen capacity of 1.5 wt% as well as an absorption/desorption time of 25 s and 70 s, respectively. When the $(\text{Ti}_{0.9}\text{Zr}_{0.1})_{1.25}\text{Cr}_{0.85}\text{Mn}_{1.1}\text{Mo}_{0.05}$ alloy and 10 wt% expanded natural graphite were employed, the hybrid system with a filling degree material of 60% presents a hydrogen volumetric and gravimetric density of $19 \text{ kg H}_2/\text{m}^3$ and 1.8 wt% for the system at a hydrogen pressure of 25 MPa.

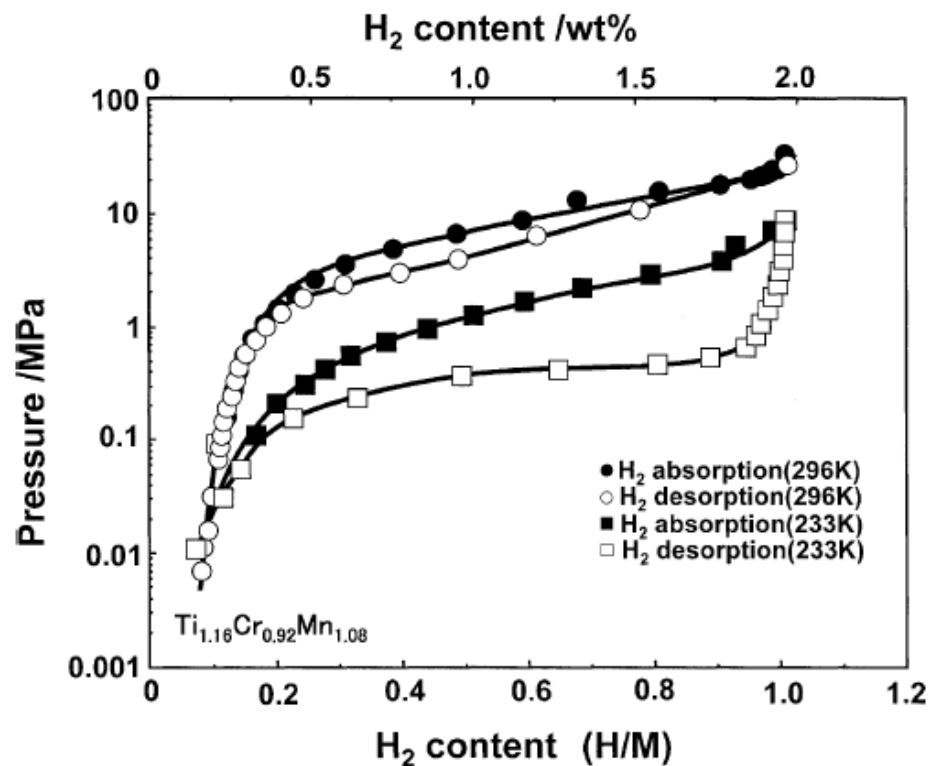


Figure 4. PCT curves for the Ti–Cr–Mn–H system. Reproduced with permission from Elsevier [15].

2.1.2. ZrFe₂-Based Alloys

The Zr–Fe system forms several stoichiometric phases, of which the most important one in respect to hydrogen storage is so far the nominal ZrFe₂ alloy displaying a cubic C15 Laves phase structure [68]. The hydrogen absorption capacity of the ZrFe₂ alloy is less than 0.1 wt% under 6.2 MPa hydrogen at room temperature; hence, it was not considered as a hydrogen absorber until a super high pressure of 1080 MPa was used for the hydrogenation process [69]. The desorption equilibrium pressure of ZrFe₂H₄ even reaches up to 34 MPa at room temperature [70,71]. The hydrogen capacity of ZrFe₂ delivers a relatively high value of 1.7 wt% H₂ at 180 MPa, and an absorption and desorption plateau pressures of 69 MPa and 32.5 MPa, respectively, at room temperature [69].

To improve the hydrogen storage properties of ZrFe₂-derived alloys, various alloying elements, such as Sc, Ti at the A site and V, Cr, Mn, Ni, Al, Mo at the B site, were applied. As shown in Figure 5, substitution of Sc for Zr in ZrFe₂ to generate Zr_{0.8}Sc_{0.2}Fe₂ leads to a significant decrease in the desorption plateau pressure to 4.9 MPa at 253 K [69]. The Zr_{0.8}Sc_{0.2}Fe₂ alloy can also react with hydrogen at 10 MPa even without any activation treatment at such a low temperature. Kouloukakis et al. [72] substituted Fe with Cr or V in ZrFe₂, producing ZrFe_{1.8}M_{0.2} (M = V, Cr) alloys to promote the application of metal hydride hydrogen compressor systems. Compared to Cr-containing alloys, the V-substituted samples show lower plateau pressure and less hysteresis but still a similar maximum hydrogen capacity of 1.4 wt% at 293 K. With the increase in the Fe substitution by V in the alloy series ZrFe_{2-x}V_x ($x = 0.2, 0.4, 0.6, 0.8$), the plateau pressure significantly decreases and the stability of the hydrides increases, accompanied by a gradual transformation of the C15 lattice structure into the C14 structure [73]. The substitution of Mn at the Fe sites resulting in the series of ZrFe_{2-x}Mn_x ($x = 0.2, 0.4, 0.6, 0.8$) increases the unit cell volume, thereby lowering the plateau pressure and increasing the hydrogen storage capacity [74]. All these Mn-substituted alloys form unstable hydrides, with an equilibrium pressure surpassing 0.2 MPa at 303 K. The increase in the Ni content from 0.2 to 0.8 in ZrFe_{2-x}Ni_x ($0.2 \leq x \leq 0.8$) alloys at 295 K effectively reduces the dissociation pressure from 32.5 MPa to 11.5 MPa while essentially keeping the absorbed hydrogen capacity at values of

1.7–1.8 wt% at 295 K at 100 MPa [75]. The formation of $\text{ZrFe}_{1.8}\text{Ni}_{0.2}\text{H}_{3.5}$ and $\text{ZrFe}_{1.2}\text{Ni}_{0.8}\text{H}_{3.7}$ hydrides results in isotropic expansion (24–26.5%) of the metal lattice without changing the structure type and the hydrogen atoms tend to occupy the tetrahedral sites with the $[\text{Zr}(\text{Fe}, \text{Ni})_3]$ coordination [76]. The substitution of Al for Fe in ZrFe_2 alloy contributes to the very fast H/D exchange kinetics in the formed hydrides, accompanied by a dramatic decrease in the deuterium absorption plateau pressures [77]. When x increases from 0.02 to 0.04 in $\text{ZrFe}_{2-x}\text{Al}_x$ alloys, the absorption plateau pressure at room temperature decreases from 56 MPa to 41 MPa [78]. Extensive studies have been devoted to $\text{Zr}(\text{Fe}_{1-x}\text{M}_x)_2$ ($\text{M} = \text{V}$ [79–81], Mn [82,83], Ni [84], Co [85], Al [86], Cr [87,88], etc.), ZrMnFe_x ($x = 1.2\text{--}1.4$) [89], $\text{Zr}_{1-x}\text{Ti}_x\text{MnFe}$ ($x = 0.2, 0.3$) [90] alloys to improve the hydrogen storage properties.

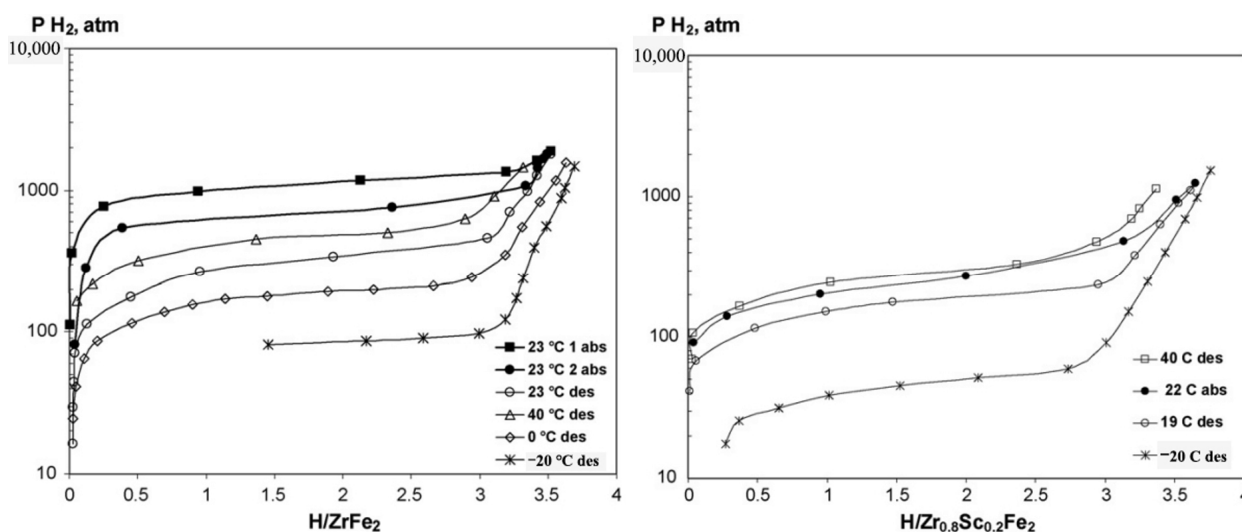


Figure 5. PCT curves for the $\text{ZrFe}_2\text{--H}_2$ and $\text{Zr}_{0.8}\text{Sc}_{0.2}\text{Fe}_2\text{--H}_2$ systems. Reproduced with permission from Elsevier [69].

Compared with individual element substitution, multi-element substitution shows much more advantages in obtaining excellent hydrogen storage performances. Zotov et al. [91] found that Ti and Al substitution effectively lowers the hydrogen absorption plateau pressure to 3.4 MPa for the composition of $\text{Zr}_{0.5}\text{Ti}_{0.5}\text{Fe}_{1.6}\text{Al}_{0.4}$ at room temperature. Subsequently, through multiple elements substitution at both the A and B sites, they flexibly adjusted the absorption/desorption plateau pressures of $\text{Zr}_{1-x}\text{M}_1_x(\text{Fe}_{1-y}\text{M}_2_y)_2$ ($\text{M}_1 = \text{Ti}, \text{Y}, \text{Dy}$; $\text{M}_2 = \text{V}, \text{Cr}, \text{Mn}, \text{Ni}, \text{Co}, \text{Cu}$ and Mo) alloys in the range from 0.5 MPa to 250 MPa [92]. The mischmetal (Mm), Ti- and Cr-substituted $\text{Zr}_{1-2x}\text{Mm}_x\text{Ti}_x\text{Fe}_{1.4}\text{Cr}_{0.6}$ ($x = 0, 0.05, 0.1$ and 0.2) alloys show high hydrogen capacity of ~ 1.75 wt% and kinetics of $\sim 30 \text{ cm}^3 \text{ min}^{-1} \text{ g}^{-1}$, which is three times faster than the $\text{ZrFe}_{1.4}\text{Cr}_{0.6}$ alloy [93]. After annealing at 1270 K for 100 h, these alloys exhibit higher uptake of hydrogen and flatter absorption/desorption plateau than before the treatment [94]. The optimal composition $\text{Zr}_{0.9}\text{Mm}_{0.05}\text{Ti}_{0.05}\text{Fe}_{1.4}\text{Cr}_{0.6}$ possesses a relatively high storage capacity of ~ 1.94 wt% and a desorption plateau pressure of ~ 0.15 MPa at 299 K. The non-stoichiometric compositions are also designed to improve the hydrogen storage properties of ZrFe_2 -based alloys. Sivov et al. [95] showed that the absorption/desorption plateau pressures of activated samples decrease considerably while the hysteresis between the absorption and desorption isotherms increases with the decrease in the Fe content in ZrFe_x ($1.9 \leq x \leq 2.5$) alloys. Among them, $\text{ZrFe}_{1.9}$ displays the best performance, with a hydrogen capacity of 1.8 wt% and a dissociation pressure of 23.7 MPa at 295 K. In regard to substitutions of V for Fe in $\text{ZrFe}_{2.05-x}\text{V}_x$ ($0.05 \leq x \leq 0.2$) alloys, Jiang et al. [96] found that the increase in the lattice parameters and the unit cell volumes of the alloys leads to the increase in the hydrogen capacity, the decrease in the plateau pressure, and to the decrease in the hysteresis factor. The dehydrogenation $\Delta_R H$ of these

alloys varies from 20.41 to 22.03 kJ/mol H₂, and all their dissociation pressures are higher than 11 MPa at 313 K. These alloys absorb hydrogen very quickly and can reach 90% of the maximum capacity within 71 s.

For the possible use in high-pressure metal hydride tanks, Ouyang et al. [97] employed Ti and V to modify the properties of Zr–Fe–V alloys, among which the non-stoichiometric (Zr_{0.7}Ti_{0.3})_{1.04}Fe_{1.8}V_{0.2} alloy shows the best performance, with a desorption plateau pressure and a reversible capacity of 1.12 MPa and 1.51 wt%, respectively. Meanwhile, this alloy can complete dehydrogenation within 8 min at 273 K, and this process is reduced to 5 min at 298 K. Combining this alloy with a 35 MPa high-pressure tank, as shown in Figure 6, the hybrid system can provide a gravimetric density of 1.95 wt% and a volumetric H₂ density of 40 kg/m³, respectively. Afterwards, they developed the series of Zr_{1.05}Fe_{1.85}Cr_{0.15–x}V_x ($x = 0.05, 0.075, 0.1$) alloys by Cr and V substitution [98]. The Zr_{1.05}Fe_{1.85}Cr_{0.075}V_{0.075} alloy delivers a hydrogen capacity of 1.54 wt%, and an absorption and desorption plateau pressure of 1.4 MPa and 0.97 MPa, respectively, at 243 K. Further investigations of the Ti-, Mn- and V-substituted Zr_{1.05}Fe₂ alloys found that the addition of V decreases the hysteresis, while Ti leads to a low plateau slope and a high plateau pressure [99]. Among these alloys, Zr_{1.05}Fe_{1.6}Mn_{0.4} shows a high desorption plateau pressure of 2.06 MPa at 298 K, while Zr_{1.05}Fe_{1.7}Mn_{0.2}V_{0.1} has the lowest hysteresis. In addition, there are more non-stoichiometric ZrFe₂-based alloys displaying high plateau pressures over 0.1 MPa and moderate hydrogen storage capacities at room temperature, such as Zr_{0.9}Ti_{0.1}(Mn_{0.9}V_{0.1})_{1.1}Fe_{0.5}Ni_{0.5} [100], ZrMn_{0.85–x}Fe_{1+x} ($x = 0, 0.2, 0.4$) [101], (Zr_{0.9}Ti_{0.1})_{1.1}Mn_{0.9}V_{0.1}Fe_{0.5}Co_{0.5} [102], etc.

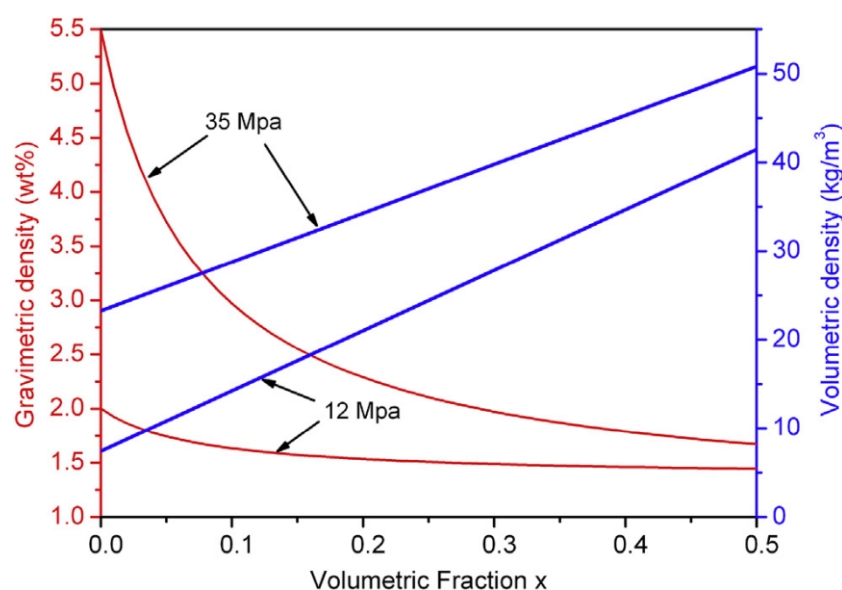


Figure 6. Calculated curves of the volumetric and gravimetric H₂ density vs. the volumetric ratio of the filled alloy in a hybrid tank under 12 MPa and 35 MPa. Reproduced with permission from Elsevier [97].

2.2. Solid Solution Alloys

Vanadium-based solid solution alloys with body-centered cubic (BCC) structures are considered as candidates mainly because of their relatively wide compositional range and high hydrogen capacities up to ~4 wt% H₂ [103]. For instance, the Ti₄₀V₄₀Cr₁₀Mn₁₀ BCC alloy can absorb an extremely high amount of hydrogen, as expressed by the gravimetric density value of 4.2 wt% at 293 K at 3 MPa [104]. The hydrogen storage capacity of Ti_{43.5}V₄₉Fe_{7.5} is 3.9 wt% at 253 K and 5 MPa [104,105]. As shown in Figure 7, these alloys usually show two plateau pressures [106]. The absorption of alloys will proceed when the system pressure is higher than the plateau pressure, while desorption cannot take place until the system pressure drops below the plateau pressure. The plateau pressure of the

first one is around 0.1 Pa, far below the moderate conditions; therefore, only about half of the absorbed hydrogen can be released.

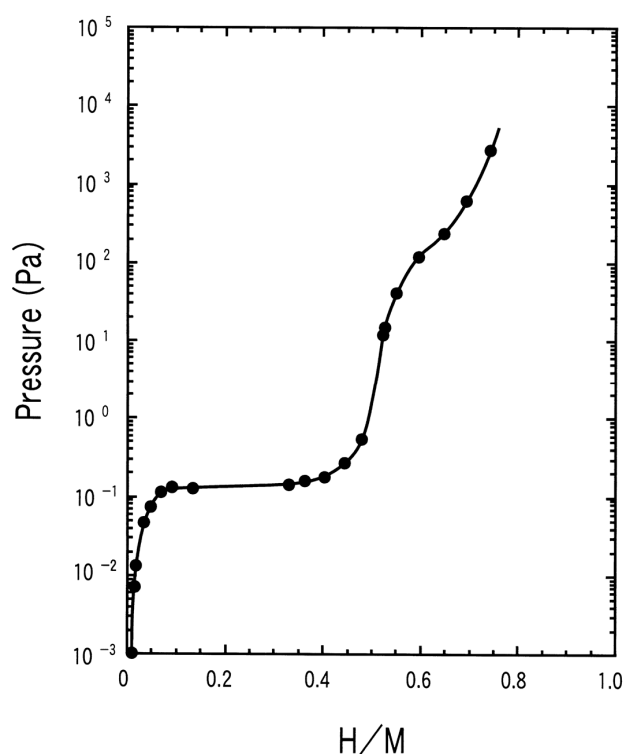


Figure 7. PCT curve for pure vanadium measured at low hydrogen pressures in the course of hydrogenation at 343 K. Reproduced with permission from Elsevier [106].

Alloying with other transition elements, such as Ti, Cr, Mn, Al, Mo, etc., is still the most effective approach to lower the thermodynamic stability and to improve the capacity of the corresponding metal hydrides. By replacing Cr with Mn and/or Fe in Ti–Cr–V alloys, Yoo et al. [107] were able to increase the reversible hydrogen capacity to 2.5 wt% without significantly changing the plateau pressure and the available hydrogen. The $\text{Ti}_{0.32}\text{Cr}_{0.32}\text{V}_{0.25}\text{Fe}_{0.03}\text{Mn}_{0.08}$ alloy reaches a high capacity value of 2.71 wt% within 100 s with a desorption plateau pressure higher than 0.1 MPa at 313 K. The homogeneity of Ti–Cr–V alloys highly influences the hydrogen absorbing properties and the reversible hydrogen capacity of $\text{Ti}_1\text{Cr}_1\text{V}_1$ alloy increases from 2.1 wt% to 2.7 wt% at 323 K and at 4 MPa after heat treatment [108]. RE (RE = La, Pr, Ce and Nd) addition can make H atom entry into the $\text{V}_{55}\text{Ti}_{22.5}\text{Cr}_{16.1}\text{Fe}_{6.4}$ alloy derivatives easier by providing more diffusion pathways, thus greatly increasing their absorption kinetics [109], while the addition of RE elements has little influence on their plateau pressures. These alloys usually have desorption plateau pressures around 0.1 MPa at room temperature, which is slightly higher or lower than that of the pristine alloy. Extensive efforts have been devoted to optimizing the hydrogen storage properties of vanadium-based BCC alloys. Binary alloys such as V–Ti [110–112], V–Cr [113–115], and V–Mo [116–118], ternary alloys such as Ti–V–Cr [119–121] and V–Ti–Fe [122–124], and multiterinary systems including Ti–Cr–V–Mo [125], Ti–V–Fe–Cr [126], and Ti–V–Cr–Fe–Al [127] were developed to yield less stable hydrides.

Although alloying with other transition elements effectively lowers the thermodynamic stability, the plateau pressures of most vanadium-based BCC alloys do not fulfill the requirements for high-pressure MH tanks. Matsunaga et al. [16] tried to employ Mo possessing a large bulk modulus (272.5 GPa) to increase the plateau pressure of TiCrV-based alloys. As shown in Figure 8, the $\text{Ti}_{25}\text{Cr}_{50}\text{V}_{20}\text{Mo}_5$ BCC alloy, as an example of this effort, enjoys an effective capacity of 2.4 wt% H_2 between 0.1 MPa and 33 MPa at 298 K, accompanied by a plateau pressure of 2.3 MPa at 298 K. The results show that elements

with a large bulk modulus, such as Cr (190.1 GPa), Mo (272.5 GPa), and W (323.2 GPa), exert an effect to increase the plateau pressure of metal hydrides, which can help to design new materials with moderate stability.

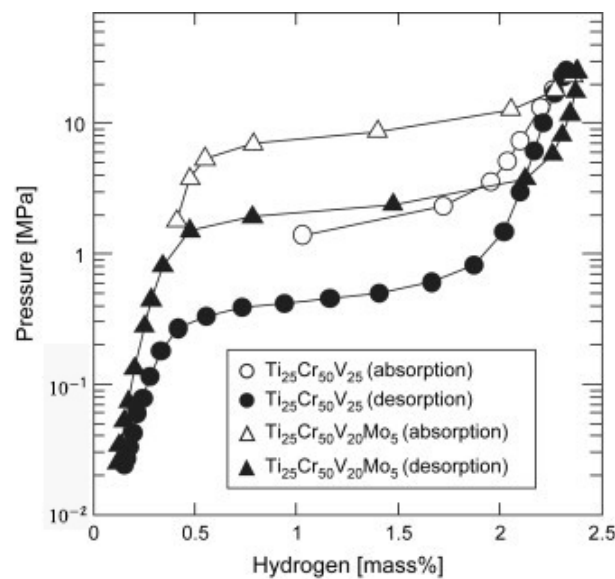


Figure 8. PCT curves of TiCrV and TiCrVMo. Reproduced with permission from Elsevier [16].

As shown in Figure 9, the composition of Ti–Cr–V–Mo alloys greatly influences their hydrogen storage properties [125]. $\text{Ti}_{25}\text{Cr}_{50}\text{V}_{20}\text{Mo}_5$ shows a higher capacity of ~ 2.4 wt% and a higher desorption plateau pressure of ~ 0.7 MPa at 273 K, while it suffers from significant capacity degradation over 10 cycles. $\text{Ti}_{10}\text{Cr}_{10}\text{V}_{75}\text{Mo}_5$ has a slightly lower capacity of ~ 2.0 wt%, a significantly lower desorption plateau pressure of ~ 0.2 MPa at 298 K, but maintains good cycling stability. Further improvements to the hydrogen properties of V–Ti–Cr alloys for high-pressure MH tanks can be achieved through composition optimization. Kuriwa et al. [128] revealed that not only the Ti/Cr ratio but also the V content influences the hydrogen capacity, plateau pressure and cyclic durability.

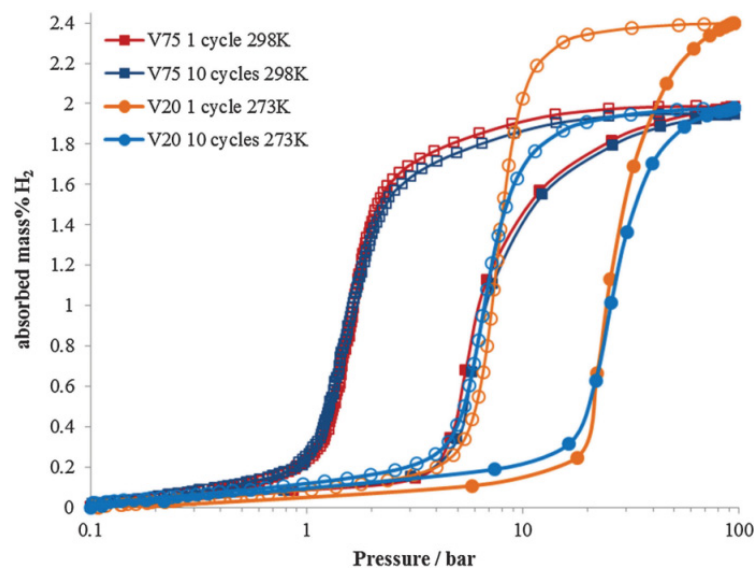


Figure 9. Hydrogen pressure composition isotherm for $\text{Ti}_{25}\text{Cr}_{50}\text{V}_{20}\text{Mo}_5$ (V20) at 273 K and $\text{Ti}_{10}\text{Cr}_{10}\text{V}_{75}\text{Mo}_5$ (V75) at 298 K for 1 cycle and 10 cycle samples during hydrogen absorption (filled data points) and desorption (empty data points). Reproduced with permission from the Royal Society of Chemistry [125].

As shown in Figure 10, the 75at%V-5at%Ti-Cr alloy demonstrates a good flat hydrogen desorption plateau, with a pressure of 0.35 MPa at 273 K and a reversible hydrogen capacity of 2.3 wt% at the 10th cycle, and shows almost no degradation after 200 cycles. PCT curves up to 100 MPa within the temperature range from 273 K to 473 K reveal that the 40V-20Ti-40Cr (at%) alloy has a reversible hydrogen capacity of 1.8 wt% and a desorption plateau pressure of ~0.25 MPa at 293 K [129]. During the first 10 absorption/desorption cycles, the $V_{40}Ti_{21.5}Cr_{38.5}$ alloy experiences an obvious decay in the maximum capacity from 2.44 wt% to 1.88 wt% and the desorption plateau shifts to 0.25 MPa, while the PCT curves after 10 cycles are quite similar to those after 100 cycles [130]. There are more developed vanadium-based BCC alloys having the possibility for use in the hybrid system, as reviewed in references [131–133]. It should be noted that the high cost of V can be an obstacle for large-scale applications [134]. Therefore, some cheaper V resources, such as the conventional ferrovanadium master alloy (FeV80), have been tested for the substitution of pure V. Nomura et al. [105] firstly tried to prepare Ti–V–X (X = Fe, Co, Ni, Cr and Pd) alloys using two kinds of industrial ferrovanadium alloys containing about 4 wt% of impurities (Al, Si, etc.), but remarkable differences in the PCT curves were observed between the pure alloys and the impurity-containing ones. Afterwards, Bibienne et al. [135] found that the ferrovanadium substitution in $Ti_{1.56}V_{0.36}Cr_{1.08}$ and $Ti_{1.26}V_{0.63}Cr_{1.11}$ BCC alloys results in no obvious change in the lattice, the hydrogen capacities, heat of formation, as well as entropy. $V_{30}Ti_{32}Cr_{32}Fe_6$ alloy prepared from a FeV80 master alloy is able to uptake 3.76 wt% H_2 at 298 K, desorb 2.35 wt% H_2 , and has a desorption plateau pressure of 0.13 MPa at 298 K [136]. Wu et al. [137] found that $V_{60}Ti_{(21.4+x)}Cr_{(6.6-x)}Fe_{12}$ ($0 \leq x \leq 3$) alloys can quickly absorb hydrogen up to 3.8 wt% H_2 at 298 K without the activation treatment, and the $V_{60}Ti_{22.4}Cr_{5.6}Fe_{12}$ alloy shows the largest reversible capacity of 2.12 wt% H_2 , with a dissociation pressure of 0.062 MPa at room temperature [138,139]. Afterwards, they prepared two series of $(FeV80)_{48}Ti_{26+x}Cr_{26}$ ($0 \leq x \leq 4$) and $(VFe)_{60}(TiCrCo)_{40-x}Zr_x$ ($0 \leq x \leq 2$) alloys using the FeV80 master alloy, and both alloys have an effective capacity ~2.0 wt% at 298 K and excellent cycling properties. These works show promise when it comes to realizing the large-scale production of low-cost and unstable V-based alloys for on-board applications.

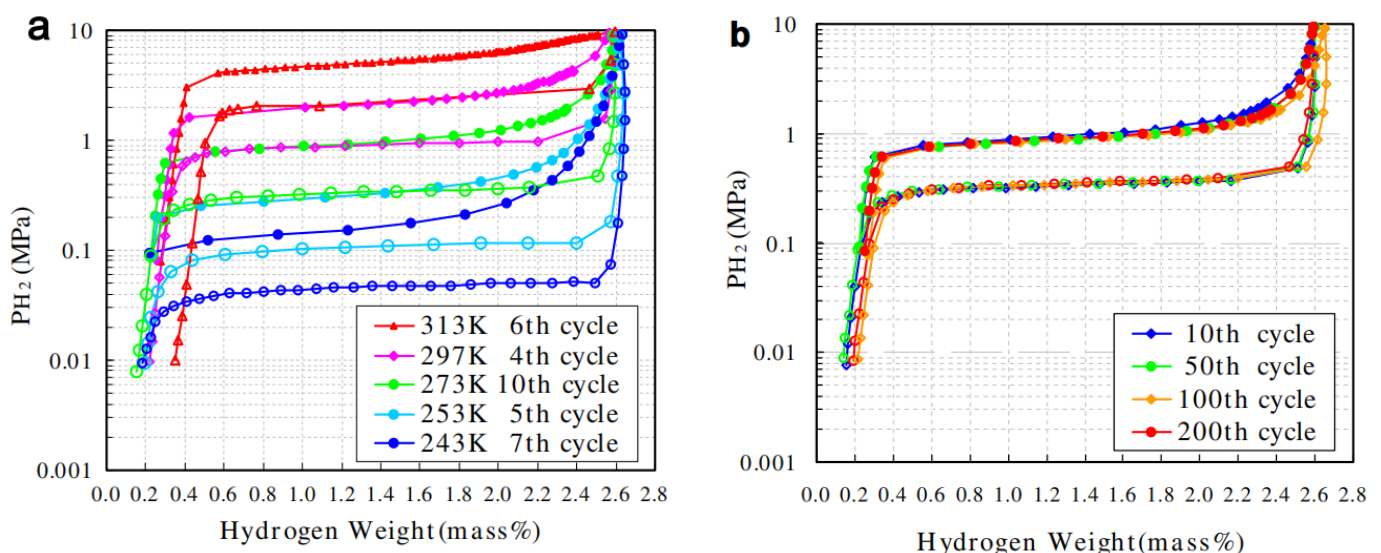


Figure 10. 75at%V-5at%Ti-Cr (a) pressure composition isotherms for 243–313 K, and (b) various cycle measured at 273 K. Reproduced with permission from Elsevier [128].

3. Complex Hydrides

Alanates, borohydrides, and amides are known as complex hydrides and have been widely investigated during the past few decades, mainly because of their high gravimetric densities [140]. For on-board applications, however, they suffer from severe thermodynamic

and/or kinetic barriers in dehydrogenation and/or rehydrogenation. The pioneering work by Bogdanović et al. [141] indicated that catalyst doping, especially for titanium-based species, enables the reversible hydrogen storage of NaAlH_4 under moderate conditions by alleviating the kinetic issues. Subsequently, substantial numbers of studies focused on the development of proper catalysts or approaches to ameliorate the thermodynamics or kinetics of the complex hydrides [142].

3.1. Transition Metal Alanates

Alkali metal and alkaline-earth metal alanates such as LiAlH_4 (10.5 wt%), NaAlH_4 (7.4 wt%), $\text{Mg}(\text{AlH}_4)_2$ (9.3 wt%), etc., offer high hydrogen capacities, but they usually suffer from high dehydrogenation temperatures and sluggish dehydrogenation kinetics. Transition metal alanates, in contrast, are usually thermodynamically less stable in respect to dehydrogenation, which leads to great difficulty in their synthesis. Some have even been solely theoretically discussed [142].

3.1.1. Overview of Known Transition Metal Alanates

Since the early 1950s, a number of transition metal alanates have been synthesized. In order to provide an overview of these alanates and their respective stability, Figure 11 was created.

$T_d \text{ M}(\text{AlH}_4)_n \geq \text{RT}$

 $T_d \text{ M}(\text{AlH}_4)_n < \text{RT}$

 $T_d \text{ M}(\text{AlH}_4)_n$ uncertain

○

 $T_d \text{ MAIH}_x \geq \text{RT}$

○

Figure 11. Overview of the known transition metal alanates and their respective stabilities.

The elements of the periodic table, marked in red, represent alanates that are reported to decompose below room temperature. Alanates of the elements, marked in green, begin to decompose at room temperature or higher temperatures. Blue-marked elements depict alanates whose existence is indicated in the literature but is still uncertain and/or questionable. If the marking is hatched, the literature reports regarding the decomposition temperature are unclear or inconsistent.

Inconsistent literature reports are on hand for $\text{Fe}(\text{AlH}_4)_2$. Monnier observed decomposition at $-125\text{ }^\circ\text{C}$ [143], Kost and Golovanova at $-70\text{ }^\circ\text{C}$ [144], and Neumaier et al. [145] reported it to be stable at room temperature. Unfortunately, Monnier did not specify the observations made during the decomposition process. If only hydrogen was being released, it could be explained by the reduction of Fe(III) to Fe(II) as FeCl_3 was used as a reactant [146]. However, this does not explain the discrepancy between the statements of Kost and Golovanova [144] and Neumaier et al. [145].

According to Monnier, $\text{Co}(\text{AlH}_4)_2$ and $\text{Ni}(\text{AlH}_4)_2$ already decompose at $-125\text{ }^\circ\text{C}$, the freezing point of the solvent diethyl ether [143]. The synthesis was presumably performed by freezing the reaction solutions layer wise and beginning the reaction by allowing the layers to melt. Therefore, it seems likely that the actual decomposition temperatures are much lower than the reported values. Consequently, a question arises whether $\text{Co}(\text{AlH}_4)_2$ and $\text{Ni}(\text{AlH}_4)_2$ can actually be synthesized.

While the existence of $\text{Sc}(\text{AlH}_4)_3$ and $\text{Mo}(\text{AlH}_4)_5$ is not in doubt, their decomposition temperatures are uncertain based on the literature. $\text{Sc}(\text{AlH}_4)_3$ was synthesized by Kuznetsov [147] in only form of the solvent adduct $\text{Sc}(\text{AlH}_4)_3 \cdot \text{Et}_2\text{O}$. The decomposition temperature of this adduct ($80\text{ }^\circ\text{C}$) suggests a decomposition temperature higher than room temperature for the alanate itself. Since the loss of solvent occurs simultaneously with the beginning of the dehydrogenation [147], the decomposition temperature of the alanate should be expected around $80\text{ }^\circ\text{C}$. Regarding $\text{Mo}(\text{AlH}_4)_5$, Monnier only stated a slow decomposition at room temperature [143]. No further specification of the decomposition temperature was provided. In Ref. [143], the decomposition of $\text{Mn}(\text{AlH}_4)_2$ is described in the same manner, but Monnier specified the decomposition temperature of $\text{Mn}(\text{AlH}_4)_2$ in another reference to be $-25\text{ }^\circ\text{C}$ [148], which is much lower than in Ref. [142]. This result combined with the overall instability of transition metal alanates indicates that the same might be true for $\text{Mo}(\text{AlH}_4)_5$.

In the case of the rare earth elements La, Pr, and Nd, the decomposition temperature of the respective alanate $\text{RE}(\text{AlH}_4)_3$ is uncertain because their synthesis was not yet successful. The synthesis was only attempted by Weidenthaler et al. via ball milling [149]. Since the reaction conditions of the ball-milling procedure are much more aggressive than those of the synthesis in solution, it does not seem surprising that the likely unstable alanates $\text{RE}(\text{AlH}_4)_3$ could not be obtained. Instead, the decomposition product REAlH_6 was synthesized [149]. However, $\text{Ce}(\text{AlH}_4)_3$ could be synthesized in solution and has a decomposition temperature of $-15\text{ }^\circ\text{C}$ [148]. The decomposition temperatures and behavior of CeAlH_6 and REAlH_6 ($\text{RE} = \text{La, Pr, Nd}$) are very similar [149]. Presumably, this similarity is not exclusive to the decomposition product MAlH_6 , but also includes the alanate $\text{RE}(\text{AlH}_4)_3$. Thus, for $\text{RE}(\text{AlH}_4)_3$, a decomposition temperature around $-15\text{ }^\circ\text{C}$ can be expected.

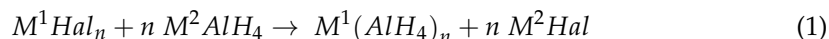
Attempts to synthesize $\text{V}(\text{AlH}_4)_3$, $\text{Ta}(\text{AlH}_4)_n$, $\text{Zn}(\text{AlH}_4)_2$, $\text{Cd}(\text{AlH}_4)_2$, $\text{Hg}(\text{AlH}_4)_2$, and $\text{Au}(\text{AlH}_4)_3$ were not successful. Even at temperatures as low as $-135\text{ }^\circ\text{C}$ (Hg [150]), $-120\text{ }^\circ\text{C}$ (Au [151]), and $-80\text{ }^\circ\text{C}$ (Cd [152], Ta [153], V [154], Zn [155]), the respective alanates were not obtained. Only the decomposition products in form of the hydrides (Hg [150], Cd [148,152], Zn [155]), the elements (Au [151]), or $\text{TaH}_{n-m}(\text{AlH}_4)_{5-n}$ [153,156] could be found. Hence, the existence of these alanates themselves could not be demonstrated and therefore is deemed to be questionable.

3.1.2. Synthesis

Most of the transition metal alanates reported in the literature were first synthesized in solution in the 1950s to 1970s. In the 2010s, the field of transition metal alanates was revived as new and already known alanates were prepared mechanochemically by ball milling.

Both approaches are usually carried out via a metathesis reaction (1). The most commonly used reactants are LiAlH_4 or NaAlH_4 (M^2AlH_4) and the respective transition metal halide (M^1Hal_x). Transition metal perchlorates [157,158] and boronates [159] can also

be employed as starting materials. Since transition metal alanates are sensitive to air and moisture, the synthesis must be performed under inert conditions [142].



For the synthesis in solution, ethereal solvents such as diethyl ether and tetrahydrofuran are used. On account of the instability of most transition metal alanates, the synthesis in solution is usually performed at temperatures between $-110\text{ }^\circ\text{C}$ and $-80\text{ }^\circ\text{C}$ [160]. The advantages of the synthesis in solution over the mechanochemical approach are the milder reaction conditions and the possibility of preparing pure alanates. Because of the mild reaction conditions, the synthesis in solution is applicable to all the transition metal alanates independently of their stability. The use of transition metal bromides and $LiAlH_4$ allows the synthesis of pure alanates as the transition metal alanates are insoluble and the by-product $LiBr$ is highly soluble in ethereal solutions [160].

Although the formation of a stable solvent adduct was only reported for $Sc(AlH_4)_3$ [147], it seems likely that other transition metal alanates form solvent adducts, too. This tendency toward adduct formation could hinder the preparation of pure, solvent free alanates and should be taken into consideration. The missing reports on solvent adducts can be explained by the largely insufficient characterization of the alanates in the 1950s to 1970s. In consequence of the instability of most transition metal alanates, the characterization often only involved the volumetric measurement of the hydrogen released during the decomposition, elemental analysis of the decomposed alanate, and possibly IR spectroscopy, XRD or DTA. These characterization techniques would not necessarily allow the determination of solvent adducts.

The mechanochemical approach involving ball milling was only used for alanates stable above room temperature until now. It only allows the synthesis of a mixture of the transition metal alanate and the respective by-product, provided the use of solvents is avoided.

Table 2 further summarizes the information provided in the literature on transition metal alanates. Since the existence of $Au(AlH_4)_3$, $Cd(AlH_4)_2$, $Co(AlH_4)_2$, $Hg(AlH_4)_2$, $Ni(AlH_4)_2$, $Ta(AlH_4)_n$, $V(AlH_4)_3$ and $Zn(AlH_4)_2$ is in doubt and $La(AlH_4)_3$, $Nd(AlH_4)_3$, $Pr(AlH_4)_3$, and $V(AlH_4)_3$ have not yet been synthesized, they are not included in Table 2.

3.1.3. Dehydrogenation and Hydrogenation Behavior

The dehydrogenation and even more so the hydrogenation behavior of the transition metal alanates has not yet been investigated in great detail. This situation is mainly a consequence of the instability of the alanates.

Based on investigations of the decomposition behavior of the alanates by volumetric hydrogen and in some cases DTA measurements, Soloveichik [160] categorized four groups of decomposition mechanisms in 1983 (see (2)–(5)). The mechanism of Group III is a special case of Group II, in which the decomposition of AlH_3 is catalyzed by the transition metal.

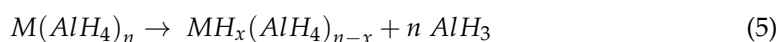
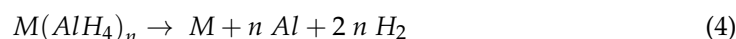
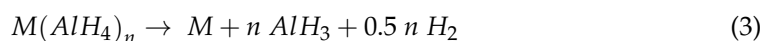
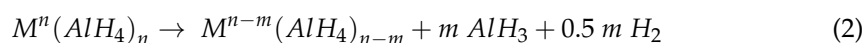


Table 2. Data of the known transition metal alانات—their hydrogen capacity (wt% H), decomposition temperature (T_{dec}), synthesis procedure, and the characterization techniques used. The hydrogen capacity corresponds to the pure alانات. The abbreviation EA stands for elemental analysis and the abbreviation VDH for volumetric determination of hydrogen released during the decomposition of the alانات.

Alانات	wt% H	T_d (°C)	Synthesis		Characterization Techniques	Ref
			Starting Materials	Procedure		
AgAlH ₄	2.9	−50	AgClO ₄ , LiAlH ₄ [157]	In solution (diethyl ether)	Conductometric titration [157] VDH [158]	[157,158]
Ce(AlH ₄) ₃	5.2	−15	Li ₃ CeBr ₆ , LiAlH ₄	In solution (diethyl ether)	VDH, EA	[148]
CeAlH ₆	3.5	100	CeCl ₃ , NaAlH ₄	High-energy ball milling under 1–15 bar hydrogen	DSC, thermolysis, XRD	[149]
CuAlH ₄	4.3	≤−80 [148]	CuI, LiAlH ₄ [161,162] Li ₂ CuBr ₄ , LiAlH ₄ [148]	In solution (tetrahydrofuran [161], diethyl ether [148,162])	VDH, EA [148,161,162] IR [161,162]	[148,161,162]
Eu(AlH ₄) ₂	3.8	100	EuCl ₂ , NaAlH ₄	High-energy ball milling under 1–15 bar hydrogen, no separate preparation of EuAlH ₅	DSC, thermolysis, XRD	[163]
EuAlH ₅	2.7	180				
Fe(AlH ₄) ₂	6.8	−125 [143] −70 [144] <RT [145]	FeCl ₃ , LiAlH ₄ [145,146,164] Li ₂ FeBr ₄ , LiAlH ₄ [148]	In solution (diethyl ether)	VDH, EA [144–146] IR [144] Thermolysis [145] DTA (not shown), XRD [146]	[143–146,148,164]
LaAlH ₆	3.5	100	LaCl ₃ , NaAlH ₄	High-energy ball milling under 1–15 bar hydrogen	DSC, thermolysis, XRD, ²⁷ Al-NMR	[149]
Mn(AlH ₄) ₂	6.9	−20	Li ₂ MnBr ₄ , LiAlH ₄	In solution (diethyl ether)	VDH, EA	[148]
Mo(AlH ₄) ₅	8.0	≤RT	No information	In solution (diethyl ether)	No information stated	[143]
Nb ₂ (AlH ₄) ₅	5.9	0 [165] >20 [166]	NbCl ₅ , LiAlH ₄	In solution (diethyl ether)	VDH, EA Thermolysis, DTA (not shown), XRD, IR [165]	[144,153,165,166]
Nb ₂ (AlH ₄) ₆	6.5	−50 [165] −40 < T_d < 20 [166]				
Nb ₂ (AlH ₄) ₇	7.0	−90 [165] −70 < T_d < −40 [166]				
NdAlH ₆	3.4	100	NdCl ₃ , NaAlH ₄	High-energy ball milling under 1–15 bar hydrogen	DSC, thermolysis, XRD	[149]
PrAlH ₆	3.5	100	PrCl ₃ , NaAlH ₄	High-energy ball milling under 1–15 bar hydrogen	DSC, thermolysis, XRD	[149]
Sc(AlH ₄) ₃ Et ₂ O	8.8	80	ScBr ₃ , LiAlH ₄	In solution (diethyl ether)	VDH, EA, IR, XRD, DTA, DTGA, MS	[147]
TaH ₂ (AlH ₄) ₂	4.1	60 [153] 130 [156]	TaCl ₅ , LiAlH ₄ [153] TaBr ₅ /TaCl ₅ , LiAlH ₄ [156]	In solution (diethyl ether)	VDH, EA Thermolysis [153,156] XRD, IR, RAMAN [156]	[153,156]
Ti(AlH ₄) ₄	9.4	−70 [146] −85 [167]	TiBr ₄ /TiCl ₄ , LiAlH ₄ [146] TiCl ₄ , LiAlH ₄ [167]	In solution (diethyl ether)	VDH, EA IR [144] DTA (not shown), XRD [146]	[144,146,167]
Y(AlH ₄) ₃	6.7	50 [168] 80 [169]	YBr ₃ , LiAlH ₄ [168] YCl ₃ , LiAlH ₄ [169]	In solution (diethyl ether) [168] High-energy ball milling under 80 bar hydrogen, no separate preparation of YAlH ₆ [169]	VDH, EA IR, DTA (not shown) [168] XRD, IR, TPD, MS, DSC, HP-DSC [169]	[168,169]
YAlH ₆	5.0	170 [169]				

Table 2. Cont.

Alaanate	wt% H	T _d (°C)	Synthesis		Characterization Techniques	Ref
			Starting Materials	Procedure		
Yb(AlH ₄) ₂	3.4	70	YbBr _x , LiAlH ₄	In solution (diethyl ether)	VDH, EA, DTA (not shown), XRD, IR	[144]
Yb(AlH ₄) ₃	4.6	100	YbCl ₃ , LiAlH ₄	High-energy ball milling under 100 bar hydrogen, no separate preparation of YbAlH ₆	XRD, IR, TGA-DSC-MS, HP-DSC	[170]
YbAlH ₆	2.9	180				
Zr(AlH ₄) ₄	7.5	<RT	Zr(BH ₄) ₄ , LiAlH ₄	In solution (diethyl ether)	EA	[159]

Regarding the decomposition mechanisms gathered by Soloveichik, it is notable that none of the decomposition mechanisms involve an intermediate of the form M_xAlH_y . This sort of intermediate was only known for $CuAlH_4$ [161] in 1983. However, the existence of M_xAlH_6 was deemed to be a unique feature of $CuAlH_4$ [160].

Nowadays, it is assumed that the dehydrogenation of most alanes involves such intermediates [142]. Thus, this phenomenon needs to be taken into account and investigated in respect of transition metal alanes on a regular basis. More recent findings seem to support this hypothesis as well. Weidenthaler [149] was able to synthesize $REAlH_6$ ($RE = Ce, La, Nd, Pr$), probably via unstable $RE(AlH_4)_3$ intermediates. Cao et al. could show a stepwise decomposition of $Y(AlH_4)_3$ [169] and $Yb(AlH_4)_3$ [170]. An intermediate formation of $MAlH_6$ during the dehydrogenation processes was proposed. Unfortunately, the formation of $MAlH_6$ could not be demonstrated beyond doubt. In the investigation of the thermal decomposition of $Eu(AlH_4)_2$ by Pommerin [163], an intermediate $EuAlH_5$ was found.

The characterization of the dehydrogenation behavior of transition metal alanes remains incomplete and leaves much to be discovered in future investigations. These tasks also include the thermodynamics, as only for $REAlH_6$ ($RE = Ce, La, Nd, Pr$) was a dehydrogenation enthalpy reported [149]. The presented value of about 30 kJ/mol H_2 is promising to obtain reversibility under benign conditions.

Successful rehydrogenation of a transition metal alane was only achieved in the case of $Y(AlH_4)_3$ [169]. Here, the first dehydrogenation step is reversible at 145 °C and 100 bar. The reversible hydrogen storage capacity of around 2.5 wt% corresponds to 75% of the theoretical storage capacity. It has to be noted that a mixture of $Y(AlH_4)_3$ and $LiCl$ was used for the investigation and not the pure alane. However, this discovery holds promise for discovering new intermediate hydrides for low-temperature applications.

3.2. Transition Metal Boranates

Metal borohydrides $M(BH_4)_n$ of alkali metals and alkaline-earth metals raise great interest, mainly because of their extremely high hydrogen densities, often above 10 wt% (e.g., $LiBH_4$ 13.8 wt%, $Mg(BH_4)_2$ 14.9 wt%). Their high decomposition temperatures and slow rehydrogenation kinetics demand tailoring before hydrogen storage applications are possible [171–173]. In contrast, transition metal boranates exhibit much lower decomposition temperatures while also maintaining high hydrogen densities. For instance, the onset decomposition temperature of $Zr(BH_4)_4$ (10.7 wt%) drops as low as 70–80 °C, which is much lower than that of $M(BH_4)_n$ of alkali metals and alkaline-earth metals (usually over 300 °C) [174].

3.2.1. Overview of Known Transition Metal Boranates

Since the 1940s, a number of transition metal boranates were synthesized and characterized to some extent. In Figure 12, an overview of the transition metal boranates described in the literature up to now is presented. The elements in the periodic table marked in red represent the corresponding boranates that are reported to decompose below room temperature. Boranates of the elements marked in green begin to decompose at room temperatures or above. Blue-marked elements depict the corresponding boranates whose existence is uncertain and/or questionable. Ruled markings indicate that the decomposition temperature is uncertain since conflicting information can be found in the literature.

The diagram shows that there is a correlation between the binary hydride gap and the low decomposition temperature of the corresponding transition metal boranates. In general, elements with stable binary hydrides tend to form transition metal boranates with higher stability (decompose at room temperatures or above), while boranates of elements that form less stable or unstable binary hydrides, like Fe, Co, Ni, etc., in most cases decompose below room temperature.

would be possible. In the end, both research groups failed to deliver clear evidence of the successful synthesis of the respected boranate. Since hard evidence of the existence of the compound is missing, its existence needs to be considered as uncertain.

Suárez-Alcántara and García [174] assumed that niobium boranate exists and should be rather stable, but the synthesis has not been attempted successfully yet.

For each of the following borohydrides, $\text{Ti}(\text{BH}_4)_3$, $\text{Ce}(\text{BH}_4)_3$, $\text{Eu}(\text{BH}_4)_n$, $\text{Y}(\text{BH}_4)_3$, $\text{Yb}(\text{BH}_4)_3$, and $\text{Th}(\text{BH}_4)_4$, a relatively wide temperature range is reported for the decomposition temperature, which may result from the different synthesis strategies applied. For example, Park et al. mentioned differences in the decomposition temperatures of ball-milled samples and those prepared from a gas solid reaction for $\text{Y}(\text{BH}_4)_3$ [190].

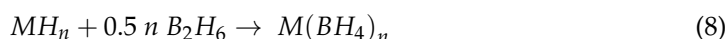
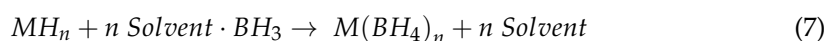
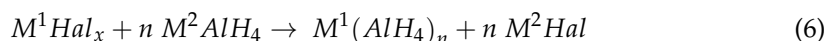
Attempts to synthesize AuBH_4 [191] and $\text{Au}(\text{BH}_4)_3$ [151] were not successful at temperatures as low as $-120\text{ }^\circ\text{C}$, which makes their existence questionable.

3.2.2. Synthesis

Most of the transition metal boranates reported in the literature were first synthesized in ethereal solution under cooling with dry ice or liquid nitrogen. Since the 2000s, a great interest in the field of transition metal boranates occurred, leading to an increase in the work regarding the synthesis of already known and new boranates. Moreover, the mechanochemical approach was also established for the synthesis of boranates.

Both synthesis approaches are usually carried out via a metathesis reaction (6). Since transition metal boranates are sensitive to air and moisture, the syntheses must be performed under inert conditions [174]. The most commonly used reactants are LiBH_4 or NaBH_4 and the respective transition metal halide (MHal_n) [174]. In some cases [192], even transition metal perchlorates can be employed as starting materials. For volatile boranates such as $\text{Zr}(\text{BH}_4)_4$ and $\text{Hf}(\text{BH}_4)_4$, a solid-state metathesis is also an option [193].

Another reaction pathway, which is often employed, is the reaction between transition metal hydrides and BH_3 -adducts in solvents such as dimethyl sulfide [194,195] or amines like triethyl amine [196,197] (7). The reaction of the transition metal hydride with diborane (B_2H_6) is also applicable for the synthesis of boranates (8) [190,198].



For the synthesis in solution, ethereal solvents such as diethyl ether, tetrahydrofuran, and dimethyl sulfide have been used. The advantages of the synthesis in solution over the mechanochemical approach are, on the one hand, the milder reaction conditions and, on the other hand, the prospect of being able to prepare pure boranates. Because of the differences in the solubility of the transition metal boranates and the starting materials ($\text{LiBH}_4/\text{NaBH}_4$, MHal_n), as well as the by-products ($\text{LiHal}/\text{NaHal}$), the separation of the boranate is possible. In this respect, solvent mixtures like dimethyl sulfide/toluene (20/80) can be beneficial. While the boranate dissolves by forming a soluble solvent adduct with the dimethyl sulfide, the by-product (LiCl/NaCl) remains insoluble [194,199–201].

The transition metal boranate mixtures obtained in ball-milling experiments can be purified by extraction with a solvent or solvent mixture [200,201].

Table 3 further summarizes the information provided in the literature on transition metal boranates. $\text{Au}(\text{BH}_4)_3$, $\text{Cr}(\text{BH}_4)_2$, and $\text{V}(\text{BH}_4)_3$ are not included in this table since their existence is in doubt. It has to be mentioned that the decomposition temperatures stated are obtained from the onset temperatures of the corresponding decomposition signals in the thermal measurements. If no value was found in the respective report, the onset temperature was determined by us from the shown graphs using the inflection tangent method [202].

Table 3. Data of the known transition metal boranates—their hydrogen capacity (wt% H), onset decomposition temperature (T_{dec}), synthesis procedure and techniques used for their characterization. The hydrogen capacity corresponds to pure boranate. The abbreviation EA stands for elemental analysis, VDH for volumetric determination of hydrogen released during the decomposition of the boranate, VPM for vapor pressure measurement, MP for magnetic properties and TPPA for temperature-programmed photographic analysis.

Boranate	wt% H	T_d (°C)	Synthesis		Characterization Techniques	Ref
			Starting Materials	Procedure		
Ag(BH ₄) ₂	3.28	−30	LiBH ₄ , AgClO ₄	In solution (diethyl ether)	VDH	[192]
Ce(BH ₄) ₂	6.55	200–251	CeH ₃ , S(CH ₃) ₂ *BH ₃ [195] LiBH ₄ , CeCl ₃ [203–205]	In solution (dimethyl sulfide-toluene mixture [195], toluene [203]) Extraction (dimethyl sulfide [203]) High-energy ball milling [204,205]	In situ XRD (synchrotron) [195,203], XRD [204,205], FT-IR [195,204,205], PCI [195], TG-DSC-MS [195,205], TG-DSC [203], DSC [204], MP [195]	[195,203–205]
Co(BH ₄) ₂	9.10	−20 [206]	CoCl ₂ /CoLi ₂ Br ₄ , LiBH ₄ [206] CoBr ₂ , LiBH ₄ [207]	In solution (diethyl ether)	EA [207]	[206,207]
CuBH ₄	5.14	0	LiBH ₄ , CuCl ₂ [208,209] LiBH ₄ , CuCl [210,211]	In solution (diethyl ether [208–210], THF/diethyl ether [211])	VDH, iodometry (Cu) [211]	[208–211]
Cd(BH ₄) ₂	5.67	75	LiBH ₄ , CdCl ₂ [212] LiBH ₄ /NaBH ₄ /KBH ₄ , CdCl ₂ [213]	High-energy ball milling	In situ XRD (synchrotron) [213], XRD [212,213], PCI [212], MS [212], DSC [212], TG-DSC [213]	[212,213]
Dy(BH ₄) ₃	5.84	250	DyH ₃ , S(CH ₃) ₂ *BH ₃	In solution (dimethyl sulfide-toluene mixture)	In situ XRD (synchrotron), FT-IR, PCI, TG-DSC-MS, MP	[195]
Eu(BH ₄) ₂	4.44	290–395	EuH ₂ , N(C ₂ H ₅) ₂ *BH ₃ [197] EuH ₂ , S(CH ₃) ₂ *BH ₃ [195] EuCl ₃ , LiBH ₄ [214] EuCl ₂ , LiBH ₄ [214]	In solution (N(C ₂ H ₅) ₂ *BH ₃ [197], dimethyl sulfide-toluene mixture [195], diethyl ether [214]) Extraction (dimethyl sulfide [214]) High-energy ball milling [214] Annealing [214]	In situ XRD (synchrotron) [195,197,214], XRD [197,214], FT-IR [195,197,214], Raman [197], PCI [195,214], TG-DSC-MS [195,214], DSC [197], MP [195]	[195,197,214]
Eu(BH ₄) ₃	6.16	<100 [215] 168 [216]	EuCl ₃ , LiBH ₄	High-energy ball milling	In situ XRD (synchrotron) [216], XRD [215,216], ATR/FT-IR [215,216], TG-DSC [215], TG-DSC-MS [216], SEM [215]	[215,216]
Er(BH ₄) ₃	5.71	245–264	ErH ₃ , S(CH ₃) ₂ *BH ₃ [195] ErCl ₃ , LiBH ₄ [217,218] ErCl ₃ , NaBH ₄ [218]	In solution (dimethyl sulfide-toluene mixture [195]) Extraction (dimethyl sulfide [217]) High-energy ball milling [217,218]	In situ XRD (synchrotron) [195,217], XRD [217,218], FT-IR [195,218], PCI [195,217,218], TG-DSC-MS [195,217], DSC [218], TPD-MS [217], MP [195]	[195,217,218]
Fe(BH ₄) ₂	9.43	−20 [206] −10 [164]	FeCl ₂ , LiBH ₄ [206] FeCl ₃ , LiBH ₄ [164]	In solution (diethyl ether)	VDH [164,206], EA [164]	[164,206]
Gd(BH ₄) ₃	5.99	250–262	GdH ₃ , S(CH ₃) ₂ *BH ₃ [194,195] GdCl ₃ , LiBH ₄ [200,219,220]	In solution (toluene or tetrahydrofuran [194], S(CH ₃) ₂ *BH ₃ -toluene mixture [200], dimethyl sulfide-toluene mixture [195]) extraction (dimethyl sulfide or tetrahydrofuran [194], dimethyl sulfide [200]) High-energy ball milling [200,219,220]	In situ XRD (synchrotron) [194,195,220], XRD [194,200,219,220], FT-IR [194,195,200,219,220], ¹ H-NMR [194], PCI [195,200,219,220], TG-DSC-MS [194,195,200], TG-DTA-MS [220], TPD-MS [200], DSC [220], TPPA [200], TEM [194], MP [195], conductivity measurements [220]	[194,195,200,219,220]
Hf(BH ₄) ₄	6.78	136.4 [221]	HfCl ₄ , LiBH ₄ [221–228] NaHfF ₅ , Al(BH ₄) ₃ [229]	Direct metathesis [221–226,229] In solution (diethyl ether [227,228])	VDH [222,229], EA [222,229], VPM [229], single crystal neutron diffraction [228], XRD [221], gas electron diffraction [225], DSC [221], TG-DSC-MS [221], IR [222,224,225], photoelectron spectroscopy [223], melting point [221,229], boiling point [229], C _p [221], S° [221], Δ _B H [221], NMR (¹ H [221,222,224,227], ¹¹ B [221,222,224]), DFT [221]	[221–229]

Table 3. Cont.

Boronate	wt% H	T _d (°C)	Synthesis		Characterization Techniques	Ref
			Starting Materials	Procedure		
Ho(BH ₄) ₃	5.77	252 [195] 236 [230]	HoH ₃ , S(CH ₃) ₂ *BH ₃ [195] HoCl ₃ , LiBH ₄ [230]	In solution (dimethyl sulfide-toluene mixture [195]) High-energy ball milling [230]	In situ XRD (synchrotron) [195], XRD [230], FT-IR [195,230], PCI [195], TG-DSC-MS [195], TG-DSC [230], MP [195]	[195,230]
La(BH ₄) ₃	6.59	242–258	LaH ₃ , S(CH ₃) ₂ *BH ₃ [195] LiBH ₄ , LaCl ₃ [203,205,231,232]	In solution (dimethyl sulfide-toluene mixture [195], toluene [203,231,232]) extraction with dimethyl sulfide [203,231,232] High-energy ball milling [205]	In situ XRD (synchrotron) [195,203], XRD [205], FT-IR [195,205], PCI [195], TG-DSC-MS [195,205], TG-DSC [203], MP [195]	[195,203,205,231,232]
Lu(BH ₄) ₃	3.94	220	LuH ₃ , S(CH ₃) ₂ *BH ₃	In solution (dimethyl sulfide-toluene mixture) High-energy ball milling [180,181,233,234]	In situ XRD (synchrotron), FT-IR, PCI, TG-DSC-MS, MP	[195]
Mn(BH ₄) ₂	9.53	125–150	MnCl ₂ , LiBH ₄ [180,181,201,233–236] MnCl ₂ , NaBH ₄ [180,237]	In solution (dimethyl sulfide-toluene mixture [201], diethyl ether [234,235]) Extraction (dimethyl sulfide [201,234,235], diethyl ether [237]) High-energy ball milling [236–238]	In situ XRD (synchrotron) [201,234,235], XRD [180,181,233,234,236–238], (ATR)-FT-IR [201,233,236–238], Raman [180,181,233,234], PCI [236–238], TG-MS [180,181,233], DSC [233,236], TG-DSC-MS [201,234,235,237,238], TDS-GC/MS [180,181], DFT [234], FE-SEM [237,238], ICP-OES [235]	[180,181,201,233–238]
Nd(BH ₄) ₃	6.41	235–245	NdH ₃ , S(CH ₃) ₂ *BH ₃	In solution (toluene or tetrahydrofurane [194], dimethyl sulfide-toluene mixture [195,239]) Extraction with dimethyl sulfide or tetrahydrofurane [194]	In situ XRD (synchrotron) [194,195,239], XRD [194], NPD [239], FT-IR [194,195], ¹ H-NMR [194], PCI [195], TG-DSC-MS [194,195,239], TEM [194], MP [195], DFT [239]	[194,195,239]
Ni(BH ₄) ₂	9.12	–20	NiCl ₂ , LiBH ₄	In solution (diethyl ether)	/	[206]
Np(BH ₄) ₄	4.30	<RT [240,241]	NpF ₄ , Al(BH ₄) ₃	Direct metathesis in glass tube	VPM [240], XRD [240,242], IR [241–243], Raman [241–243], EPR [242], C _p [243], S _c [243]	[240–243]
Pa(BH ₄) ₄	5.55	>RT	PaF ₄ , Al(BH ₄) ₃	Direct metathesis in glass tube	XRD [241,242], IR [241,242], Raman [241,242], EPR [242]	[241,242]
Pr(BH ₄) ₃	6.52	236–252	PrH ₃ , S(CH ₃) ₂ *BH ₃ [195,239] PrCl ₃ , LiBH ₄ [217]	In solution (dimethyl sulfide-toluene mixture [195,239], diethyl ether [217]) Extraction (dimethyl sulfide [217])	In situ XRD (synchrotron) [195,217,239], XRD [217], NPD [239], FT-IR [195], PCI [195,217], TG-DSC-MS [195,217,239], TPD-MS [217], MP [195], DFT [239]	[195,217,239]
Pu(BH ₄) ₄	4.19	<RT [241]	PuF ₄ , Al(BH ₄) ₃	Direct metathesis in glass tube	XRD [241,242], IR [241,242], Raman [241,242], EPR [242]	[241,242]
Sc(BH ₄) ₃	13.52	207–215	ScCl ₃ , LiBH ₄	High-energy ball milling	XRD, Raman, TDS-GC/MS	[179–181,244]
Sm(BH ₄) ₂	4.48	300–318	SmH ₂ , S(CH ₃) ₂ *BH ₃ [194,195] SmCl ₃ , LiBH ₄ [214–216]	In solution (toluene or tetrahydrofurane [194], dimethyl sulfide-toluene mixture [195], diethyl ether [214]) Extraction (dimethyl sulfide or tetrahydrofurane [194], dimethyl sulfide [214]) High-energy ball milling [215,216]	In situ XRD (synchrotron) [194,195,214,216], XRD [194,214–216], ATR/FT-IR [194,195,214–216], ¹ H-NMR [194], PCI [195,214], TG-DSC-MS [194,195,214–216], SEM [215], TEM [194], MP [195]	[194,195,214–216]
Sm(BH ₄) ₃	6.21	170 [215] 168 [216]	SmCl ₃ , LiBH ₄	High-energy ball milling	In situ XRD (synchrotron) [216], XRD [215,216], ATR/FT-IR [215,216], TG-DSC-MS [215,216], SEM [215]	[215,216]
Tb(BH ₄) ₃	5.95	250 [195] 243 [215]	TbH ₃ , S(CH ₃) ₂ *BH ₃ [195] TbCl ₃ , LiBH ₄ [215]	In solution (dimethyl sulfide-toluene mixture) [195] High-energy ball milling [215]	In situ XRD (synchrotron) [195], XRD [215], ATR/FT-IR [195,215], PCI [195], TG-DSC-MS [195,215], SEM [215], MP [195]	[195,215]
Th(BH ₄) ₄	5.53	>150–203 [229, 241,245]	ThF ₄ , Al(BH ₄) ₃	Direct metathesis in glass tube	VDH [229], EA [229], VPM [229], XRD [241], IR [241,245], Raman [241], TG [245], melting point [229]	[229,241,245]
Ti(BH ₄) ₃	13.09	<RT–78 [229, 246,247]	TiCl ₄ , LiBH ₄ [229,247] TiCl ₃ , LiBH ₄ [247–249] TiF ₃ , LiBH ₄ [246]	Direct metathesis [229] Mixing in mortar [247] High-energy ball milling [246–249]	VDH [229,248,249], EA [229,248,249], XRD [246], TG-DSC-MS [246], TG [247], MS [247], (FT)-IR [246,247,249]	[229,246–249]

Table 3. Cont.

Borane	wt% H	T _d (°C)	Synthesis		Characterization Techniques	Ref
			Starting Materials	Procedure		
Tm(BH ₄) ₃	5.71	253	TmH ₃ , S(CH ₃) ₂ *BH ₃	In solution (dimethyl sulfide-toluene mixture)	In situ XRD (synchrotron), FT-IR, PCI, TG-DSC-MS, MP	[195]
U(BH ₄) ₄	5.42	<RT [241,250]	UF ₄ , Al(BH ₄) ₃	Direct metathesis in glass tube	VDH [250], EA [250,251], VPM [250,251], XRD [241,252], IR [241,245,252,253], Raman [241], thermographic investigation [252]	[241,245,250–253]
Y(BH ₄) ₃	9.06	191–276	YCl ₃ , LiBH ₄ [181,190,199,200,254–258] YH ₃ , B ₂ H ₆ [190] YH ₃ , S(CH ₃) ₂ *BH ₃ [194] YCl ₃ , Li ¹¹ BD ₄ [259] YCl ₃ , LiBD ₄ [260]	High-energy ball milling [181,190,200,254–260] In solution (toluene or tetrahydrofuran [194], dimethyl sulfide-borane complex in toluene [200], diethyl ether [199,255]) Extraction (dimethyl sulfide or tetrahydrofuran [194], dimethyl sulfide [199,200])	EA [258], in situ XRD (synchrotron) [190,194,199,200,254,259], XRD [181,190,194,199,200,254–260], PND [259], FT-IR [194,257,258,260], Raman [181,255,258,260], NMR (¹ H [194,258], ¹¹ B [258], ¹ H-MAS [256], ¹¹ B-MAS [254], ⁸⁹ Y-MAS [256]), PCI [200,255,257], DSC [190,199,257], DSC-TPD [259], TG [199], TG-DSC-MS/FT-IR [256,258,260], TG-DSC [254], TG-MS [181,190], TG-DSC-MS [194,200], TDS-GC [181], TPD-MS [181,200], TG-DTA-MS [255], TPPA [199,200], SEM-EDS [258], TEM [194], BET [190]	[181,190,194,199,200,254–260]
Yb(BH ₄) ₂	3.98	329–353	YbH ₃ , S(CH ₃) ₂ *BH ₃ [194] YbH ₂ , S(CH ₃) ₂ *BH ₃ [195] YbCl ₃ , LiBH ₄ [216,261]	In solution (toluene or tetrahydrofuran [194], dimethyl sulfide-toluene mixture [195]) Extraction (dimethyl sulfide or tetrahydrofuran [194]) High-energy ball milling [216,261]	In situ XRD (synchrotron) [194,195,216,261], XRD [194,216,261], PND [261], ATR/FT-IR [194,195,216], Raman [261], ¹ H-NMR [194], PCI [195], TG-DSC-MS [194,195], TG-DSC [261], TG-DSC-MS [216], TPD [261], TEM [194], MP [195]	[194,195,216,261]
Yb(BH ₄) ₃	5.56	122–150	YbCl ₃ , LiBH ₄	High-energy ball milling	In situ XRD (synchrotron) [216,261], XRD [215,216,261], PND [261], Raman [261], ATR/FT-IR [215,216], TG-DSC [261], TG-DSC-MS [215,216], TPD [216,261], SEM [215]	[215,216,261]
Zr(BH ₄) ₄	10.71	72 [179,181,262] 82 [263] 130.4 [221]	ZrCl ₄ , NaBH ₄ [179] ZrCl ₄ , LiBH ₄ [159,164,179,181,193,221–225,227,262–270] NaZrF ₅ , Al(BH ₄) ₃ [159,229] KZrF ₅ , Al(BH ₄) ₃ [159] Na ₂ ZrF ₆ , Al(BH ₄) ₃ [243] Zr(iso-propylate) ₄ , B ₂ H ₆ [159]	Direct metathesis [159,193,221–225,229,243,264–266] In solution (diethyl ether) [159,227,268–270] High-energy ball milling [179,181,262,263,267]	VDH [159,222,229], EA [159,222,229], VPM [229,268], in situ XRD (synchrotron) [267], XRD [179,181,221,262,263,267], electron diffraction [225], (FT-IR) [222,224,225,243,245,263–265,267,268,270], Raman [179,181,262], NMR (¹ H [221,222,227,269], ¹¹ B [221,222,224,269], ⁹¹ Zr [221,269]), photoelectron spectroscopy [223], DSC [221,263], TPD-GC [179,181,262], TG-MS [179,181,262], TG-DSC-MS [221], melting point [159,221,263,268], boiling point [229], C _p [221], S° [221], Δ ₈ H [221], DFT [221,262], MDS [271]	[159,179,181,193,221–225,227,229,243,245,262–271]

3.2.3. Dehydrogenation and Hydrogenation Behavior

The dehydrogenation and hydrogenation behavior of some transition metal boranates has been investigated in great detail (e.g., $\text{Y}(\text{BH}_4)_3$ [255,257,272] and $\text{Mn}(\text{BH}_4)_2$ [233,235,273,274]). There is, however, a lack of investigations regarding the majority of the known transition metal boranates [174]. Although for some boranates DFT or other calculations exist (as for Sc, Ti and Zr [275]), they have usually not been validated by experimental investigations. The numerous dehydrogenation reactions of transition metal boranates can occur via a great variety of intermediates. The type of intermediate formed depends on the considered transition metal and its properties, such as its oxidation state in the boranate, the one in the corresponding decomposition product, and its electronegativity. Unfortunately, it is not possible to summarize the known individual decomposition reactions by stating general decomposition pathways.

The decomposition is kinetically hindered in general and occurs at higher temperatures than the equilibrium ones. If the decomposition reactions are thermodynamically controlled, the solid decomposition products for most transition metals would be borides or hydrides instead of the elemental transition metals and boron (and, of course, hydrogen), since these compounds are energetically preferred over the pure elements for most transition metals. However, due to the relatively low desorption temperatures during decomposition, crystallization associated with the formation of metal borides or hydrides often cannot occur for kinetic reasons. However, in practice, the borides and the mixtures of borides and hydrides can often be rehydrogenated more easily than the mixtures of the elements, so that it is advantageous, if the decomposition of the transition metal borohydride does not go all the way to the elemental transition metal and boron but to the corresponding borides [276].

Unfortunately, the decomposition reactions can involve the release of diborane, which will be discussed in the next section [276].

3.2.4. Stability and Diborane Formation

As already discussed by Suárez-Alcántara and García [174], the evolution of diborane often depends on several experimental factors, such as the synthesis route (e.g., ball milling, in solution) [275], including the purification process [174], the hydrogen back pressure and heating rate during dehydrogenation (a high back pressure [257,276] and a small heating rate [277] prevent diborane formation) and the type of modification (molecular or salt-like crystalline compounds) [275]. In complex mixtures of transition metal borohydrides and mixtures of transition metal borohydrides and other transition metals [278], the evolution of diborane may also depend on the intricate interaction with the various transition metal components. In addition to the conditions already summarized by Suárez-Alcántara and García, Nakamori et al. observed a dependency on the Pauling electronegativity of the transition metal. For transition metals with a Pauling electronegativity χ_P smaller than 1.5 [180,181,262], no diborane release is observed. Based on this finding, Harrison and Thonhauser plotted the relative diborane content in the released gas mixture of some boranates after decomposition (defined as the ratio between the integrated MS-diborane signal to the integrated MS-hydrogen signal and normalized to a value of 1 for $\text{Al}(\text{BH}_4)_3$) against the χ_P of the contained metal [278] but did not obtain a clear correlation. Instead, they found an exponential correlation between the calculated (via DFT) enthalpies of the formation of the boranates and the diborane release. While Vajo et al. [172,173] showed that it is possible to destabilize boranates by adding additional reactants during decomposition, Harrison and Thonhauser [278] were able to show by theoretical means that it is possible to stabilize boranates by adding transition metals to prevent the development of diborane. They calculated that Sc-stabilized $\text{Al}(\text{BH}_4)_3$ should not emit diborane during decomposition on thermodynamic grounds. Roedern and Jensen observed similar effects by adding alkali and alkaline-earth metal boranates to manganese boranate [235].

In principle, diborane can decompose spontaneously into the elements above 50 °C, but the reaction is strongly kinetically hindered [275]. Consequently, higher decomposition

temperatures should reduce the presence of diborane, because even if it is formed, it will presumably quickly decompose to boron and hydrogen [174,275,279].

In 2006, Nakamori et al. demonstrated the existence of a correlation between the Pauling electronegativity χ_P of the metal of a boranate and the decomposition temperature of the boranate T_d [262]. Suárez-Alcántara and García expanded the plot to bimetallic borohydrides using an approach reported by Li et al. to calculate an average value for the χ_P [174,280]. Unfortunately, the data used are inconsistent, as Suárez-Alcántara and García did not differentiate between the peak and onset temperatures and the data points shown even display a significant amount of scatter despite being logarithmically plotted. We decided to replot the χ_P values (taken from [281]) of the transition metal boranates versus T_d , the direct proportionally. Only the boranates for which clear values are stated in the literature or a clear graph suitable for determining the decomposition onset temperature were considered. If several, differing values were published, the arithmetic mean was used and the span of the (min, max) values is shown in the graph as error bars. As can be seen in Figure 13, the lanthanoid boranates have nearly similar χ_P , which appears to be a consequence of the lanthanoid contraction [282]. This is why we used the arithmetic means of χ_P and T_d for those boranates with the oxidation states +II and +III. Otherwise, the lanthanoids would be over-represented in the fit procedure because of the large number of values with nearly the same χ_P and differing T_d values. Furthermore, $Ti(BH_4)_3$, $Hf(BH_4)_4$ and $Zr(BH_4)_4$ seem to be outliers, as can be seen in Figure 13 (red dots). It can be assumed that their decomposition temperatures deviate from those of the other boranates because they do not possess a salt-like (ionic) crystal structure but rather a molecular one [174,276]. This fact seems to be unimportant for the decomposition of the molecular $Th(BH_4)_4$, which exhibits a decomposition temperature as high as expected for ionic boranates. As a result, we excluded only the values of $Ti(BH_4)_3$, $Hf(BH_4)_4$ and $Zr(BH_4)_4$ in our fit (Figure 13). The equation describing our fit function is given by:

$$T_d/K = -363.2 \chi_P + 949.2 \quad (9)$$

with an corrected R^2 value of 0.97596. The much improved R^2 value for the assumption of the simpler direct proportional correlation compared to the logarithmic fit in Ref. [174] can be seen as a consequence of the restriction to the most reliable data.

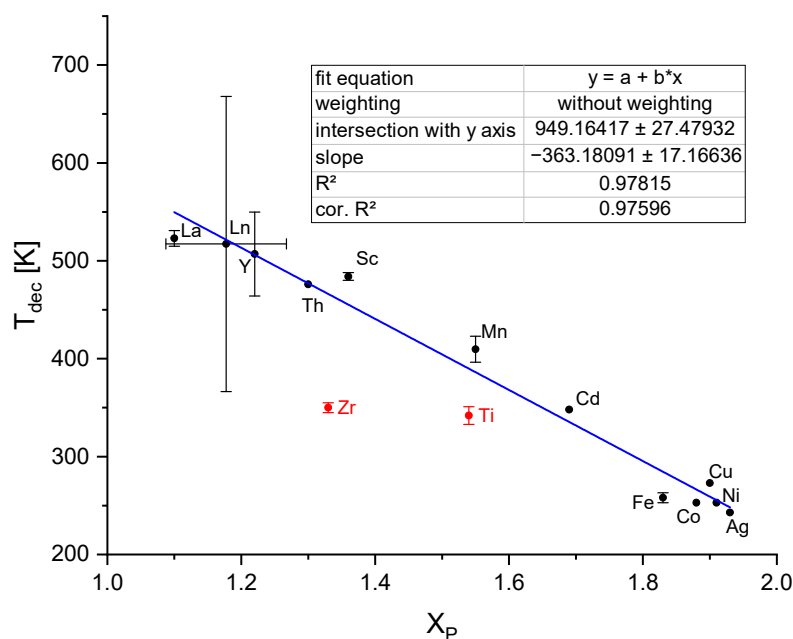


Figure 13. Fit of the decomposition temperature values of transition metal boranates (without the respective values for Ti, Hf and Zr boranate (red dots)).

Different explanations for the decrease of T_d with increasing χ_P exist [174]. Callini et al. [283] explained this result by the strength of the charge transfer from the metal cation to the tetrahydridoborate ion. In case of high values for χ_P , there is a small charge transfer to the anion and, in turn, a strong distortion of the (BH_4^-) units, resulting in low stability combined with diborane emission [283]. This could also be explained by the distorted orbitals of the borohydride anionic molecule [283] found in the simulation performed by Du et al. [284].

4. Summary and Perspective

In this review, the development status of unstable metal hydrides for possible on-board hydrogen storage based on classic metal hydrides is reported and potential materials for the development of unstable complex metal hydride systems based on alanates or boranates have been laid out (see schematic overview in Table 4). AB₂-type Laves phase alloys like TiCr₂- and ZrFe₂-based alloys display suitable plateau pressures and tentative tests on high-pressure tank systems based on these alloys have already been conducted. However, because of the high atomic weight of transition metal elements, the hydrogen capacity of these classic metal hydrides is usually limited to ~2 wt%, which prohibits their large-scale commercialization in fuel cell vehicles. Vanadium-based BCC alloys display much higher hydrogen storage capacity (>3 wt%), while the desorption plateau pressures are far below those believed to be needed for hybrid tank systems, which leads to the incomplete dehydrogenation of the alloys under certain conditions, resulting in relatively low reversible capacities. Through decades of effort, the hydrogen storage performances of these intermetallic compounds have been effectively improved and some characteristics can even meet parts of the requirements of high-pressure MH tanks. Up to now, however, none of them has met the DOE 2020–2025 targets and major improvements are required to meet those. In this regard, unstable complex hydrides like transition metal alanates and borohydrides can be very interesting materials in terms of the high hydrogen content and rich chemical diversity. In contrast to the main group of complex metal hydrides, the known transition complex metal hydrides, i.e., mainly boranates and alanates, show very little stability. With regards to the necessary thermodynamic properties for solid-state hydrogen storage, the current transition metal complex hydrides need to be regarded as non-suitable for practical applications. However, by creating mixed systems, they may offer a valuable tool box for the design of systems with the desired properties. Efforts to update the information on these complex metal hydrides in respect to new synthesis procedures and characterization techniques can supply fundamental knowledge for the task of designing viable solid-state hydrogen storage systems.

Table 4. Comparison of different types of metal hydrides.

Categories	Types	wt% H	Thermodynamics	Kinetics
AB ₂ -type Laves phase alloys	TiCr ₂ -based	<2	Most desorbing equilibrium pressure > 1.0 MPa at 298 K	Most desorption finishes within 5 min
	ZrFe ₂ -based	<2	Most desorbing equilibrium pressure > 1.0 MPa at 298 K	Most desorption finishes within 5 min
Solid solution alloys	Vanadium-based	>3	Most desorbing equilibrium pressure < 0.1 MPa at 298 K	Most desorption finishes within 10 min
Complex hydrides	Transition metal alanates	Most > 4	Most desorbing under −50 °C	Unknown
	Transition metal boranates	Most > 5	Most desorbing under 0 °C	Unknown

Materials under high-pressure conditions may show physical and chemical properties strongly deviating from the ambient pressure ones, which may create opportunities for discovering novel metastable materials with beneficial properties [285]. The pressure range up to the anticipated level of 70 MPa for compressed hydrogen in fuel cell vehicles is large enough to expect the design of a significant number of new reversible hydrogen storage materials. For instance, ZrFe₂ alloy does not show any hydrogen storage properties

under moderate conditions but becomes a good hydrogen absorber at a high pressure over 100 MPa. YNi_5 , LaPt_5 and ThNi_5 alloys also only start to absorb hydrogen at high pressures up to 155 MPa [286]. However, conventional intermetallic compounds are usually composed of transition metals with heavy atomic weights. A higher capacity can only be achieved in alloys composed of light elements. To achieve higher capacities, alloys containing transition and non-transition elements should be considered. To ensure excellent reversibility, candidates should have a stable structure under high pressure. For example, light REM_{2-3} alloys consisting of rare earth elements ($\text{RE} = \text{Y, La, Ce, Pr, Nd, etc.}$), transition metal elements (TM) and non-transition metal elements ($\text{M} = \text{Al, Si, etc.}$) have a stable structure even under a high pressure up to several GPa. LaAl_2 and CeAl_2 alloys have the C15 (MgCu_2 type, SG Fd3m) structure and are stable up to pressures over 20 GPa [287]. Rare earth trialuminides, REAl_3 ($\text{RE} = \text{La-Yb}$) alloys exhibit hexagonal DO_{19} -type (Ni_3Sn , SGP63/mmc), and the cubic environment of the atoms increases with the increase in the atomic number or decrease in the atomic radii of the rare earth elements as a function of pressure [288,289]. However, up to now, few studies concentrated on the hydrogen storage properties of these alloys. More attempts should be conducted under pressure up to 100 MPa or even higher.

Explorations solely relying on experimental approaches are time-consuming and inefficient. It is now well established that many important materials' properties can be predicted through computational means. The heat of formation (ΔH) is the key quantity to predict the stability of transition metal hydrides. Griessen et al. [290,291] calculated the ΔH of the transition metal hydrides A_5BH_x , A_2BH_x , AB_2H_x , AB_5H_x ($\text{A} = \text{Sc, Ti, V, Y, Zr, Nb, La, Hf, Ta, Ni, Pd}$; $\text{B} = \text{transition metal}$) using a semi-empirical model based on the electronic structure of the host alloy. Among the 1380 possible compounds, there are 44 metal hydrides with an appropriate heat of formation between -12 and -25 kJ/mol H_2 [291]. However, semi-empirical models are only effective for predicting the conventional intermetallic compounds comprising 3d, 4d and 5d transition metals. On the other hand, predictions of the hydrogen storage performances by conducting true ab initio calculations or such based on density functional theory are also feasible [292]. In the field of hydrogen storage materials, high-throughput computational hits were confirmed by experimental works [293,294]. Through the high-throughput ab initio computational approach, Alapati et al. [293] examined the potential utility for hydrogen storage of a large set of destabilized metal hydride reactions for which thermodynamic data had previously been unavailable. These methods are able to find many promising reactions with favorable reaction enthalpies ($20 \text{ kJ/mol H}_2 \leq \Delta H \leq 25 \text{ kJ/mol H}_2$) and high hydrogen storage capacities ($>7 \text{ wt\%}$) [293–295]. Lu et al. [294] experimentally demonstrated one of the predicted reactions ($\text{LiNH}_2 + \text{MgH}_2 \rightarrow \text{LiMgN} + 2\text{H}_2$) and found that the binary nitride LiMgN can be hydrogenated under 14 MPa hydrogen pressure at 433 K with TiCl_3 as a catalyst. The TGA results showed that a reversible capacity of 8 wt% H_2 is stored in TiCl_3 -doped LiMgN during the hydrogenation process. Akbarzadeh et al. [296] developed a practical formalism for studying phase diagrams of multicomponent systems through density functional theory calculations, which can predict thermodynamically favorable hydrogen storage reactions for a given multicomponent system without having to explicitly enumerate the possible reaction pathways, and optimize the hydrogen storage capacity within a given window of temperatures and pressures. Wolverton et al. [297] proposed to discover novel hydrogen storage materials through the atomic-scale computational approach, which provides reasonably accurate enthalpies compared to experimentally measured values across a series of metal hydrides. These results impressively demonstrate the solid guidance that computational studies can provide for the development of suitable high-equilibrium pressure hydrides, be it for systems generated by alloying or by mixing complex metal hydrides.

Funding: This research was supported by the National Natural Science Foundation of China, grant numbers 52271221, 51801107. In addition to the basic funding of the Max Planck Society, M.F. and

F.M. acknowledge partial funding by the Deutsche Forschungsgemeinschaft (DFG, German Research Foundation, grant number 449160425). The APC was funded by Project Deal.

Acknowledgments: F.H. and K.B. thank K. Bohmhammel for numerous fruitful discussions.

Conflicts of Interest: The authors declare no conflict of interest.

References

- Schlapbach, L.; Züttel, A. Hydrogen-storage materials for mobile applications. *Nature* **2001**, *414*, 353–358. [CrossRef] [PubMed]
- Marbán, G.; Valdés-Solís, T. Towards the hydrogen economy? *Int. J. Hydrogen Energy* **2007**, *32*, 1625–1637. [CrossRef]
- Wu, Y.; Ghalkhani, M.; Ashrafzadeh Afshar, E.; Karimi, F.; Xia, C.; Le, Q.V.; Vasseghian, Y. Recent progress in Biomass-derived nanoelectrocatalysts for the sustainable energy development. *Fuel* **2022**, *323*, 124349. [CrossRef]
- Bockris, J.O. The hydrogen economy: Its history. *Int. J. Hydrogen Energy* **2013**, *38*, 2579–2588. [CrossRef]
- Hwang, H.T.; Varma, A. Hydrogen storage for fuel cell vehicles. *Curr. Opin. Chem. Eng.* **2014**, *5*, 42–48. [CrossRef]
- Eberle, U.; Felderhoff, M.; Schüth, F. Chemical and physical solutions for hydrogen storage. *Angew. Chem. Int. Ed. Engl.* **2009**, *48*, 6608–6630. [CrossRef] [PubMed]
- Satyapal, S.; Petrovic, J.; Read, C.; Thomas, G.; Ordaz, G. The U.S. Department of Energy’s National Hydrogen Storage Project: Progress towards meeting hydrogen-powered vehicle requirements. *Catal. Today* **2007**, *120*, 246–256. [CrossRef]
- Heinemann, N.; Alcalde, J.; Miodic, J.M.; Hangx, S.J.T.; Kallmeyer, J.; Ostertag-Henning, C.; Hassanpouryouzband, A.; Thaysen, E.M.; Strobel, G.J.; Schmidt-Hattenberger, C.; et al. Enabling large-scale hydrogen storage in porous media—The scientific challenges. *Energy Environ. Sci.* **2021**, *14*, 853–864. [CrossRef]
- Durbin, D.J.; Malardier-Jugroot, C. Review of hydrogen storage techniques for on board vehicle applications. *Int. J. Hydrogen Energy* **2013**, *38*, 14595–14617. [CrossRef]
- Zohuri, B. *Hydrogen Energy: Challenges and Solution for a Cleaner Future*; Springer International Publishing: Cham, Switzerland, 2019.
- Yoshida, T.; Kojima, K. Toyota MIRAI Fuel Cell Vehicle and Progress toward a Future Hydrogen Society. *Electrochem. Soc. Interface* **2015**, *24*, 45–49. [CrossRef]
- Takeichi, N. “Hybrid hydrogen storage vessel”, a novel high-pressure hydrogen storage vessel combined with hydrogen storage material. *Int. J. Hydrogen Energy* **2003**, *28*, 1121–1129. [CrossRef]
- Mori, D.; Hirose, K. Recent challenges of hydrogen storage technologies for fuel cell vehicles. *Int. J. Hydrogen Energy* **2009**, *34*, 4569–4574. [CrossRef]
- Mori, D.; Hirose, K.; Haraikawa, N.; Takiguchi, T.; Shinozawa, T.; Matsunaga, T.; Toh, K.; Fujita, K.; Kumano, A.; Kubo, H. *SAE Technical Paper Series*; SAE International: Warrendale, PA, USA, 2007.
- Kojima, Y.; Kawai, Y.; Towata, S.; Matsunaga, T.; Shinozawa, T.; Kimbara, M. Development of metal hydride with high dissociation pressure. *J. Alloys Compd.* **2006**, *419*, 256–261. [CrossRef]
- Matsunaga, T.; Kon, M.; Washio, K.; Shinozawa, T.; Ishikiriya, M. TiCrVMo alloys with high dissociation pressure for high-pressure MH tank. *Int. J. Hydrogen Energy* **2009**, *34*, 1458–1462. [CrossRef]
- Mori, D.; Haraikawa, N.; Kobayashi, N.; Kubo, H.; Toh, K.; Tsuzuki, M.; Shinozawa, T.; Matsunaga, T. High-pressure metal hydride tank for fuel cell vehicles. *MRS Online Proc. Libr.* **2005**, *884*, 72–78. [CrossRef]
- Xu, Y.-H.; Chen, C.-P.; Geng, W.-X.; Wang, Q.-D. The hydrogen storage properties of Ti–Mn-based C14 Laves phase intermetallics as hydrogen resource for PEMFC. *Int. J. Hydrogen Energy* **2001**, *26*, 593–596. [CrossRef]
- Young, K.; Ouchi, T.; Fetcenko, M.A. Pressure–composition–temperature hysteresis in C14 Laves phase alloys: Part 1. Simple ternary alloys. *J. Alloys Compd.* **2009**, *480*, 428–433. [CrossRef]
- Lototsky, M.V.; Tolj, I.; Pickering, L.; Sita, C.; Barbir, F.; Yartys, V. The use of metal hydrides in fuel cell applications. *Prog. Nat. Sci. Mater. Int.* **2017**, *27*, 3–20. [CrossRef]
- Marques, F.; Balcerzak, M.; Winkelmann, F.; Zepon, G.; Felderhoff, M. Review and outlook on high-entropy alloys for hydrogen storage. *Energy Environ. Sci.* **2021**, *14*, 5191–5227. [CrossRef]
- Shoemaker, D.P.; Shoemaker, C.B. Concerning atomic sites and capacities for hydrogen absorption in the AB₂ Friauf-Laves phases. *J. Less-Common Met.* **1979**, *68*, 43–58. [CrossRef]
- Westlake, D.G. Site occupancies and stoichiometries in hydrides of intermetallic compounds: Geometric considerations. *J. Less-Common Met.* **1983**, *90*, 251–273. [CrossRef]
- Westlake, D.G. Hydrides of intermetallic compounds: A review of stabilities, stoichiometries and preferred hydrogen sites. *J. Less-Common Met.* **1983**, *91*, 1–20. [CrossRef]
- Bodega, J.; Fernández, J.F.; Leardini, F.; Ares, J.R.; Sánchez, C. Synthesis of hexagonal C14/C36 and cubic C15 ZrCr₂ Laves phases and thermodynamic stability of their hydrides. *J. Phys. Chem. Solids* **2011**, *72*, 1334–1342. [CrossRef]
- Merlino, R.; Luna, C.R.; Juan, A.; Pronato, M.E. A DFT study of hydrogen storage in Zr(Cr_{0.5}Ni_{0.5})₂ Laves phase. *Int. J. Hydrogen Energy* **2016**, *41*, 2700–2710. [CrossRef]
- Ivey, D.G.; Northwood, D.O. Storing Hydrogen in AB₂ Laves-Type Compounds. *Z. Phys. Chem.* **1986**, *147*, 191–209. [CrossRef]
- Johnson, J.R.; Reilly, J.J. Reaction of hydrogen with the low-temperature form (C15) of titanium-chromium (TiCr₂). *Inorg. Chem.* **1978**, *17*, 3103–3108. [CrossRef]

29. Johnson, J.R. Reaction of hydrogen with the high temperature (C14) form of TiCr_2 . *J. Less-Common Met.* **1980**, *73*, 345–354. [[CrossRef](#)]
30. Klyamkin, S. Effect of substitution on F.C.C. and B.C.C. hydride phase formation in the $\text{TiCr}_2\text{-H}_2$ system. *Int. J. Hydrogen Energy* **1999**, *24*, 149–152. [[CrossRef](#)]
31. Murashkina, T.L.; Syrtanov, M.S.; Laptev, R.S.; Stepanova, E.N.; Lider, A.M. Structure and defects evolution at temperature and activation treatments of the TiCr_2 intermetallic compound of Laves phase C36-type. *Int. J. Hydrogen Energy* **2019**, *44*, 10732–10743. [[CrossRef](#)]
32. Murashkina, T.L.; Syrtanov, M.S.; Laptev, R.S.; Lider, A.M. Cyclic stability of the C36-type TiCr_2 Laves phase synthesized in the abnormal glow discharge plasma under hydrogenation. *Int. J. Hydrogen Energy* **2019**, *44*, 6709–6719. [[CrossRef](#)]
33. Murashkina, T.L.; Syrtanov, M.S.; Shabunin, A.S.; Laptev, R.S. The Synthesis Method of Intermetallic Alloys Based on Ti–Cr with C14 and C36 Laves Phases for Hydrogen Storage. *J. Surf. Investig. X-Ray Synchrotron Neutron Tech.* **2019**, *13*, 146–153. [[CrossRef](#)]
34. Moriwaki, Y.; Gamo, T.; Iwaki, T. Control of hydrogen equilibrium pressure for C14-type laves phase alloys. *J. Less-Common Met.* **1991**, *172–174*, 1028–1035. [[CrossRef](#)]
35. Nagasako, N.; Fukumoto, A.; Miwa, K. First-principles calculations of C14-type Laves phase Ti–Mn hydrides. *Phys. Rev. B* **2002**, *66*, 155106. [[CrossRef](#)]
36. Kandavel, M.; Bhat, V.V.; Rougier, A.; Aymard, L.; Nazri, G.-A.; Tarascon, J.-M. Improvement of hydrogen storage properties of the AB_2 Laves phase alloys for automotive application. *Int. J. Hydrogen Energy* **2008**, *33*, 3754–3761. [[CrossRef](#)]
37. Li, F.; Zhao, J.; Tian, D.; Zhang, H.; Ke, X.; Johansson, B. Hydrogen storage behavior in C15 Laves phase compound TiCr_2 by first principles. *J. Appl. Phys.* **2009**, *105*, 43707. [[CrossRef](#)]
38. Nong, Z.-S.; Zhu, J.-C.; Cao, Y.; Yang, X.-W.; Lai, Z.-H.; Liu, Y. A first-principles study on the structural, elastic and electronic properties of the C14 Laves phase compounds TiX_2 ($X = \text{Cr, Mn, Fe}$). *Phys. B Condens. Matter* **2013**, *419*, 11–18.
39. Nong, Z.-S.; Zhu, J.-C.; Yang, X.-W.; Cao, Y.; Lai, Z.-H.; Liu, Y.; Sun, W. First-principles calculations of the stability and hydrogen storage behavior of C14 Laves phase compound TiCrMn . *Solid State Sci.* **2014**, *32*, 1–7. [[CrossRef](#)]
40. Guo, X.; Wu, E. Thermodynamics of hydrogenation for $\text{Ti}_{1-x}\text{Zr}_x\text{MnCr}$ Laves phase alloys. *J. Alloys Compd.* **2008**, *455*, 191–196.
41. Guo, X.; Wu, E.; Wang, S. Hydrogen storage properties of Laves phase $\text{Ti}_{1-x}\text{Zr}_x(\text{Mn}_{0.5}\text{Cr}_{0.5})_2$ alloys. *Rare Met.* **2006**, *25*, 218–223. [[CrossRef](#)]
42. Li, W.; Wu, E.; Ma, P.; Sun, K.; Chen, D. Hydrogen storage properties of $\text{Ti}_{1-x}\text{Sc}_x\text{MnCr}$ Laves phase alloys. *Int. J. Energy Res.* **2013**, *37*, 686–697. [[CrossRef](#)]
43. Reilly, J.J. Metal Hydride Technology. *Z. Phys. Chem.* **1979**, *117*, 155–184. [[CrossRef](#)]
44. Johnson, J.R.; Reilly, J.J. *The Metal Hydride Research and Development Program at Brookhaven National Laboratory*; Brookhaven National Lab.: Upton, NY, USA, 1978.
45. Johnson, J.R.; Reilly, J.J.; Reidinger, F.; Corliss, L.M.; Hastings, J.M. On the existence of f.c.c. $\text{TiCr}_{1.8}\text{H}_{5.3}$. *J. Less-Common Met.* **1982**, *88*, 107–114. [[CrossRef](#)]
46. Beeri, O.; Cohen, D.; Gavra, Z.; Johnson, J.R.; Mintz, M.H. Thermodynamic characterization and statistical thermodynamics of the $\text{TiCrMn-H}_2(\text{D}_2)$ system. *J. Alloys Compd.* **2000**, *299*, 217–226. [[CrossRef](#)]
47. Beeri, O.; Cohen, D.; Gavra, Z.; Mintz, M.H. Sites occupation and thermodynamic properties of the $\text{TiCr}_{2-x}\text{Mn}_x\text{-H}_2$ ($0 \leq x \leq 1$) system: Statistical thermodynamics analysis. *J. Alloys Compd.* **2003**, *352*, 111–122. [[CrossRef](#)]
48. dos Santos, D.S.; Bououdina, M.; Fruchart, D. Structural and thermodynamic properties of the pseudo-binary $\text{TiCr}_{2-x}\text{V}_x$ compounds with $0.0 \leq x \leq 1.2$. *J. Alloys Compd.* **2002**, *340*, 101–107. [[CrossRef](#)]
49. Ulmer, U.; Dieterich, M.; Pohl, A.; Dittmeyer, R.; Linder, M.; Fichtner, M. Study of the structural, thermodynamic and cyclic effects of vanadium and titanium substitution in laves-phase AB_2 hydrogen storage alloys. *Int. J. Hydrogen Energy* **2017**, *42*, 20103–20110. [[CrossRef](#)]
50. Young, K.; Ouchi, T.; Yang, J.; Fetcenko, M.A. Studies of off-stoichiometric AB_2 metal hydride alloy: Part 1. Structural characteristics. *Int. J. Hydrogen Energy* **2011**, *36*, 11137–11145. [[CrossRef](#)]
51. Young, K.; Nei, J.; Huang, B.; Fetcenko, M.A. Studies of off-stoichiometric AB_2 metal hydride alloy: Part 2. Hydrogen storage and electrochemical properties. *Int. J. Hydrogen Energy* **2011**, *36*, 11146–11154. [[CrossRef](#)]
52. Lee, S.-M.; Lee, H.; Kim, J.-H.; Lee, P.S.; Lee, J.-Y. A study on the development of hypo-stoichiometric Zr-based hydrogen storage alloys with ultra-high capacity for anode material of Ni/MH secondary battery. *J. Alloys Compd.* **2000**, *308*, 259–268. [[CrossRef](#)]
53. Lee, S.-M.; Kim, S.-H.; Jeon, S.-W.; Lee, J.-Y. Study on the Electrode Characteristics of Hypostoichiometric Zr-Ti-V-Mn-Ni Hydrogen Storage Alloys. *J. Electrochem. Soc.* **2000**, *147*, 4464–4469. [[CrossRef](#)]
54. Xu, Y.; Wang, G.; Chen, C.; Wang, Q.; Wang, X. The structure and electrode properties of non-stoichiometric $\text{A}_{1.2}\text{B}_2\text{A}_{1.2}\text{B}_2$ type C14 Laves alloy and the effect of surface modification. *Int. J. Hydrogen Energy* **2007**, *32*, 1050–1058. [[CrossRef](#)]
55. Marinin, V.S.; Umerenkova, K.R.; Volovchuk, O.V. Hydrogen sorption properties of hexagonal laves phase $\text{TiMn}_{1.5}$ intermetallic compound. *Int. J. Hydrogen Energy* **2011**, *36*, 1359–1363. [[CrossRef](#)]
56. Park, J.-G.; Jang, H.-Y.; Han, S.-C.; Lee, P.S.; Lee, J.-Y. The thermodynamic properties of Ti–Zr–Cr–Mn Laves phase alloys. *J. Alloys Compd.* **2001**, *325*, 293–298. [[CrossRef](#)]
57. Pourpoint, T.L.; Velagapudi, V.; Mudawar, I.; Zheng, Y.; Fisher, T.S. Active cooling of a metal hydride system for hydrogen storage. *Int. J. Heat Mass Transfer* **2010**, *53*, 1326–1332. [[CrossRef](#)]

58. Cao, Z.; Ouyang, L.; Wang, H.; Liu, J.; Sun, D.; Zhang, Q.; Zhu, M. Advanced high-pressure metal hydride fabricated via Ti–Cr–Mn alloys for hybrid tank. *Int. J. Hydrogen Energy* **2015**, *40*, 2717–2728. [[CrossRef](#)]
59. Cao, Z.; Ouyang, L.; Wang, H.; Liu, J.; Sun, L.; Zhu, M. Composition design of Ti–Cr–Mn–Fe alloys for hybrid high-pressure metal hydride tanks. *J. Alloys Compd.* **2015**, *639*, 452–457. [[CrossRef](#)]
60. Chen, Z.; Xiao, X.; Chen, L.; Fan, X.; Liu, L.; Li, S.; Ge, H.; Wang, Q. Development of Ti–Cr–Mn–Fe based alloys with high hydrogen desorption pressures for hybrid hydrogen storage vessel application. *Int. J. Hydrogen Energy* **2013**, *38*, 12803–12810. [[CrossRef](#)]
61. Chen, Z.; Xiao, X.; Chen, L.; Fan, X.; Liu, L.; Li, S.; Ge, H.; Wang, Q. Influence of Ti super-stoichiometry on the hydrogen storage properties of $Ti_{1+x}Cr_{1.2}Mn_{0.2}Fe_{0.6}$ ($x = 0-0.1$) alloys for hybrid hydrogen storage application. *J. Alloys Compd.* **2014**, *585*, 307–311. [[CrossRef](#)]
62. Liu, L.; Chen, L.; Xiao, X.; Xu, C.; Sun, J.; Li, S.; Ge, H.; Jiang, L. Influence of annealing treatment on the microstructure and hydrogen storage performance of $Ti_{1.02}Cr_{1.1}Mn_{0.3}Fe_{0.6}$ alloy for hybrid hydrogen storage application. *J. Alloys Compd.* **2015**, *636*, 117–123. [[CrossRef](#)]
63. Yao, Z.; Liu, L.; Xiao, X.; Wang, C.; Jiang, L.; Chen, L. Effect of Rare Earth Doping on the Hydrogen Storage Performance of $Ti_{1.02}Cr_{1.1}Mn_{0.3}Fe_{0.6}$ Alloy for Hybrid Hydrogen Storage Application. *J. Alloys Compd.* **2018**, *731*, 524–530. [[CrossRef](#)]
64. Li, J.; Xu, L.; Jiang, X.; Li, X. Study on the hydrogen storage property of $(TiZr_{0.1})_xCr_{1.7-y}Fe_yMn_{0.3}$ ($1.05 < x < 1.2$, $0.2 < y < 0.6$) alloys. *Prog. Nat. Sci. Mater. Int.* **2018**, *28*, 470–477.
65. Li, J.; Jiang, X.; Li, G.; Li, X. Development of $Ti_{1.02}Cr_{2-x-y}Fe_xMn_y$ ($0.6 \leq x \leq 0.75$, $y = 0.25, 0.3$) alloys for high hydrogen pressure metal hydride system. *Int. J. Hydrogen Energy* **2019**, *44*, 15087–15099. [[CrossRef](#)]
66. Li, J.; Jiang, X.; Li, Z.; Jiang, L.; Li, X. High-pressure hydrogen storage properties of $Ti_xCr_{1-y}Fe_yMn_{1.0}$ alloys. *Int. J. Energy Res.* **2019**, *43*, 5759–5774. [[CrossRef](#)]
67. Puzskiel, J.; Bellosta von Colbe, J.M.; Jepsen, J.; Mitrokhin, S.V.; Movlaev, E.; Verbetsky, V.; Klassen, T. Designing an AB_2 -Type Alloy (TiZr–CrMnMo) for the Hybrid Hydrogen Storage Concept. *Energies* **2020**, *13*, 2751. [[CrossRef](#)]
68. Granovsky, M.S.; Arias, D. Intermetallic phases in the iron-rich region of the ZrFe phase diagram. *J. Nucl. Mater.* **1996**, *229*, 29–35. [[CrossRef](#)]
69. Zotov, T.; Movlaev, E.; Mitrokhin, S.; Verbetsky, V. Interaction in $(Ti,Sc)Fe_2-H_2$ and $(Zr,Sc)Fe_2-H_2$ systems. *J. Alloys Compd.* **2008**, *459*, 220–224. [[CrossRef](#)]
70. Filipek, S.M.; Jacob, I.; Paul-Boncour, V.; Percheron-Guegan, A.; Marchuk, I.; Mogilyanski, D.; Pielaszek, J. ChemInform Abstract: Investigation of ZrFe₂ and ZrCo₂ under Very High Pressure of Gaseous Hydrogen and Deuterium. *ChemInform* **2002**, *33*. [[CrossRef](#)]
71. Paul-Boncour, V.; Bourée-Vignerot, F.; Filipek, S.M.; Marchuk, I.; Jacob, I.; Percheron-Guégan, A. Neutron Diffraction Study of ZrM_2D_x Deuterides ($M = Fe, Co$). *J. Alloys Compd.* **2003**, *356–357*, 69–72. [[CrossRef](#)]
72. Koultoukis, E.D.; Makridis, S.S.; Pavlidou, E.; de Rango, P.; Stubos, A.K. Investigation of ZrFe₂-type materials for metal hydride hydrogen compressor systems by substituting Fe with Cr or V. *Int. J. Hydrogen Energy* **2014**, *39*, 21380–21385. [[CrossRef](#)]
73. Banerjee, S.; Kumar, A.; Pillai, C. Improvement on the hydrogen storage properties of ZrFe₂ Laves phase alloy by vanadium substitution. *Intermetallics* **2014**, *51*, 30–36. [[CrossRef](#)]
74. Jain, A.; Jain, R.K.; Agarwal, S.; Sharma, R.K.; Kulshrestha, S.K.; Jain, I.P. Structural and Mössbauer spectroscopic study of cubic phase $ZrFe_{2-x}Mn_x$ hydrogen storage alloy. *J. Alloys Compd.* **2008**, *454*, 31–37. [[CrossRef](#)]
75. Sivov, R.B.; Zotov, T.A.; Verbetsky, V.N.; Filimonov, D.S.; Pokholok, K.V. Synthesis, Properties and Mössbauer Study of $ZrFe_{2-x}Ni_x$ Hydrides ($x = 0.2-0.8$). *J. Alloys Compd.* **2011**, *509*, S763–S769. [[CrossRef](#)]
76. Sivov, R.B.; Somenkov, V.A.; Glazkov, V.P.; Verbetsky, V.N. Crystal structure of the $ZrFe_{1.8}Ni_{0.2}D_{3.4}$ and $ZrFe_{1.2}Ni_{0.8}D_{3.6}$ deuterides. *Inorg. Mater.* **2012**, *48*, 792–795. [[CrossRef](#)]
77. Yartys, V.A.; Denys, R.V.; Webb, C.J.; Mæhlen, J.P.; Gray, E.M.; Blach, T.; Isnard, O.; Barnsley, L.C. High pressure in situ diffraction studies of metal–hydrogen systems. *J. Alloys Compd.* **2011**, *509*, S817–S822. [[CrossRef](#)]
78. Sivov, R.B.; Zotov, T.A.; Verbetsky, V.N. Interaction of ZrFe₂ doped with Ti and Al with hydrogen. *Inorg. Mater.* **2010**, *46*, 372–376. [[CrossRef](#)]
79. Mendelsohn, M.H.; Gruen, D.M. Intermetallic compounds as bulk getters. *J. Less-Common Met.* **1980**, *74*, 449–453. [[CrossRef](#)]
80. Zhang, T.B.; Wang, X.F.; Hu, R.; Li, J.S.; Yang, X.W.; Xue, X.Y.; Fu, H.Z. Hydrogen absorption properties of $Zr(V_{1-x}Fe_x)_2$ intermetallic compounds. *Int. J. Hydrogen Energy* **2012**, *37*, 2328–2335. [[CrossRef](#)]
81. Yadav, T.P.; Shahi, R.R.; Srivastava, O.N. Synthesis, characterization and hydrogen storage behaviour of AB_2 ($ZrFe_2$, $Zr(Fe_{0.75}V_{0.25})_2$, $Zr(Fe_{0.5}V_{0.5})_2$) type materials. *Int. J. Hydrogen Energy* **2012**, *37*, 3689–3696. [[CrossRef](#)]
82. Kanematsu, K. Magnetic Moment in Laves Phase Compound. II. $Zr(Fe_{1-x}Mn_x)_2$ and $Zr(Fe_{1-x}Co_x)_2$. *J. Phys. Soc. Jpn.* **1971**, *31*, 1355–1360. [[CrossRef](#)]
83. Fujii, H.; Sinha, V.K.; Pourarian, F.; Wallace, W.E. Effect of hydrogen absorption on the magnetic properties of $ZrMn_{2-x}Fe_x$ ternaries with a C14 structure. *J. Less-Common Met.* **1982**, *85*, 43–54. [[CrossRef](#)]
84. Jain, A.; Jain, R.K.; Agarwal, S.; Ganesan, V.; Lalla, N.P.; Phase, D.M.; Jain, I.P. Synthesis, characterization and hydrogenation of $ZrFe_{2-x}Ni_x$ ($x = 0.2, 0.4, 0.6, 0.8$) alloys. *Int. J. Hydrogen Energy* **2007**, *32*, 3965–3971. [[CrossRef](#)]
85. Hirose, S.; Pourarian, F.; Sinha, V.K.; Wallace, W.E. Magnetic properties of $Zr(Cr_{1-x}Co_x)_2$ alloys and their hydrides. *J. Magn. Mater.* **1983**, *38*, 159–164. [[CrossRef](#)]

86. Bereznitsky, M.; Jacob, I.; Bloch, J.; Mintz, M.H. Thermodynamic and structural aspects of hydrogen absorption in the Zr(Al_xFe_{1-x})₂ system. *J. Alloys Compd.* **2003**, *351*, 180–183. [[CrossRef](#)]
87. Coaquira, J.; Rechenberg, H.R.; Mestnik Filho, J. Magnetic properties of Zr(Cr_{1-x}Fe_x)₂ alloys and their hydrides. *J. Magn. Magn. Mater.* **1999**, *196–197*, 677–679. [[CrossRef](#)]
88. Coaquira, J.; Rechenberg, H.R.; Mestnik Filho, J. Structural and Mössbauer spectroscopic study of hexagonal Laves-phase Zr(Fe_xCr_{1-x})₂ alloys and their hydrides. *J. Alloys Compd.* **1999**, *288*, 42–49. [[CrossRef](#)]
89. Yu, G.Y.; Wallace, W.E. The effect of hyperstoichiometric iron on the hydrogen storage properties of ZrMnFe ternary. *J. Solid State Chem.* **1986**, *65*, 356–362. [[CrossRef](#)]
90. Sinha, V.; Pourarian, F.; Wallace, W. Hydrogenation characteristics of Zr_{1-x}Ti_xMnFe alloys. *J. Less-Common Met.* **1982**, *87*, 283–296. [[CrossRef](#)]
91. Zotov, R.S.T.; Mitrokhin, E.; Movlaev, E.A.; Verbetsky, V. *Carbon Nanomaterials in Clean Energy Hydrogen Systems*; Springer: Dordrecht, The Netherlands, 2008; pp. 699–704.
92. Zotov, T.A.; Sivov, R.B.; Movlaev, E.A.; Mitrokhin, S.V.; Verbetsky, V.N. IMC hydrides with high hydrogen dissociation pressure. *J. Alloys Compd.* **2011**, *509*, S839–S843. [[CrossRef](#)]
93. Davidson, D.J.; Srivastava, O.N. Studies on the hydrogen absorption/desorption properties of Zr_{1-x}Mm_xFe_{1.4}Cr_{0.6} and Zr_{1-2x}Mm_xTi_xFe_{1.4}Cr_{0.6} (x = 0, 0.05, 0.1 and 0.2) Laves phase alloys. *Int. J. Hydrogen Energy* **2001**, *26*, 219–223. [[CrossRef](#)]
94. Davidson, D.J.; Raman, S.S.; Lototsky, M.V.; Srivastava, O.N. On the computer simulation of the P–C isotherms of ZrFe₂ type hydrogen storage materials. *Int. J. Hydrogen Energy* **2003**, *28*, 1425–1431. [[CrossRef](#)]
95. Sivov, R.B.; Zotov, T.A.; Verbetsky, V.N. Hydrogen sorption properties of ZrFe_x (1.9 ≤ x ≤ 2.5) alloys. *Int. J. Hydrogen Energy* **2011**, *36*, 1355–1358. [[CrossRef](#)]
96. Jiang, L.; Tu, Y.; Tu, H.; Chen, L. Microstructures and hydrogen storage properties of ZrFe_{2.05-x}V_x (x = 0.05–0.20) alloys with high dissociation pressures for hybrid hydrogen storage vessel application. *J. Alloys Compd.* **2015**, *627*, 161–165. [[CrossRef](#)]
97. Cao, Z.; Ouyang, L.; Wang, H.; Liu, J.; Sun, L.; Felderhoff, M.; Zhu, M. Development of Zr single bond Fe single bond V alloys for hybrid hydrogen storage system. *Int. J. Hydrogen Energy* **2016**, *41*, 11242–11253. [[CrossRef](#)]
98. Zhou, C.; Wang, H.; Ouyang, L.Z.; Liu, J.W.; Zhu, M. Achieving high equilibrium pressure and low hysteresis of Zr–Fe based hydrogen storage alloy by Cr/V substitution. *J. Alloys Compd.* **2019**, *806*, 1436–1444. [[CrossRef](#)]
99. Qin, C.; Zhou, C.; Ouyang, L.; Liu, J.; Zhu, M.; Sun, T.; Wang, H. High-pressure hydrogen storage performances of ZrFe₂ based alloys with Mn, Ti, and V addition. *Int. J. Hydrogen Energy* **2020**, *45*, 9836–9844. [[CrossRef](#)]
100. Kandavel, M.; Ramaprabhu, S. The effect of non-stoichiometry on the hydrogen storage properties of Ti-substituted AB₂ alloys. *J. Phys. Condens. Matter* **2003**, *15*, 7501–7517. [[CrossRef](#)]
101. Li, S.L.; Cheng, H.H.; Deng, X.X.; Chen, W.; Chen, D.M.; Yang, K. Investigation of hydrogen absorption/desorption properties of ZrMn_{0.85-x}Fe_{1+x} alloys. *J. Alloys Compd.* **2008**, *460*, 186–190. [[CrossRef](#)]
102. Kandavel, M.; Ramaprabhu, S. Hydriding properties of Ti-substituted non-stoichiometric AB₂ alloys. *J. Alloys Compd.* **2004**, *381*, 140–150. [[CrossRef](#)]
103. Akiba, E.; Iba, H. Hydrogen absorption by Laves phase related BCC solid solution. *Intermetallics* **1998**, *6*, 461–470. [[CrossRef](#)]
104. Yu, X.; Wu, Z.; Xia, B.; Huang, T.; Chen, J.; Wang, Z.; Xu, N. Hydrogen storage in Ti–V-based body-centered-cubic phase alloys. *J. Mater. Res.* **2003**, *18*, 2533–2536. [[CrossRef](#)]
105. Nomura, K.; Akiba, E. H₂ Absorbing-desorbing characterization of the Ti single bond V single bond Fe alloy system. *J. Alloys Compd.* **1995**, *231*, 513–517. [[CrossRef](#)]
106. Yukawa, H.; Teshima, A.; Yamashita, D.; Ito, S.; Yamaguchi, S.; Morinaga, M. Alloying effects on the hydriding properties of vanadium at low hydrogen pressures. *J. Alloys Compd.* **2002**, *337*, 264–268. [[CrossRef](#)]
107. Yoo, J.-H.; Shim, G.; Park, C.-N.; Kim, W.-B.; Cho, S.-W. Influence of Mn or Mn plus Fe on the hydrogen storage properties of the Ti–Cr–V alloy. *Int. J. Hydrogen Energy* **2009**, *34*, 9116–9121. [[CrossRef](#)]
108. Arashima, H.; Takahashi, F.; Ebisawa, T.; Itoh, H.; Kabutomori, T. Correlation between hydrogen absorption properties and homogeneity of Ti–Cr–V alloys. *J. Alloys Compd.* **2003**, *356–357*, 405–408. [[CrossRef](#)]
109. Wu, C.; Yan, Y.; Chen, Y.; Tao, M.; Zheng, X. Effect of rare earth (RE) elements on V-based hydrogen storage alloys. *Int. J. Hydrogen Energy* **2008**, *33*, 93–97. [[CrossRef](#)]
110. Ono, S.; Nomura, K.; Ikeda, Y. The reaction of hydrogen with alloys of vanadium and titanium. *J. Less-Common Met.* **1980**, *72*, 159–165. [[CrossRef](#)]
111. Nowak, B.; Hayashi, S.; Hayamizu, K.; Yamamoto, O. X-ray diffraction and ¹H and ⁵¹V NMR study of the structure of a Ti V H alloy in relation to preparation conditions. *J. Less-Common Met.* **1986**, *123*, 75–84. [[CrossRef](#)]
112. Matsuda, J.; Akiba, E. Lattice defects in V–Ti BCC alloys before and after hydrogenation. *J. Alloys Compd.* **2013**, *581*, 369–372. [[CrossRef](#)]
113. Lynch, J.F.; Reilly, J.J.; Millot, F. The absorption of hydrogen by binary vanadium-chromium alloys. *Solid State Commun.* **1978**, *26*, iv–v. [[CrossRef](#)]
114. Verbetsky, V.N.; Zotov, T.A.; Tatarintsev, A.V.; Movlaev, E.A. Hydrogen sorption properties of V_{1-x}Cr_x (x = 0.1–0.5) alloys. *Inorg. Mater.* **2013**, *49*, 149–152. [[CrossRef](#)]
115. Asano, K.; Hayashi, S.; Nakamura, Y.; Akiba, E. Effect of substitutional Cr on hydrogen diffusion and thermal stability for the BCT monohydride phase of the V–H system studied by ¹H NMR. *J. Alloys Compd.* **2012**, *524*, 63–68. [[CrossRef](#)]

116. Asano, K.; Hayashi, S.; Nakamura, Y.; Akiba, E. Effect of substitutional Mo on diffusion and site occupation of hydrogen in the BCT monohydride phase of V–H system studied by ^1H NMR. *J. Alloys Compd.* **2010**, *507*, 399–404. [[CrossRef](#)]
117. Verbetsky, V.N.; Zotov, T.A.; Movlaev, E.A. Absorption of hydrogen by V–Mo and V–Mo–Ti alloys. *Inorg. Mater. Appl. Res.* **2014**, *5*, 70–74. [[CrossRef](#)]
118. Phung, T.V.B.; Ogawa, H.; Dinh, V.A.; Nguyen, O.H.; Shibutani, Y.; Asano, K.; Nakamura, Y.; Akiba, E. Effects of substitutional Mo and Cr on site occupation and diffusion of hydrogen in the β -phase vanadium hydride by first principles calculations. *Theor. Chem. Acc.* **2019**, *138*, 16. [[CrossRef](#)]
119. Miraglia, S.; de Rango, P.; Rivoirard, S.; Fruchart, D.; Charbonnier, J.; Skryabina, N. Hydrogen sorption properties of compounds based on BCC $\text{Ti}_{1-x}\text{V}_{1-y}\text{Cr}_{1+x+y}$ alloys. *J. Alloys Compd.* **2012**, *536*, 1–6. [[CrossRef](#)]
120. Tamura, T.; Kazumi, T.; Kamegawa, A.; Takamura, H.; Okada, M. Protium absorption properties and protide formations of Ti–Cr–V alloys. *J. Alloys Compd.* **2003**, 356–357, 505–509. [[CrossRef](#)]
121. Itoh, H.; Arashima, H.; Kubo, K.; Kabutomori, T.; Ohnishi, K. Improvement of cyclic durability of BCC structured Ti–Cr–V alloys. *J. Alloys Compd.* **2005**, 404–406, 417–420. [[CrossRef](#)]
122. Lynch, J.F.; Maeland, A.J.; Libowitz, G.G. Lattice Parameter Variation and Thermodynamics of Dihydride Formation in the Vanadium-Rich V–Ti–Fe/ H_2 System. *Z. Phys. Chem.* **1985**, *145*, 51–59. [[CrossRef](#)]
123. Fu, G.; Wang, F.; Wang, J.; Rong, M.H.; Wang, Z.M.; Rao, G.H.; Zhou, H.Y. Microstructure and Hydrogen Storage Properties of Ti–V–Fe Alloys. *Mater. Sci. Forum* **2016**, *847*, 3–7.
124. Guéguen, A.; Joubert, J.-M.; Lacroche, M. Influence of the C14 $\text{Ti}_{35.4}\text{V}_{32.3}\text{Fe}_{32.3}$ Laves phase on the hydrogenation properties of the body-centered cubic compound $\text{Ti}_{24.5}\text{V}_{59.3}\text{Fe}_{16.2}$. *J. Alloys Compd.* **2011**, *509*, 3013–3018. [[CrossRef](#)]
125. Callear, S.K.; Ramirez-Cuesta, A.J.; Kamazawa, K.; Towata, S.; Noritake, T.; Parker, S.F.; Jones, M.O.; Sugiyama, J.; Ishikiriya, M.; David, W.I.F. Understanding composition-property relationships in Ti–Cr–V–Mo alloys for optimisation of hydrogen storage in pressurised tanks. *Phys. Chem. Chem. Phys.* **2014**, *16*, 16563–16572. [[CrossRef](#)] [[PubMed](#)]
126. Basak, S.; Shashikala, K.; Sengupta, P.; Kulshrestha, S.K. Hydrogen absorption properties of Ti–V–Fe alloys: Effect of Cr substitution. *Int. J. Hydrogen Energy* **2007**, *32*, 4973–4977. [[CrossRef](#)]
127. Yan, Y.; Chen, Y.; Liang, H.; Wu, C.; Tao, M.; Mingjing, T. Effect of Al on hydrogen storage properties of $\text{V}_{30}\text{Ti}_{35}\text{Cr}_{25}\text{Fe}_{10}$ alloy. *J. Alloys Compd.* **2006**, *426*, 253–255. [[CrossRef](#)]
128. Kuriwa, T.; Maruyama, T.; Kamegawa, A.; Okada, M. Effects of V content on hydrogen storage properties of V–Ti–Cr alloys with high desorption pressure. *Int. J. Hydrogen Energy* **2010**, *35*, 9082–9087. [[CrossRef](#)]
129. Goshome, K.; Endo, N.; Tetsuhiko, M. Evaluation of a BCC alloy as metal hydride compressor via 100 MPa-class high-pressure hydrogen apparatus. *Int. J. Hydrogen Energy* **2019**, *44*, 10800–10807. [[CrossRef](#)]
130. Selvaraj, S.; Jain, A.; Kumar, S.; Zhang, T.; Isobe, S.; Miyaoka, H.; Kojima, Y.; Ichikawa, T. Study of cyclic performance of V–Ti–Cr alloys employed for hydrogen compressor. *Int. J. Hydrogen Energy* **2018**, *43*, 2881–2889. [[CrossRef](#)]
131. Nonobe, Y. Development of the fuel cell vehicle mirai. *IEEJ Trans. Electr. Electron. Eng.* **2017**, *12*, 5–9. [[CrossRef](#)]
132. Kumar, S.; Jain, A.; Ichikawa, T.; Kojima, Y.; Dey, G.K. Development of vanadium based hydrogen storage material: A review. *Renew. Sustain. Energy Rev.* **2017**, *72*, 791–800. [[CrossRef](#)]
133. Lys, A.; Fadonougbo, J.O.; Faisal, M.; Suh, J.-Y.; Lee, Y.-S.; Shim, J.-H.; Park, J.; Cho, Y.W. Enhancing the Hydrogen Storage Properties of AxBy Intermetallic Compounds by Partial Substitution: A Short Review. *Hydrogen* **2020**, *1*, 38–63. [[CrossRef](#)]
134. Young, K.; Wong, D.F.; Yasuoka, S.; Ishida, J.; Nei, J.; Koch, J. Different failure modes for V-containing and V-free AB_2 metal hydride alloys. *J. Power Sources* **2014**, *251*, 170–177. [[CrossRef](#)]
135. Bibienne, T.; Gosselin, C.; Bobet, J.-L.; Huot, J. Replacement of Vanadium by Ferrovandium in a Ti-Based Body Centred Cubic (BCC) Alloy: Towards a Low-Cost Hydrogen Storage Material. *J. Appl. Sci.* **2018**, *8*, 1151. [[CrossRef](#)]
136. Yan, Y.; Chen, Y.; Wu, C.; Tao, M.; Liang, H. A low-cost BCC alloy prepared from a FeV80 alloy with a high hydrogen storage capacity. *J. Power Sources* **2007**, *164*, 799–802. [[CrossRef](#)]
137. Wu, C.; Zheng, X.; Chen, Y.; Tao, M.; Tong, G.; Zhou, J. Hydrogen storage and cyclic properties of $\text{V60Ti}_{(21.4+x)}\text{Cr}_{(6.6-x)}\text{Fe}_{12}$ ($0 \leq x \leq 3$) alloys. *Int. J. Hydrogen Energy* **2010**, *35*, 8130–8135. [[CrossRef](#)]
138. Mao, Y.; Yang, S.; Wu, C.; Luo, L.; Chen, Y. Preparation of $(\text{FeV80})_{48}\text{Ti}_{26+x}\text{Cr}_{26}$ ($x=0-4$) alloys by the hydride sintering method and their hydrogen storage performance. *J. Alloys Compd.* **2017**, *705*, 533–538. [[CrossRef](#)]
139. Yang, S.; Yang, F.; Wu, C.; Chen, Y.; Mao, Y.; Luo, L. Hydrogen storage and cyclic properties of $(\text{VFe})_{60}(\text{TiCrCo})_{40-x}\text{Zr}_x$ ($0 \leq x \leq 2$) alloys. *J. Alloys Compd.* **2016**, *663*, 460–465. [[CrossRef](#)]
140. Ley, M.B.; Jepsen, L.H.; Lee, Y.-S.; Cho, Y.W.; Bellosta von Colbe, J.M.; Dornheim, M.; Rokni, M.; Jensen, J.O.; Sloth, M.; Filinchuk, Y.; et al. Complex hydrides for hydrogen storage—New perspectives. *Mater. Today* **2014**, *17*, 122–128. [[CrossRef](#)]
141. Bogdanović, B.; Schwickardi, M. Ti-doped alkali metal aluminium hydrides as potential novel reversible hydrogen storage materials. *J. Alloys Compd.* **1997**, 253–254, 1–9. [[CrossRef](#)]
142. Suárez-Alcántara, K.; Tena-García, J.R.; Guerrero-Ortiz, R. Alanates, a Comprehensive Review. *Materials* **2019**, *12*, 2724. [[CrossRef](#)]
143. Monnier, G. Sur les hydrures complexes des métaux de transition. *Bull. Soc. Chim. Fr.* **1955**, 1138.
144. Kost, M.E.; Golovanova, A.I. Reaction of lithium tetrahydroaluminate with transition metal halides. *Izv. Akad. Nauk SSSR Neorg. Mater.* **1978**, *14*, 1732–1734.
145. Neumaier, H.; Büchel, D.; Ziegelmaier, G. Über die Umsetzung von Eisen(III)-chlorid mit Lithiumalanat bei tiefen Temperaturen. *Z. Anorg. Allg. Chem.* **1966**, *345*, 46–52. [[CrossRef](#)]

146. Kost, M.E.; Golovanova, A.I. Interaction of Titanium and Iron Halides with Lithium Alanate in Diethylether. *Izv. Akad. Nauk SSSR Ser. Khim.* **1975**, *5*, 991–994.
147. Kuznetsov, N.T.; Mal'tseva, N.N.; Golovanova, A.I. Synthesis and properties of etherate of scandium alumohydride. *Russ. J. Inorg. Chem.* **1985**, *30*, 1604–1606.
148. Monnier, G. Les hydrures métalliques et l'éther anhydre. *Ann. Chim.* **1957**, *13*, 33.
149. Weidenthaler, C.; Pommerin, A.; Felderhoff, M.; Sun, W.; Wolverson, C.; Bogdanović, B.; Schüth, F. Complex rare-earth aluminum hydrides: Mechanochemical preparation, crystal structure and potential for hydrogen storage. *J. Am. Chem. Soc.* **2009**, *131*, 16735–16743. [[CrossRef](#)] [[PubMed](#)]
150. Wiberg, E.; Henle, W. Notizen: Zur Kenntnis eines Quecksilberwasserstoffs HgH_2 . *Z. Naturforsch. B* **1951**, *6*, 461–462. [[CrossRef](#)]
151. Wiberg, E.; Neumaier, H. Zur Frage der Existenz eines Gold (III)-Hydrids AuH_3 . *Inorg. Nucl. Chem. Lett.* **1965**, *1*, 35–37. [[CrossRef](#)]
152. Wiberg, E.; Henle, W. Notizen: Zur Kenntnis eines Cadmiumwasserstoffs CdH_2 . *Z. Naturforsch. B* **1951**, *6*, 461. [[CrossRef](#)]
153. Neumaier, H. *Dissertation*; Ludwig-Maximilians-Universität: München, Germany, 1961.
154. Habermann, F.; Burkmann, K.; Hansel, B.; Störr, B.; Schimpf, C.; Seidel, J.; Bertau, M.; Mertens, F. Hydrogen absorption and desorption in the V-Al-H system. *Dalton Trans.* **2023**, *52*, 4880–4890. [[CrossRef](#)]
155. Wiberg, E.; Usón, R. Zur Kenntnis eines Zinkwasserstoffs ZnH_2 . *Z. Naturforsch. B* **1951**, *6*, 393–394. [[CrossRef](#)]
156. Golovanova, I.; Kost, M.E.; Mikheeva, V.I. Interaction of tantalum halides with lithium aluminum hydride in ether. *Bull. Acad. Sci. USSR Div. Chem. Sci. Engl. Transl.* **1973**, *22*, 1410–1413. [[CrossRef](#)]
157. Jander, G.; Krafczyk, K. Ionenreaktionen in absolutem Diäthyläther als Lösungsmittel. II. Konduktometrische Titrationsen von einigen organischen und anorganischen Verbindungstypen mit Lithiumaluminiumhydrid in absolutem Diäthyläther. *Z. Anorg. Allg. Chem.* **1956**, *283*, 217–229. [[CrossRef](#)]
158. Wiberg, E.; Henle, W. Zur Kenntnis eines Silber-aluminium-wasserstoffs $AgAlH_4$. *Z. Naturforsch. B* **1952**, *7*, 250–251. [[CrossRef](#)]
159. Reid, W.E.; Bish, J.M.; Brenner, A. Electrodeposition of Metals from Organic Solutions. *J. Electrochem. Soc.* **1957**, *104*, 21–29. [[CrossRef](#)]
160. Soloveichik, G.L.; Bulychev, B.M. Bimetallic Transition Metal Hydride Complexes. *Russ. Chem. Rev.* **1983**, *52*, 43–60. [[CrossRef](#)]
161. Ashby, E.C.; Kovar, R.A. Reaction of Lithium Aluminum Hydride with Copper(I) and Mercury(II) Salts. Nature of the Reactive Species in the Conjugate Reducing Agent $LiAlH_4$ -CuI. *Inorg. Chem.* **1977**, *16*, 1437–1440. [[CrossRef](#)]
162. Ashby, E.C.; Prasad, H.S. Reactions of Aluminum Hydride with Group 1b, 2a, and 2b Metal Halides. *Inorg. Chem.* **1975**, *14*, 1608–1614. [[CrossRef](#)]
163. Pommerin, A.; Wosylus, A.; Felderhoff, M.; Schüth, F.; Weidenthaler, C. Synthesis, crystal structures, and hydrogen-storage properties of $Eu(AlH_4)_2$ and $Sr(AlH_4)_2$ and of their decomposition intermediates, $EuAlH_5$ and $SrAlH_5$. *Inorg. Chem.* **2012**, *51*, 4143–4150. [[CrossRef](#)] [[PubMed](#)]
164. Schaeffer, G.W.; Roscoe, J.S.; Stewart, A.C. The Reduction of Iron(III) Chloride with Lithium Aluminohydride and Lithium Borohydride: Iron(II) Borohydride. *J. Am. Chem. Soc.* **1956**, *78*, 729–733. [[CrossRef](#)]
165. Kost, M.E.; Golovanova, A.I. Reaction of niobium pentachloride with lithium tetrahydroaluminate in diethyl ether. *Zh. Neorg. Khim.* **1977**, *22*, 977–979.
166. Wiberg, E.; Neumaier, H. Zur Kenntnis von Doppel- und Tripelhydriden der Übergangsmetalle. I. Über die Umsetzung von Niob(V)-chlorid mit Lithiumalanat. *Z. Anorg. Allg. Chem.* **1965**, *340*, 189–200. [[CrossRef](#)]
167. Wiberg, E.; Usón, R. Zur Kenntnis eines Titan-aluminium-wasserstoffs $Ti(AlH_4)_4$. *Z. Naturforsch. B* **1951**, *6*, 392–393. [[CrossRef](#)]
168. Kost, M.E.; Golovanova, A.I. Production of yttrium alanate. *Zh. Neorg. Khim.* **1977**, *22*, 832–833.
169. Cao, Z.; Ouyang, L.; Wang, H.; Liu, J.; Felderhoff, M.; Zhu, M. Reversible hydrogen storage in yttrium aluminum hydride. *J. Mater. Chem. A* **2017**, *5*, 6042–6046. [[CrossRef](#)]
170. Cao, Z.; Felderhoff, M. Mechanochemical synthesis and dehydrogenation properties of $Yb(AlH_4)_3$. *Int. J. Hydrogen Energy* **2021**, *46*, 26437–26444. [[CrossRef](#)]
171. Li, H.-W.; Yan, Y.; Orimo, S.-I.; Züttel, A.; Jensen, C.M. Recent Progress in Metal Borohydrides for Hydrogen Storage. *Energies* **2011**, *4*, 185–214. [[CrossRef](#)]
172. Vajo, J.J.; Mertens, F.; Ahn, C.C.; Bowman, R.C.; Fultz, B. Altering Hydrogen Storage Properties by Hydride Destabilization through Alloy Formation: LiH and MgH_2 Destabilized with Si. *J. Phys. Chem. B* **2004**, *108*, 13977–13983. [[CrossRef](#)]
173. Vajo, J.J.; Skeith, S.L.; Mertens, F. Reversible storage of hydrogen in destabilized $LiBH_4$. *J. Phys. Chem. B* **2005**, *109*, 3719–3722. [[CrossRef](#)]
174. Suárez-Alcántara, K.; Tena García, J.R. Metal Borohydrides beyond Groups I and II: A Review. *Materials* **2021**, *14*, 2561–2616. [[CrossRef](#)]
175. Nöth, H.; Seitz, M. Preparation and Characterization of Chromium(II) Tetrahydroborate–Tetrahydrofuran (1/2). *J. Chem. Soc. Chem. Commun.* **1976**, *24*, 1004a. [[CrossRef](#)]
176. Lobkovskii, B.; Kravchenko, S.E.; Semenenko, K.N. X-Ray Structure Study of Crystals of the Tetrahydrofuranate of Scandium Borohydride. *J. Struct. Chem.* **1977**, *18*, 312–314. [[CrossRef](#)]
177. Morris, J.H.; Smith, W.E. Synthesis and Characterisation of a Tetrahydrofuran Derivative of Scandium Tetrahydroborate. *J. Chem. Soc. D* **1970**, *4*, 245a. [[CrossRef](#)]
178. Nöth, H.; Winter, L.P. Metallboranate und Boranato-metallate. V. Solvate des Cadmiumboranats und Boranato-cadmiate. *Z. Anorg. Allg. Chem.* **1972**, *389*, 225–234. [[CrossRef](#)]

179. Nakamori, Y.; Li, H.; Miwa, K.; Towata, S.; Orimo, S.-I. Syntheses and Hydrogen Desorption Properties of Metal-Borohydrides $M(\text{BH}_4)_n$ ($M = \text{Mg, Sc, Zr, Ti, and Zn}$; $n = 2-4$) as Advanced Hydrogen Storage Materials. *Mater. Trans.* **2006**, *47*, 1898–1901. [[CrossRef](#)]
180. Nakamori, Y.; Li, H.-W.; Kikuchi, K.; Aoki, M.; Miwa, K.; Towata, S.; Orimo, S. Thermodynamical stabilities of metal-borohydrides. *J. Alloys Compd.* **2007**, *446–447*, 296–300. [[CrossRef](#)]
181. Nakamori, Y.; Li, H.-W.; Matsuo, M.; Miwa, K.; Towata, S.; Orimo, S. Development of metal borohydrides for hydrogen storage. *J. Phys. Chem. Solids* **2008**, *69*, 2292–2296. [[CrossRef](#)]
182. Jeon, E.; Cho, Y. Mechanochemical synthesis and thermal decomposition of zinc borohydride. *J. Alloys Compd.* **2006**, *422*, 273–275. [[CrossRef](#)]
183. Song, M.Y.; Kwak, Y.J.; Kwon, S.N.; Lee, S.H.; Park, I.W. Synthesis of $\text{Zn}(\text{BH}_4)_2$ and Gas Absorption and Release Characteristics of $\text{Zn}(\text{BH}_4)_2$, Ni, or Ti-Added MgH_2 -Based Alloys. *Korean J. Met. Mater.* **2015**, *53*, 500–505. [[CrossRef](#)]
184. Srinivasan, S.; Escobar, D.; Jurczyk, M.; Goswami, Y.; Stefanakos, E. Nanocatalyst doping of $\text{Zn}(\text{BH}_4)_2$ for on-board hydrogen storage. *J. Alloys Compd.* **2008**, *462*, 294–302. [[CrossRef](#)]
185. Ravnsbaek, D.; Filinchuk, Y.; Cerenius, Y.; Jakobsen, H.J.; Besenbacher, F.; Skibsted, J.; Jensen, T.R. A series of mixed-metal borohydrides. *Angew. Chem. Int. Ed.* **2009**, *48*, 6659–6663. [[CrossRef](#)]
186. Gu, Q.; Gao, L.; Guo, Y.; Tan, Y.; Tang, Z.; Wallwork, K.S.; Zhang, F.; Yu, X. Structure and decomposition of zinc borohydride ammonia adduct: Towards a pure hydrogen release. *Energy Environ. Sci.* **2012**, *5*, 7590–7600. [[CrossRef](#)]
187. Mikheeva, V.I.; Mal'tseva, N.N.; Alekseeva, L.S. Reaction of Potassium Tetrahydroborate with Zinc Chloride in Diethyl Ether at 0 °C. *Russ. J. Inorg. Chem.* **1968**, *13*, 682–685.
188. Yang, C.-H.; Tsai, W.-T.; Chang, J.-K. Hydrogen desorption behavior of vanadium borohydride synthesized by modified mechanochemical process. *Int. J. Hydrogen Energy* **2011**, *36*, 4993–4999. [[CrossRef](#)]
189. Korablov, D.; Ravnsbæk, D.B.; Ban, V.; Filinchuk, Y.; Besenbacher, F.; Jensen, T.R. Investigation of $\text{MBH}_4\text{-VCl}_2$, $M = \text{Li, Na or K}$. *Int. J. Hydrogen Energy* **2013**, *38*, 8376–8383. [[CrossRef](#)]
190. Park, K.; Lee, H.-S.; Remhof, A.; Lee, Y.-S.; Yan, Y.; Kim, M.-Y.; Kim, S.J.; Züttel, A.; Cho, Y.W. Thermal properties of $\text{Y}(\text{BH}_4)_3$ synthesized via two different methods. *Int. J. Hydrogen Energy* **2013**, *38*, 9263–9270. [[CrossRef](#)]
191. Nöth, H. Anorganische Reaktionen der Alkaliboranate. *Angew. Chem.* **1961**, *73*, 371–383. [[CrossRef](#)]
192. Wiberg, E.; Henle, W. Notizen: Zur Kenntnis eines Silber-bor-wasserstoffs AgBH_4 . *Z. Naturforsch. B* **1952**, *7*, 575–576. [[CrossRef](#)]
193. Rice, G.W.; Woodin, R.L. Zirconium Borohydride as a Zirconium Boride Precursor. *J. Am. Chem. Soc.* **1988**, *71*, C181–C183. [[CrossRef](#)]
194. Richter, B.; Grinderslev, J.B.; Møller, K.T.; Paskevicius, M.; Jensen, T.R. From Metal Hydrides to Metal Borohydrides. *Inorg. Chem.* **2018**, *57*, 10768–10780. [[CrossRef](#)]
195. Grinderslev, J.B.; Møller, K.T.; Bremholm, M.; Jensen, T.R. Trends in Synthesis, Crystal Structure, and Thermal and Magnetic Properties of Rare-Earth Metal Borohydrides. *Inorg. Chem.* **2019**, *58*, 5503–5517. [[CrossRef](#)]
196. Bannenberg, L.J.; Heere, M.; Benzidi, H.; Montero, J.; Dematteis, E.M.; Suwarno, S.; Jaroń, T.; Winny, M.; Orłowski, P.A.; Wegner, W.; et al. Metal (boro-) hydrides for high energy density storage and relevant emerging technologies. *Int. J. Hydrogen Energy* **2020**, *45*, 33687–33730. [[CrossRef](#)]
197. Sharma, M.; Didelot, E.; Spyratou, A.; Lawson Daku, L.M.; Černý, R.; Hagemann, H. Halide Free $\text{M}(\text{BH}_4)_2$ ($M = \text{Sr, Ba, and Eu}$) Synthesis, Structure, and Decomposition. *Inorg. Chem.* **2016**, *55*, 7090–7097. [[CrossRef](#)]
198. Remhof, A.; Borgschulte, A.; Friedrichs, O.; Mauron, P.; Yan, Y.; Züttel, A. Solvent-free synthesis and decomposition of $\text{Y}(\text{BH}_4)_3$. *Scr. Mater.* **2012**, *66*, 280–283. [[CrossRef](#)]
199. Roedern, E.; Lee, Y.-S.; Ley, M.B.; Park, K.; Cho, Y.W.; Skibsted, J.; Jensen, T.R. Solid state synthesis, structural characterization and ionic conductivity of bimetallic alkali-metal yttrium borohydrides $\text{MY}(\text{BH}_4)_4$ ($M = \text{Li and Na}$). *J. Mater. Chem. A* **2016**, *4*, 8793–8802. [[CrossRef](#)]
200. Ley, M.B.; Paskevicius, M.; Schouwink, P.; Richter, B.; Sheppard, D.A.; Buckley, C.E.; Jensen, T.R. Novel solvates $\text{M}(\text{BH}_4)_3\text{S}(\text{CH}_3)_2$ and properties of halide-free $\text{M}(\text{BH}_4)_3$ ($M = \text{Y or Gd}$). *Dalton Trans.* **2014**, *43*, 13333–13342. [[CrossRef](#)]
201. Richter, B.; Ravnsbæk, D.B.; Tumanov, N.; Filinchuk, Y.; Jensen, T.R. Manganese borohydride; synthesis and characterization. *Dalton Trans.* **2015**, *44*, 3988–3996. [[CrossRef](#)] [[PubMed](#)]
202. ISO 11357-1:2016; Kunststoffe—Dynamische Differenz-Thermoanalyse (DSC)—Teil 1: Allgemeine Grundlagen; 83.080.01; Deutsches Institut für Normung e. V.: Berlin, Germany; Beuth Verlag GmbH: Berlin, Germany, 2017.
203. Ley, M.B.; Jørgensen, M.; Černý, R.; Filinchuk, Y.; Jensen, T.R. From $\text{M}(\text{BH}_4)_3$ ($M = \text{La, Ce}$) Borohydride Frameworks to Controllable Synthesis of Porous Hydrides and Ion Conductors. *Inorg. Chem.* **2016**, *55*, 9748–9756. [[CrossRef](#)] [[PubMed](#)]
204. Gennari, F.C.; Esquivel, M.R. Synthesis and dehydriding process of crystalline $\text{Ce}(\text{BH}_4)_3$. *J. Alloys Compd.* **2009**, *485*, L47–L51. [[CrossRef](#)]
205. Zhang, B.J.; Liu, B.H.; Li, Z.P. Destabilization of LiBH_4 by $(\text{Ce, La})(\text{Cl, F})_3$ for hydrogen storage. *J. Alloys Compd.* **2011**, *509*, 751–757. [[CrossRef](#)]
206. Aubry, J.; Monnier, G. Sur les borohydrures de manganèse, de fer, de cobalt et de nickel. *Bull. Soc. Chim. Fr.* **1955**, 482.
207. Stewart, C.; Schaeffer, G.W. The Reaction of Cobalt(II) Bromide with Lithium Borohydride and Lithium Aluminohydride. *J. Inorg. Nucl. Chem.* **1956**, *3*, 194–197. [[CrossRef](#)]
208. Wiberg, E. Neuere Ergebnisse der präparativen Hydrid-Forschung. *Angew. Chem.* **1953**, *65*, 16–33. [[CrossRef](#)]

209. Klingen, T.J. The Reaction of Copper(II) Chloride with Lithium Borohydride. *Inorg. Chem.* **1964**, *3*, 1058–1059. [[CrossRef](#)]
210. Wiberg, E.; Henle, W. Notizen: Zur Kenntnis eines Cadmium-bor-wasserstoffs $\text{Cd}(\text{BH}_4)_2$ und eines Kupfer-bor-wasserstoffs CuBH_4 . *Z. Naturforsch. B* **1952**, *7*, 582. [[CrossRef](#)]
211. Mal'tseva, N.N. A Study of Various Reactions of Copper Hydride. *Russ. J. Inorg. Chem.* **1997**, *12*, 1338–1341.
212. Blanchard, D.; Zatti, M.; Vegge, T. Analysis of the decomposition gases from α and β - $\text{Cd}(\text{BH}_4)_2$ synthesized by temperature controlled mechanical milling. *J. Alloys Compd.* **2013**, *547*, 76–80. [[CrossRef](#)]
213. Ravnsbæk, D.B.; Sørensen, L.H.; Filinchuk, Y.; Besenbacher, F.; Jensen, T.R. Screening of metal borohydrides by mechanochemistry and diffraction. *Angew. Chem. Int. Ed.* **2012**, *51*, 3582–3586. [[CrossRef](#)] [[PubMed](#)]
214. Humphries, T.D.; Ley, M.B.; Frommen, C.; Munroe, K.T.; Jensen, T.R.; Hauback, B.C. Crystal structure and in situ decomposition of $\text{Eu}(\text{BH}_4)_2$ and $\text{Sm}(\text{BH}_4)_2$. *J. Mater. Chem. A* **2015**, *3*, 691–698. [[CrossRef](#)]
215. Wegner, W.; Jaroń, T.; Grochala, W. Preparation of a series of lanthanide borohydrides and their thermal decomposition to refractory lanthanide borides. *J. Alloys Compd.* **2018**, *744*, 57–63. [[CrossRef](#)]
216. Olsen, J.E.; Frommen, C.; Jensen, T.R.; Riktor, M.D.; Sørby, M.H.; Hauback, B.C. Structure and thermal properties of composites with RE-borohydrides (RE = La, Ce, Pr, Nd, Sm, Eu, Gd, Tb, Er, Yb or Lu) and LiBH_4 . *RSC Adv.* **2014**, *4*, 1570–1582. [[CrossRef](#)]
217. Heere, M.; Payandeh GharibDoust, S.H.; Frommen, C.; Humphries, T.D.; Ley, M.B.; Sørby, M.H.; Jensen, T.R.; Hauback, B.C. The influence of LiH on the rehydrogenation behavior of halide free rare earth (RE) borohydrides (RE = Pr, Er). *Phys. Chem. Chem. Phys.* **2016**, *18*, 24387–24395. [[CrossRef](#)] [[PubMed](#)]
218. Gennari, F.C. Mechanochemical synthesis of erbium borohydride: Polymorphism, thermal decomposition and hydrogen storage. *J. Alloys Compd.* **2013**, *581*, 192–195. [[CrossRef](#)]
219. Andrade-Gamboa, J.; Puzkiel, J.A.; Fernández-Albanesi, L.; Gennari, F.C. A novel polymorph of gadolinium tetrahydroborate produced by mechanical milling. *Int. J. Hydrogen Energy* **2010**, *35*, 10324–10328. [[CrossRef](#)]
220. Ley, M.B.; Boulineau, S.; Janot, R.; Filinchuk, Y.; Jensen, T.R. New Li Ion Conductors and Solid State Hydrogen Storage Materials: $\text{LiM}(\text{BH}_4)_3$ Cl, M = La, Gd. *J. Phys. Chem. C* **2012**, *116*, 21267–21276. [[CrossRef](#)]
221. Burkmann, K.; Habermann, F.; Schumann, E.; Kraus, J.; Störr, B.; Schmidt, H.; Brendler, E.; Seidel, J.; Bohmhammel, K.; Kortus, J.; et al. Structural and thermodynamic investigations of $\text{Zr}(\text{BH}_4)_4$ and $\text{Hf}(\text{BH}_4)_4$ between 280 K and their decomposition temperatures. *New J. Chem.* **2024**, *48*, 2743–2754. [[CrossRef](#)]
222. James, B.D.; Nanda, R.K.; Wallbridge, M.G.H. Spectroscopic studies of borohydride derivatives of zirconium and hafnium. *J. Chem. Soc. A* **1966**, *1*, 182–184. [[CrossRef](#)]
223. Green, J.C.; de Simone, M.; Coreno, M.; Jones, A.; Pritchard, H.M.I.; McGrady, G.S. Electronic structure of $\text{M}(\text{BH}_4)_4$, M = Zr, Hf, and U, by variable photon-energy photoelectron spectroscopy and density functional calculations. *Inorg. Chem.* **2005**, *44*, 7781–7793. [[CrossRef](#)] [[PubMed](#)]
224. Marks, T.J.; Shimp, L.A. Structure and Dynamics in Metal Tetrahydroborates. I. Nuclear Magnetic Resonance Studies of Zirconium and Hafnium Tetrahydroborates. *J. Am. Chem. Soc.* **1972**, *94*, 1542–1550. [[CrossRef](#)]
225. Haaland, A.; Shorokhov, D.J.; Tutukin, A.V.; Volden, H.V.; Swang, O.; McGrady, G.S.; Kaltsoyannis, N.; Downs, A.J.; Tang, C.Y.; Turner, J.F. Molecular Structures of Two Metal Tetrakis(tetrahydroborates), $\text{Zr}(\text{BH}_4)_4$ and $\text{U}(\text{BH}_4)_4$: Equilibrium Conformations and Barriers to Internal Rotation of the Triply Bridging BH_4 Groups. *Inorg. Chem.* **2002**, *41*, 6646–6655. [[CrossRef](#)]
226. Bernstein, E.R.; Keiderling, T.A. Optical and magnetic resonance spectra of inorganic molecular crystals-uranium borohydride $[\text{U}(\text{BH}_4)_4]$ in hafnium borohydride $[\text{Hf}(\text{BH}_4)_4]$. *J. Chem. Phys.* **1973**, *59*, 2105–2122. [[CrossRef](#)]
227. Wayda, L.; Schneemeyer, L.F.; Opila, R.L. Low-temperature deposition of zirconium and hafnium boride films by thermal decomposition of the metal borohydrides ($\text{M}[\text{BH}_4)_4$). *Appl. Phys. Lett.* **1988**, *53*, 361–363. [[CrossRef](#)]
228. Broach, R.W.; Chuang, I.S.; Marks, T.J.; Williams, J.M. Metrical Characterization of Tridentate Tetrahydroborate Ligation to a Transition-Metal Ion. Structure and Bonding in $\text{Hf}(\text{BH}_4)_4$ by Single-Crystal Neutron Diffraction. *Inorg. Chem.* **1983**, *22*, 1081–1084. [[CrossRef](#)]
229. Hoekstra, H.R.; Katz, J.J. The Preparation and Properties of the Group IV-B Metal Borohydrides. *J. Am. Chem. Soc.* **1949**, *71*, 2488–2492. [[CrossRef](#)]
230. Wegner, W.; Jaroń, T.; Grochala, W. Polymorphism and hydrogen discharge from holmium borohydride, $\text{Ho}(\text{BH}_4)_3$, and $\text{KHo}(\text{BH}_4)_4$. *Int. J. Hydrogen Energy* **2014**, *39*, 20024–20030. [[CrossRef](#)]
231. Payandeh GharibDoust, S.; Heere, M.; Sørby, M.H.; Ley, M.B.; Ravnsbæk, D.B.; Hauback, B.C.; Černý, R.; Jensen, T.R. Synthesis, structure and properties of new bimetallic sodium and potassium lanthanum borohydrides. *Dalton Trans.* **2016**, *45*, 19002–19011. [[CrossRef](#)] [[PubMed](#)]
232. Payandeh GharibDoust, S.; Brighi, M.; Sadikin, Y.; Ravnsbæk, D.B.; Černý, R.; Skibsted, J.; Jensen, T.R. Synthesis, Structure, and Li-Ion Conductivity of $\text{LiLa}(\text{BH}_4)_3\text{X}$, X = Cl, Br, I. *J. Phys. Chem. C* **2017**, *121*, 19010–19021. [[CrossRef](#)]
233. Liu, R.; Reed, D.; Book, D. Decomposition behaviour of $\text{Mn}(\text{BH}_4)_2$ formed by ball-milling LiBH_4 and MnCl_2 . *J. Alloys Compd.* **2012**, *515*, 32–38. [[CrossRef](#)]
234. Tumanov, N.A.; Roedern, E.; Łodziana, Z.; Nielsen, D.B.; Jensen, T.R.; Talyzin, A.V.; Černý, R.; Chernyshov, D.; Dmitriev, V.; Palasyuk, T.; et al. High-Pressure Study of $\text{Mn}(\text{BH}_4)_2$ Reveals a Stable Polymorph with High Hydrogen Density. *Chem. Mater.* **2016**, *28*, 274–283. [[CrossRef](#)]
235. Roedern, E.; Jensen, T.R. Thermal Decomposition of $\text{Mn}(\text{BH}_4)_2\text{-M}(\text{BH}_4)_x$ and $\text{Mn}(\text{BH}_4)_2\text{-MH}_x$ Composites with M = Li, Na, Mg, and Ca. *J. Phys. Chem. C* **2014**, *118*, 23567–23574. [[CrossRef](#)]

236. Varin, R.A.; Bidabadi, A.S. The effect of milling energy input during mechano-chemical activation synthesis (MCAS) of the nanocrystalline manganese borohydride ($\text{Mn}(\text{BH}_4)_2$) on its thermal dehydrogenation properties. *Int. J. Hydrogen Energy* **2014**, *39*, 11620–11632. [[CrossRef](#)]
237. Varin, R.A.; Mattar, D.K.; Bidabadi, A.S.; Polanski, M. Synthesis of amorphous manganese borohydride in the (NaBH_4 – MnCl_2) system, its hydrogen generation properties and crystalline transformation during solvent extraction. *J. Energy Chem.* **2017**, *26*, 24–34. [[CrossRef](#)]
238. Varin, R.A.; Bidabadi, A.S.; Polanski, M.; Biglari, M.; Stobinski, L. The effects of filamentary Ni, graphene and lithium amide (LiNH_2) additives on the dehydrogenation behavior of mechano-chemically synthesized crystalline manganese borohydride ($\text{Mn}(\text{BH}_4)_2$) and its solvent filtration/extraction. *Mater. Res. Bull.* **2018**, *100*, 394–406. [[CrossRef](#)]
239. Payandeh GharibDoust, S.; Heere, M.; Nervi, C.; Sørby, M.H.; Hauback, B.C.; Jensen, T.R. Synthesis, structure, and polymorphic transitions of praseodymium(III) and neodymium(III) borohydride, $\text{Pr}(\text{BH}_4)_3$ and $\text{Nd}(\text{BH}_4)_3$. *Dalton Trans.* **2018**, *47*, 8307–8319. [[CrossRef](#)] [[PubMed](#)]
240. Banks, R.H.; Edelstein, N.M.; Spencer, B.; Templeton, D.H.; Zalkin, A. Volatility and Molecular Structure of Neptunium(IV) Borohydride. *J. Am. Chem. Soc.* **1980**, *102*, 620–623. [[CrossRef](#)]
241. Banks, R.H.; Edelstein, N.M.; Rietz, R.R.; Templeton, D.H.; Zalkin, A. Preparation and Properties of the Actinide Borohydrides: $\text{Pa}(\text{BH}_4)_4$, $\text{Np}(\text{BH}_4)_4$, and $\text{Pu}(\text{BH}_4)_4$. *J. Am. Chem. Soc.* **1978**, *100*, 1957–1958. [[CrossRef](#)]
242. Banks, R.H.; Edelstein, N.M. *ACS Symposium Series*; Edelstein, N.M., Ed.; American Chemical Society: Washington, DC, USA, 1980; Volume 131, pp. 331–348.
243. Banks, R.H.; Edelstein, N. Vibrational spectra and normal coordinate analysis of neptunium (IV) borohydride and neptunium (IV) borodeuteride. *J. Chem. Phys.* **1980**, *73*, 3589–3599. [[CrossRef](#)]
244. Nakamori, Y.; Orimo, S. *Woodhead Publishing Series in Electronic and Optical Materials*; Walker, H.G., Ed.; Elsevier Reference Monographs: Cambridge, UK, 2008; pp. 420–449.
245. Volkov, V.V.; Myakishev, K.G.; Grankika, Z.A. Infrared Spectra and Nature of the Molecules of Metal Tetrahydroborates of the Type $\text{M}(\text{BH}_4)_4$. *Russ. J. Inorg. Chem.* **1970**, *15*, 1490–1491.
246. Fang, Z.Z.; Ma, L.P.; Kang, X.D.; Wang, P.J.; Wang, P.; Cheng, H.M. In situ formation and rapid decomposition of $\text{Ti}(\text{BH}_4)_3$ by mechanical milling LiBH_4 with TiF_3 . *Appl. Phys. Lett.* **2009**, *94*, 44104. [[CrossRef](#)]
247. Callini, E.; Borgschulte, A.; Hugelshofer, C.L.; Ramirez-Cuesta, A.J.; Züttel, A. The Role of Ti in Alanates and Borohydrides: Catalysis and Metathesis. *J. Phys. Chem. C* **2014**, *118*, 77–84. [[CrossRef](#)]
248. Volkov, V.V.; Myakishev, K.G. Mechanochemical Reaction of Synthesis of Titanium(III) Tetrahydroborate. *Sib. Khim. Zh.* **1992**, *5*, 105–108.
249. Volkov, V.V.; Myakishev, K.G. Synthesis of Titanium(III) Tetrahydroborate with Titanium Trichloride and Lithium Borohydride. *Izv. Akad. Nauk SSSR Ser. Khim.* **1987**, *6*, 1429.
250. Schlesinger, H.I.; Brown, H.C. Uranium(IV) Borohydride. *J. Am. Chem. Soc.* **1953**, *75*, 219–221. [[CrossRef](#)]
251. Katz, J.J.; Rabinowitch, E. *The Chemistry of Uranium. The Element, Its Binary and Related Compounds*; Dover Publications: New York, NY, USA, 1951.
252. Volkov, V.V.; Grankika, Z.A.; Myakishev, K.G. The Nature of Uranium(IV) Borohydride. *Radiochemistry* **1971**, *13*, 416–419.
253. Ghiasee, N.; Clay, P.G.; Walton, G.N. Thermal Decomposition of $\text{U}(\text{BH}_4)_4$. *J. Inorg. Nucl. Chem.* **1981**, *43*, 2909–2913. [[CrossRef](#)]
254. Ravnsbaek, D.B.; Filinchuk, Y.; Cerný, R.; Ley, M.B.; Haase, D.; Jakobsen, H.J.; Skibsted, J.; Jensen, T.R. Thermal polymorphism and decomposition of $\text{Y}(\text{BH}_4)_3$. *Inorg. Chem.* **2010**, *49*, 3801–3809. [[CrossRef](#)] [[PubMed](#)]
255. Yan, Y.; Li, H.-W.; Sato, T.; Umeda, N.; Miwa, K.; Towata, S.; Orimo, S.-I. Dehydrogenating and rehydrogenating properties of yttrium borohydride $\text{Y}(\text{BH}_4)_3$ prepared by liquid-phase synthesis. *Int. J. Hydrogen Energy* **2009**, *34*, 5732–5736. [[CrossRef](#)]
256. Jaroń, T.; Koźmiński, W.; Grochala, W. Phase transition induced improvement in H_2 desorption kinetics: The case of the high-temperature form of $\text{Y}(\text{BH}_4)_3$. *Phys. Chem. Chem. Phys.* **2011**, *13*, 8847–8851. [[CrossRef](#)]
257. Gennari, F.C. Improved hydrogen storage reversibility of LiBH_4 destabilized by $\text{Y}(\text{BH}_4)_3$ and YH_3 . *Int. J. Hydrogen Energy* **2012**, *37*, 18895–18903. [[CrossRef](#)]
258. Jaroń, T.; Grochala, W. $\text{Y}(\text{BH}_4)_3$ --an old-new ternary hydrogen store aka learning from a multitude of failures. *Dalton Trans.* **2010**, *39*, 160–166. [[CrossRef](#)]
259. Frommen, C.; Aliouane, N.; Deledda, S.; Fonnelløp, J.E.; Grove, H.; Lieutenant, K.; Llamas-Jansa, I.; Sartori, S.; Sørby, M.H.; Hauback, B.C. Crystal structure, polymorphism, and thermal properties of yttrium borohydride $\text{Y}(\text{BH}_4)_3$. *J. Alloys Compd.* **2010**, *496*, 710–716. [[CrossRef](#)]
260. Jaroń, T.; Grochala, W. $\text{Y}(\text{BD}_4)_3$, an efficient store of deuterium, and impact of isotope effects on its thermal decomposition. *J. Nucl. Mater.* **2012**, *420*, 307–313. [[CrossRef](#)]
261. Olsen, J.E.; Frommen, C.; Sørby, M.H.; Hauback, B.C. Crystal structures and properties of solvent-free $\text{LiYb}(\text{BH}_4)_{4-x}\text{Cl}_x$, $\text{Yb}(\text{BH}_4)_3$ and $\text{Yb}(\text{BH}_4)_{2-x}\text{Cl}_x$. *RSC Adv.* **2013**, *3*, 10764–10774. [[CrossRef](#)]
262. Nakamori, Y.; Miwa, K.; Ninomiya, A.; Li, H.; Ohba, N.; Towata, S.; Züttel, A.; Orimo, S.-I. Correlation between thermodynamical stabilities of metal borohydrides and cation electronegativities: First-principles calculations and experiments. *Phys. Rev. B* **2006**, *74*, 045126. [[CrossRef](#)]
263. Gennari, F.C.; Fernández Albanesi, L.; Rios, I.J. Synthesis and thermal stability of $\text{Zr}(\text{BH}_4)_4$ and $\text{Zr}(\text{BD}_4)_4$ produced by mechanochemical processing. *Inorg. Chim. Acta* **2009**, *362*, 3731–3737. [[CrossRef](#)]

264. Davies, N.; Saunders, D.; Wallbridge, M.G.H. Exchange Reactions of Zirconium Tetrakis(tetrahydroborate). *J. Chem. Soc. A* **1970**, *15*, 2915–2917. [[CrossRef](#)]
265. Marks, T.J.; Kennelly, W.J.; Kolb, J.R.; Shimp, L.A. Structure and Dynamics in Metal Tetrahydroborates. II. Vibrational Spectra and Structures of Some Transition metal and Actinide Tetrahydroborates. *Inorg. Chem.* **1972**, *11*, 2540–2546. [[CrossRef](#)]
266. Sung, J.; Goedde, D.M.; Girolami, G.S.; Abelson, J.R. Remote-plasma chemical vapor deposition of conformal ZrB₂ films at low temperature: A promising diffusion barrier for ultralarge scale integrated electronics. *J. Appl. Phys.* **2002**, *91*, 3904–3911. [[CrossRef](#)]
267. Rude, L.H.; Corno, M.; Ugliengo, P.; Baricco, M.; Lee, Y.-S.; Cho, Y.W.; Besenbacher, F.; Overgaard, J.; Jensen, T.R. Synthesis and Structural Investigation of Zr(BH₄)₄. *J. Phys. Chem. C* **2012**, *116*, 20239–20245. [[CrossRef](#)]
268. James, B.D.; Smith, B.E. Convenient, High-Yield Syntheses of Bis(tetrahydroborato)bis(cyclopentadienyl)zirconium(IV) and Tetrakis(tetrahydroborato)zirconium(IV). *Synth. React. Inorg. Met.-Org. Chem.* **1974**, *4*, 461–465. [[CrossRef](#)]
269. Sayer, B.G.; Thompson, J.I.A.; Hao, N.; Birchall, T.; Eaton, D.R.; McGlinchey, M.J. Zirconium-91 NMR Spectrum of Zr(BH₄)₄: The Zr-H Coupling Constant as a Probe for a Fast Intramolecular Process. *Inorg. Chem.* **1981**, *20*, 3748–3750. [[CrossRef](#)]
270. Smith, B.E.; Shurvell, H.F.; James, B.D. Molecular Vibrations of Zirconium(IV) Tetrahydroborate, a Compound containing Triple Hydrogen Bridges. *Phys. Rev. B* **1978**, *7*, 710–722. [[CrossRef](#)]
271. Igoshkin, M.; Golovnev, I.F.; Krisyuk, V.V.; Igumenov, I.K. Structure of Zirconium Tetrahydroborate Zr(BH₄)₄: A Molecular Dynamics Study. *J. Struct. Chem.* **2016**, *57*, 1068–1073. [[CrossRef](#)]
272. Yan, Y.; Remhof, A.; Rentsch, D.; Lee, Y.-S.; Whan Cho, Y.; Züttel, A. Is Y₂(B₁₂H₁₂)₃ the main intermediate in the decomposition process of Y(BH₄)₃? *Chem. Commun.* **2013**, *49*, 5234–5236. [[CrossRef](#)]
273. Guda, A.; Pankin, I.A.; Bugaev, A.L.; Lomachenko, K.A.; Guda, S.A.; Dmitriev, V.P.; Soldatov, A.V. X-Ray Absorption Spectroscopy Determination of the Products of Manganese Borohydride Decomposition upon Heating. *Bull. Russ. Acad. Sci. Phys.* **2015**, *79*, 139–143. [[CrossRef](#)]
274. Pankin, A.; Guda, A.A.; Tumanov, N.A.; Filinchuk, Y.; Lomachenko, K.A.; Bugaev, A.L.; Guda, S.A.; Shapovalov, V.V.; Lamberti, C.; Soldatov, A.V. Experimental and theoretical study of hydrogen desorption process from Mn(BH₄)₂. *J. Alloys Compd.* **2018**, *735*, 277–284. [[CrossRef](#)]
275. Łodziana, Z. Multivalent metal tetrahydroborides of Al, Sc, Y, Ti, and Zr. *Phys. Rev. B* **2010**, *81*, 1–12. [[CrossRef](#)]
276. Paskevicius, M.; Jepsen, L.H.; Schouwink, P.; Černý, R.; Ravnsbæk, D.B.; Filinchuk, Y.; Dornheim, M.; Besenbacher, F.; Jensen, T.R. Metal borohydrides and derivatives—Synthesis, structure and properties. *Chem. Soc. Rev.* **2017**, *46*, 1565–1634. [[CrossRef](#)] [[PubMed](#)]
277. Varin, R.A.; Zbroniec, L.; Polanski, M.; Filinchuk, Y.; Černý, R. Mechano-chemical synthesis of manganese borohydride (Mn(BH₄)₂) and inverse cubic spinel (Li₂MnCl₄) in the (nLiBH₄ + MnCl₂) (n = 1, 2, 3, 5, 9 and 23) mixtures and their dehydrogenation behavior. *Int. J. Hydrogen Energy* **2012**, *37*, 16056–16069. [[CrossRef](#)]
278. Harrison, D.; Thonhauser, T. Suppressing diborane production during the hydrogen release of metal borohydrides: The example of alloyed Al(BH₄)₃. *Int. J. Hydrogen Energy* **2016**, *41*, 3571–3578. [[CrossRef](#)]
279. Borgschulte, A.; Callini, E.; Probst, B.; Jain, A.; Kato, S.; Friedrichs, O.; Remhof, A.; Biemann, M.; Ramirez-Cuesta, A.J.; Züttel, A. Impurity Gas Analysis of the Decomposition of Complex Hydrides. *J. Phys. Chem. C* **2011**, *115*, 17220–17226. [[CrossRef](#)]
280. Li, H.-W.; Orimo, S.; Nakamori, Y.; Miwa, K.; Ohba, N.; Towata, S.; Züttel, A. Materials designing of metal borohydrides: Viewpoints from thermodynamical stabilities. *J. Alloys Compd.* **2007**, *446–447*, 315–318. [[CrossRef](#)]
281. Rumble, J.R.; Bruno, T.J. (Eds.) *CRC Handbook of Chemistry and Physics*; A Ready-Reference Book of Chemical and Physical Data; CRC Press: Boca Raton, FL, USA, 2020.
282. Riedel, E.; Janiak, C. *Anorganische Chemie*, 9th ed.; De Gruyter: Berlin, Germany; Boston, MA, USA, 2015.
283. Callini, E.; Borgschulte, A.; Ramirez-Cuesta, A.J.; Züttel, A. Diborane release and structure distortion in borohydrides. *Dalton Trans.* **2013**, *42*, 719–725. [[CrossRef](#)] [[PubMed](#)]
284. Du, J.; Smith, S.C.; Lu, G.Q. Role of charge in destabilizing AlH₄ and BH₄ complex anions for hydrogen storage applications: Ab initio density functional calculations. *Phys. Rev. B* **2006**, *74*, 193405. [[CrossRef](#)]
285. McMillan, P.F. New materials from high-pressure experiments. *Nat. Mater.* **2002**, *1*, 19–25. [[CrossRef](#)] [[PubMed](#)]
286. Takeshita, T.; Gschneidner, K.A.; Lakner, J.F. High Pressure Hydrogen Absorption Study on YNi₅, LaPt₅ and ThNi₅. *J. Less-Common Met.* **1981**, *78*, 43–47. [[CrossRef](#)]
287. Vedel, I.; Redon, A.-M.; Mignot, J.-M.; Leger, J.-M. Absence of discontinuity in the pressure-volume dependence of CeAl₂ and CeIn₃. *J. Phys. F Met. Phys.* **1987**, *17*, 849–856. [[CrossRef](#)]
288. Cannon, J.F.; Hall, H. Effect of High Pressure on the Crystal Structures of Lanthanide Trialuminides. *J. Less-Common Met.* **1975**, *40*, 313–328. [[CrossRef](#)]
289. Sekar, M.; Chandra Shekar, N.; Sahu, P.; Sanjay Kumar, N.; Rajan, K. High pressure X-ray diffraction study of LaAl₂ and LaAl₃. *Phys. B* **2002**, *324*, 240–244. [[CrossRef](#)]
290. Griessen, R.; Driessen, A. Heat of formation and band structure of binary and ternary metal hydrides. *Phys. Rev. B* **1984**, *30*, 4372–4381. [[CrossRef](#)]
291. Griessen, R.; Driessen, A.; de Groot, D.G. Search for New Metal-Hydrogen Systems for Energy Storage. *J. Less-Common Met.* **1984**, *103*, 235–244. [[CrossRef](#)]

292. Vajeeston, P.; Ravindran, P.; Kjekshus, A.; Fjellvåg, H. High hydrogen content complex hydrides: A density-functional study. *Appl. Phys. Lett.* **2006**, *89*, 71906. [[CrossRef](#)]
293. Alapati, S.V.; Johnson, J.K.; Sholl, D.S. Identification of Destabilized Metal Hydrides for Hydrogen Storage Using First Principles Calculations. *J. Phys. Chem. B* **2006**, *110*, 8769–8776. [[CrossRef](#)] [[PubMed](#)]
294. Lu, J.; Fang, Z.Z.; Choi, Y.J.; Sohn, H.Y. The Potential of Binary Lithium Magnesium Nitride—LiMgN for Hydrogen Storage Application. *MRS Online Proc. Libr.* **2007**, *1042*, 1042-S05. [[CrossRef](#)]
295. Alapati, S.V.; Karl Johnson, J.; Sholl, D.S. Using first principles calculations to identify new destabilized metal hydride reactions for reversible hydrogen storage. *Phys. Chem. Chem. Phys.* **2007**, *9*, 1438–1452. [[CrossRef](#)] [[PubMed](#)]
296. Akbarzadeh, R.; Ozoliņš, V.; Wolverton, C. First-Principles Determination of Multicomponent Hydride Phase Diagrams: Application to the Li-Mg-N-H System. *Adv. Mater.* **2007**, *19*, 3233–3239. [[CrossRef](#)]
297. Wolverton, C.; Siegel, D.J.; Akbarzadeh, A.R.; Ozoliņš, V. Discovery of novel hydrogen storage materials: An atomic scale computational approach. *J. Phys. Condens. Matter* **2008**, *20*, 64228. [[CrossRef](#)]

Disclaimer/Publisher’s Note: The statements, opinions and data contained in all publications are solely those of the individual author(s) and contributor(s) and not of MDPI and/or the editor(s). MDPI and/or the editor(s) disclaim responsibility for any injury to people or property resulting from any ideas, methods, instructions or products referred to in the content.